Dissertation
submitted to the
Combined Faculties for the Natural Sciences and for Mathematics
of the Ruperto-Carola University of Heidelberg, Germany
for the degree of
Doctor of Natural Sciences

presented by
Diplom-Physicist Michael Peter Geyer
born in Schweinfurt
Oral examination: February 13, 2002

Numerical Simulations on the Formation of Massive Star Clusters

Referees: **Priv.-Doz. Dr. Andreas Burkert**
Prof. Dr. Wolfgang J. Duschl

Numerische Simulationen zur Entstehung von massereichen Sternhaufen
Die Entstehung von massereichen gebundenen Sternhaufen in Molekülwolken ist ein Wettrennen zwischen effizienter Sternentstehung und energetischen Rückkopplungsprozessen massereicher Sterne. Diese unterbinden den Sternentstehungsprozeß und treiben das Restgas aus dem System.

Der Einfluß des Gasausstoßes auf die dynamische Entwicklung von Sternentstehungsregionen wurde untersucht. Bei kollisionsfreien numerischen N–Körperrechnungen wurde der Gasausstoß aus einem gebundenen System aus Sternen und umgebenden Gas durch ein externes Potential beschrieben. Die Sternhaufen bleiben nur dann gebunden, wenn entweder die Sternentstehungseffizienz wesentlich höher ist als die in der Galaxis typische, wenn die Zeitskala des Gasausstoßes ein mehrfaches der dynamischen Zeitskala beträgt oder wenn sich das System anfangs nicht im virialen Gleichgewicht befand.

Deswegen wurde außerdem die Entstehung von Sternhaufen aus anfänglich kalten, turbulenten Molekülwolken untersucht. Zur numerischen Simulation des Gases wurde „Smoothed Particle Hydrodynamics“ mit einer idealisierenden Beschreibung der Sternentstehung verwendet. Die Sterne selbst werden wieder mittels kollisionsfreier N–Körperrechnung beschrieben, die Rückkopplung wird durch thermisches Heizen des umgebenden Gases simuliert. Die Sternentstehungseffizienz der kollabierenden und fragmentierenden Molekülwolke und damit die Gebundenheit des resultierenden Systems wird wesentlich beeinflußt von der Zeitverzögerung zwischen der Bildung der Sterne und dem Einsetzen der Rückkopplung, sowie von dem gewählten globalen Dichtekriterium, das bestimmt zu welchem Zeitpunkt sich die Sterne während des Kollapses der Wolke bilden.

Numerical Simulations on the Formation of Massive Star Clusters
The formation of massive bound stellar clusters in molecular clouds is a race between efficient star formation and energetic feedback processes by high mass stars, which cancel star formation and expel the residual gas.

The influence of gas expulsion on the dynamical evolution of star forming regions, initially consisting of a bound system of stars and gas, is investigated. Collisionless numerical N–body calculations were performed, describing the gas expulsion by a time variable external potential. Bound clusters will only result, if the star formation efficiency is considerably higher than the typical observed efficiencies in the Galaxy, if the gas expulsion timescale is several times longer than the dynamical timescale or if the system initially is not in virial equilibrium.

Therefore the formation of clusters from initially cold turbulent molecular clouds is investigated, using smoothed particle hydrodynamics with an idealized star formation description. Stars are treated as collisionless N–bodies and feedback is implemented by thermally heating the surrounding medium. In the collapsing and fragmenting molecular cloud the star formation efficiency and thus the boundness of the resulting system strongly depends on the time delay between the formation of stars and the time when feedback from the stars begins and on a chosen global density criterion, which determines when stars form during the collapse of the cloud.

There is a theory which states that if ever anyone discovers exactly what the Universe is for and why it is here, it will instantly disappear and be replaced by something even more bizarre and inexplicable.

There is another which states that this has already happened.

Douglas Adams, ∗11th March, 1952 †11th May, 2001

Contents

Chapter 1

Introduction

Our understanding of the formation of massive bound stellar clusters is still unsatisfactory. Although it is widely accepted today that star formation takes place in the cores of collapsing and fragmenting cold turbulent molecular clouds, unsolved questions remain regarding the formation of *bound* stellar clusters. Besides hot topics like the initial mass function, spatial structures, star formation efficiency and dynamical properties of the newly-formed stars, the pure existence of bound stellar clusters is a puzzle that is not solved until now.

Inspired by observations, star clusters are divided into two main groups: open clusters and globular clusters. In our Galaxy, the loosely bound open clusters with a mass range from hundreds to thousands of solar masses are preferentially found inside the Galactic plane. Open clusters in general are very young, with maximum estimated lifetimes of roughly a few hundred million years. The globular clusters, which are found in the Galactic halo, can contain up to several million solar masses. They are strongly centrally concentrated with ages of 10 billion years and beyond. Whereas formation of open clusters is common in our Galaxy even today, no recently formed globular clusters are known. Up to now only one candidate for a young globular cluster has been found by Knödlseder (2000). On the other hand, observations show that a large number of massive stellar clusters form today in other galaxies e.g. in the starburst regions of merging galaxies (Whitmore & Schweizer 1995, Zepf et al. 1999) or the Large Magellanic Cloud. It is still unclear where the differences in these formation processes come from — why do such massive clusters form in other galaxies, but not in our Milky Way ?

Peeking into the formation process of a cluster, we start with a fragmenting molecular cloud. Stars form in the dense cores. In recent numerical simulations by Klessen & Burkert (2000) and Klessen & Burkert (2001) the fragmentation of molecular clouds could be followed down to the scale of the protostars. In their simulations stars accrete all the gas that is left in the system. However, as soon as stars have formed, their energetic feedback, like stellar winds, ionizing radiation and, in the later stages of the evolution, even supernovae will expel the residual gas that is left over from star formation, thus limiting the star formation efficiency. The star formation efficiency, which is the ratio of the mass of the formed stars to the initial gas mass, is a crucial parameter determining the future fate of the stellar system: If it is too low, expelling the gas will have a destructive effect on the system and it will develop into an unbound association of stars. Only if the efficiency, at least in the local vicinity of the stars, is high enough, massive bound clusters like the globulars will be able to form. Thus, a full understanding of star cluster formation can only be obtained by examining the complex interplay between the turbulent dynamics of the initial molecular gas clouds, star formation and stellar feedback.

The aim of this thesis is to cast light on the circumstances that allow the formation of bound clusters. We examine the influences of gas expulsion on the dynamical evolution of young stellar clusters and simulate their formation starting with molecular clouds and incorporating stellar feedback. This allows us to investigate how feedback alters the properties of the young stars, the efficiency of star formation, the conditions required to form a bound stellar cluster and how feedback destroys molecular clouds.

Although the general statements of this thesis will be adaptable to star clusters of various sizes and masses, it will concentrate on the most puzzling representatives — the globular clusters.

The structure of this thesis is as follows:

Chapter 2 first gives a short overview of the main properties of globular clusters in our and other galaxies. Different globular cluster formation scenarios and their implications will be reviewed. Also the properties of molecular clouds, which are needed for a basic understanding of cluster formation, will be presented. The chapter ends with an overview of recent observations regarding "young globular clusters". These are objects, to some extent being only a few million years old, which presumable are the progenitors of globulars and are therefore of interest for understanding the formation process.

Chapter 3 gives a general introduction into hydrodynamics, which in this work is needed to describe the evolution of the molecular cloud gas. Starting with the Boltzmann equation, the basic equations of hydrodynamics as well as of self-gravitating many particle systems are derived schematically. Chapter 3 also presents the numerical methods used in this thesis: The stellar part of the systems will be described by a collisionless N–body method. The gas dynamics is followed using the more and more popular smoothed particle hydrodynamics (SPH), where the gas is represented by spatially smeared out "gas particles". SPH is intrinsically Lagrangian and is able to follow high density contrasts.

Chapter 4 first concentrates on how an idealized description of star formation can be implemented into the numerical scheme. After energetic considerations regarding the energy feedback from massive OB stars into the surrounding interstellar medium and their ability to disrupt the parental cloud, analytical derivations are presented, which give a threshold for the star formation efficiency that is needed to obtain a bound cluster after the expulsion of the residual gas. The chapter ends with a description of the implementation of feedback, in which the thermal energy of the SPH gas particles surrounding the stars is increased.

Chapter 5 shows the effects of gas expulsion on star forming regions, starting with a system that already has formed stars. It emphasizes the importance of the star formation efficiency and the gas expulsion timescale for the question whether the resulting stellar system is bound or not. The dynamical evolution is investigated with special emphasize on the spatial enlargements and the density distributions.

Chapter 6 then presents numerical simulations looking at the formation process itself. Starting with a cold turbulent molecular cloud, the collapse and fragmentation are followed. Star formation and energy feedback as given in Chapter 4 are included and their effects are studied. The choice of parameters that leads to a dynamical stable or bound stellar system is investigated.

The thesis ends with Chapter 7, which provides a summary of the obtained conclusions as well as a brief outlook on how to improve the numerical methods that were used.

Chapter 2

Globular Clusters and Massive Cluster Formation

If not all, at least a great fraction of stars is born in clusters. Based on observations in our Galaxy, star clusters are divided into the loosely bound open clusters, found mainly in the Galactic plane, and the compact globular clusters, which are part of the Galactic halo. This thesis concentrates on the formation of massive star clusters. Defining a massive star cluster by a mass threshold of $10^5\,M_\odot$, in our Galaxy only the old globular clusters fall into this regime (Mermilliod 2000). Therefore, this chapter concentrates on the Globulars in our Galaxy, but also on young massive clusters observed in external galaxies.

It is impractical to give a general definition of a globular cluster. Usually, star clusters with ages greater than 10 billion years found in the bulge or halo regions of galaxies are called "globulars". But, if one wishes to incorporate the so called "young globular clusters", forming at the very moment in external galaxies and therefore having ages as low as several million years, another approach is advisable: Globular clusters are gravitationally bound stellar systems that contain up to several millions of stars which are centrally concentrated and show a spherical symmetric density distribution. However, in our Milky Way globulars with only thousand solar masses are known to exist, drawing near the masses of rich open clusters. All these forms of appearance have to be included in a general definition of globular clusters.

This chapter starts with a short overview of the properties of old globular clusters. Several actual formation models for mass-rich star clusters, their predictions that have to be matched with observations, as well as their problems are discussed. Giant molecular clouds are likely to be the progenitors of bound as well as unbound star clusters. In the second section, we therefore give a brief review regarding the properties of molecular clouds. Young, mass-rich clusters of which presumably at least a certain fraction might be the progenitors of future globulars are the ideal test case for formation models. In the last section, the important aspects of these systems derived from observations are listed.

2.1 Globular Clusters - A Short Overview

Recent overviews and citations to important papers regarding the properties of globular clusters can be found in the extensive review by Meylan & Heggie (1997) or in the text book by Ashman & Zepf (1999). Understanding globular cluster formation also implies the knowledge of the properties of globular cluster systems of our and other galaxies as a whole. A useful review is

given by Harris (1991) and also in the above mentioned text book. Tables for a large fraction of the about 140 observed Galactic globular clusters can be found in Chernoff & Djorgovski (1989). Harris (1996) provides tables of now 142 globular clusters accessible via world wide web (WWW). Djorgovski & Meylan (1994) give a detailed analysis of correlations between the different Milky Way globular cluster quantities. An introduction to the different aspects of the dynamical evolution is given in the text book by Spitzer (1987). The mentioned citations are the basis for the following overview.

Whereas external galaxies may contain considerably more than thousand globulars, in our Milky Way presumably 160 ± 20 globulars exist, of which about 140 are observed (Harris 1991). A useful quantity for comparing globular cluster systems of different galaxies is the specific frequency

$$S_N = N_t \, 10^{0.4(M_v+15)} \,, \tag{2.1.1}$$

where N_t is the total number of clusters and M_v the absolut visual magnitude of the host galaxy. There is a general trend for an increasing specific frequency from spirals or irregular to elliptical and giant elliptical galaxies (e.g. Harris 1991). Explaining these frequencies will be crucial for each formation model.

Milky Way globular clusters show masses in the range from several thousand up to several million solar masses. Looking at the dynamics, up to now no evidence for dark matter, besides neutron stars, white dwarfs or brown dwarfs in globulars has been found.

Regarding the spatial properties, the majority of globular clusters can be well described by a spherical symmetric density distribution drawn from distribution functions first proposed by King (1966). Postponing the mathematical description of those models to Chapter 5, we now only mention the important parameters: First, the models have a finite spatial extension up to the tidal radius r_t. From observations, one gets the core radius r_c, which is the radius where the projected density dropped to half its central value. This core radius roughly equals the King radius which is defined by the King profile (Binney & Tremaine 1987). Observations show that the core radii lie in the large range of 0.03 pc and 30 pc. However, omitting clusters with extreme values, the majority shows core radii between 0.3 pc and 10 pc. Globulars are distributed within the Galactic halo with distances from 0.6 kpc up to 123 kpc from the Galactic center. The cluster system is strongly concentrated towards the Galactic center (Figure 2.1), so the mean distance is about 12 kpc. Figure 2.2 shows that the concentrations of globular clusters, which characterize the King profile and are defined as $\log(r_t/r_c)$, are wide spread. The scaled central potential W_0 is directly connected to the concentration and will also be defined in Chapter 5. Concluding from the large variety of these numbers, one can see that the globular clusters in our Milky Way alone span a large parameter space that has to be explained by formation models.

The ages of globular clusters can be determined principally using the turn-off point of the main sequence in Hertzsprung-Russel diagrams (HRD), see e.g. Ashman & Zepf (1999). For several years, measurements were in contradiction with the age of the universe — at least the universe must be older than the objects within it. Problems in the age estimations are due to errors in the distances and chemical composition as well as uncertainties in stellar evolution models. During the last years, the estimated values of globular cluster ages have decreased and now are in accordance with the age estimations of the universe. E.g. Carretta et al. (2000) give a mean age of $12.9\,\mathrm{Gyr} \pm 2.9\,\mathrm{Gyr}$ for a sample of nine globular clusters. Most Milky Way globulars are equally old, but there is evidence for a subset of globulars being significantly younger than

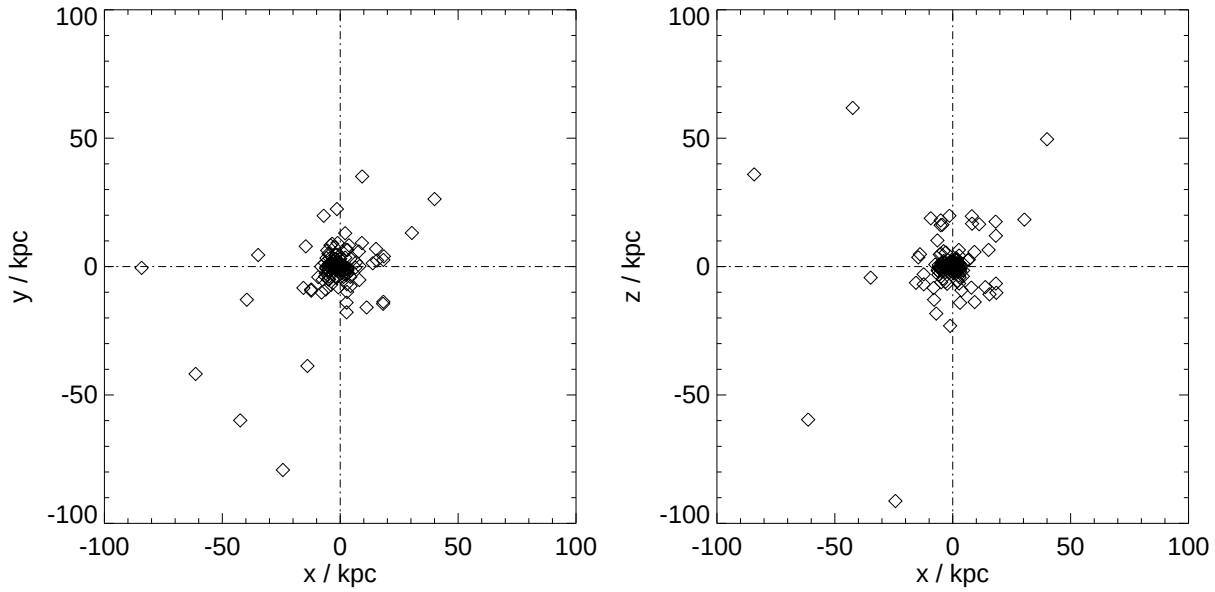

Figure 2.1: *Spatial distributions of Galactic globular clusters projected onto the x–y plane (left) and x–z plane (right); the center of the Milky Way is located at $x = y = z = 0$; the data have been taken from Harris (1996).*

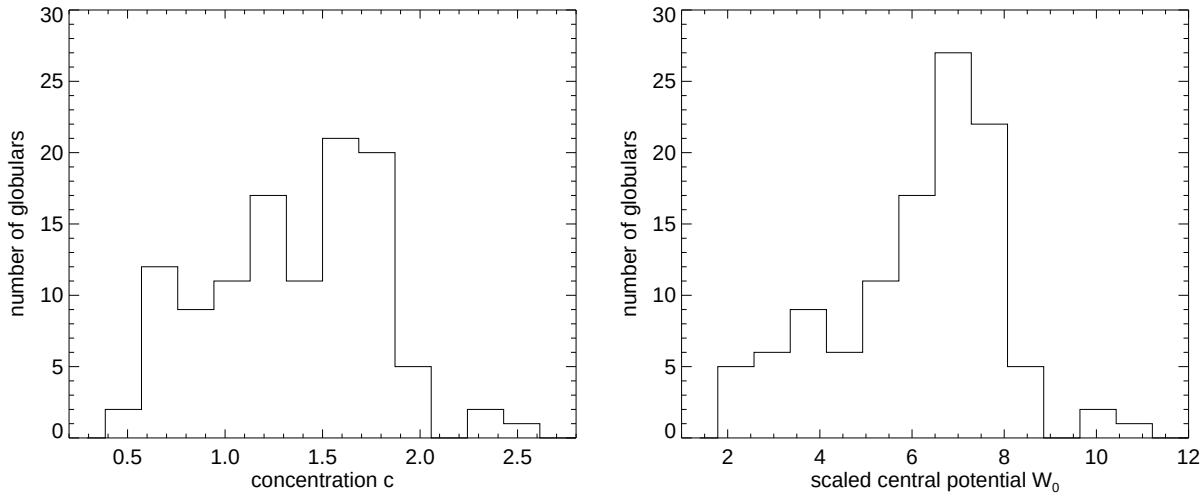

Figure 2.2: ***Left:*** *histogram of the concentration c_0;* ***Right:*** *histogram of the scaled potential W_0; in both figures globular clusters which have presumable undergone core collapse are excluded; the data have been taken from Harris (1996).*

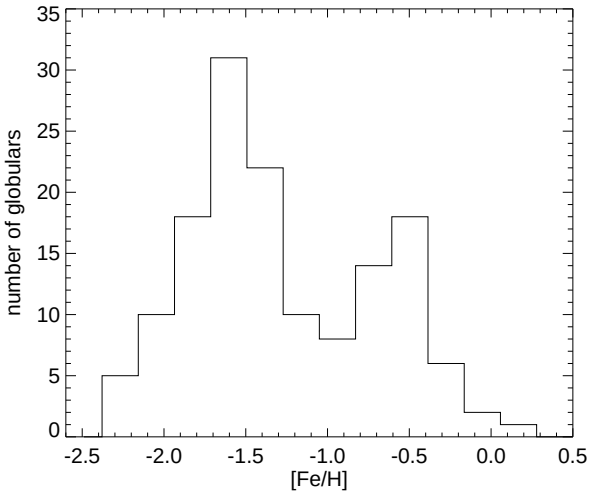

Figure 2.3: *Histogram of the metallicity distribution; the data have been taken from Harris (1996).*

the others, with an age difference of about 3 Gyr.

Among the stars of a globular cluster, the relative metallicity, compared to solar values, $[\mathrm{Fe/H}] = \log(\mathrm{Fe/H}) - \log(\mathrm{Fe/H})_\odot$ varies only little. However, individual clusters show different metallicities. Looking at the histogram of metallicities (Figure 2.3), one can see two distinct peaks at about $[\mathrm{Fe/H}] = -1.6$ and $[\mathrm{Fe/H}] = -0.5$. Zinn (1985) indeed showed by additionally examining spatial and kinematic properties, that the two metal-poor and metal-rich cluster systems are distributed differently within the Milky Way. Such bimodal metallicity distributions have been observed in a large fraction of globular cluster systems around other galaxies (see Ashman & Zepf (1999) and references therein).

Globular as well as open clusters can be disrupted by internal and external processes. Thus, the cluster mass distribution observed today does not necessarily coincide with the initial mass distribution. The most important internal process is evaporation of stars due to two-body encounters. At times one star may gain such high velocities that it can escape from the bound system. For a typical globular cluster, the timescale of this process is of the order of 10 Gyr. However, the smaller the number of particles, the shorter is the timescale. The same behaviour, that low mass clusters are disrupted faster, is caused by external processes like the influence of the tidal field of the galaxy. Indeed, Elmegreen & Efremov (1997) argue that the different mass distribution functions regarding open and globular clusters can be explained by preferentially disrupting low mass clusters. This would evolve an initial power law distribution function, as observed among open clusters, to the gaussian observed among globulars. This picture leads to a universal formation scenario for both open and globular clusters.

2.2 Formation Scenarios

In the literature, formation scenarios for globular clusters are commonly divided into three distinguishable types: *Primary formation models* stage the forming of the first globular clusters in the framework of the building of cosmological structure. Peebles & Dicke (1968) first invented this idea and supposed that globular clusters might have been the first objects formed in the

universe. *Secondary models* assume that globular clusters form at the same time with their host galaxies. A prominent theory in this regime was proposed by Fall & Rees (1985), where cooling instabilities in the environment of the proto-galaxy lead to the formation of proto-globular cluster clouds which successively form star clusters. *Tertiary formation models* set globular cluster formation after the host galaxies have formed, e.g. in interacting or merging galaxies (Ashman & Zepf 1992) or even by accretion of dwarf galaxies.

The primary formation model by Peebles & Dicke (1968) explains naturally the gaussian cluster mass distribution with typical masses of order $10^6 M_\odot$ and radii of 10 pc, which is just the Jeans mass and length at the time of recombination. However, this model leads to contradictions with observations: First, globulars forming before their host galaxy cannot explain the observed correlation between metallicities of the cluster and their host galaxies (Harris 1991). Second, globular clusters show no signs of any dark matter halo, which should be expected if they form as the first cosmological objects.

In the Fall & Rees (1985) picture, the 10^6 K hot gas around the proto-galaxy is thermally unstable and develops a two-phase structure with cooler 10^4 K clouds embedded in the hot medium. If these clouds last long enough at this temperature to grow to typical masses of $10^6\, M_\odot$, they will get gravitational unstable, collapse and form globulars. However, in their original paper Fall & Rees (1985) did not take into account cooling due to H_2 formation. The clouds cannot persist long enough at temperatures of 10^4 K and just cool down further. The case is even worse if cooling by metals is included. Thus, to save the model, one must assume heat sources which keep the clouds from cooling further. Proposed mechanisms are the ultra-violet or X-ray flux due to an earlier generation of stars or active galactic nuclei (for references see Ashman & Zepf 1999).

The most prominent tertiary mechanism is the formation in external interacting or merging galaxies. Ashman & Zepf (1992) list evidences for young globular cluster formation in such environments. The observed excess in the specific frequency around ellipticals can then be explained by forming a new population of clusters during the merging process of two spirals. This scenario also can explain the bimodal metallicity distribution observed in many galaxies: The younger systems will form in a more metal-rich environment compared to the old population. The lack of dark matter mentioned above puts constraints on other tertiary models which assume accretion of dwarf galaxies containing dark matter. Dwarf galaxies, in contrast to globulars, also exhibit a significant range in metallicity (van den Bergh 2000). However, accretion of dwarf galaxies might explain the high specific frequencies around elliptical galaxies.

Although the assumption that all globular clusters formed before their host galaxies is very unlikely, van den Bergh (2001) proposes two distinct formation epochs for globulars: The first one is set after reionization of the universe (Cen 2001) and is therefore primary, the second family of clusters is formed during mergers and is thus tertiary.

Already mentioned in the last section, Elmegreen & Efremov (1997) propose a universal formation mechanism for cluster formation. Therefore they do not need to explain the preferred gaussian mass distribution around $10^6\, M_\odot$ observed for globulars. Globular clusters then just form at the high mass end compared to the less massive open clusters.

2.3 Molecular Clouds as Progenitors of Massive Star Clusters

It is widely accepted that stars form in the cores of cold molecular clouds. A natural extension to larger scales is to conclude that giant molecular clouds or complexes are the birthplaces of stellar clusters. By that their properties fix the initial conditions and will have direct effects on cluster formation. We follow the nomenclature of Blitz (1993): Molecular clouds are called "giant" if their mass is approximately or larger than $10^5\,M_\odot$. The typical diameter is 45 pc, the typical mean H_2 number density is $50\,\mathrm{cm}^{-3}$.

Molecular clouds in general only show very small variations around the mean temperature of 10 K, corresponding to an isothermal sound speed of $a = 0.2\,\mathrm{km/s}$. This almost constant temperature is caused by the well-balanced heat input from cosmic rays and cooling caused by the most abundant molecular species (Goldsmith & Langer 1978). For this reason, in this thesis we use the isothermal equation of state to describe the molecular cloud gas. Only in protostellar cores, where the number density exceeds $10^{10}\mathrm{cm}^{-3}$, the cloud becomes opaque and the isothermal assumption is no longer valid.

Molecular clouds show self-similar structures, sometimes even believed to be fractal, down to the smallest scales that are observable (Stutzki et al. 1998, Datta 2001). These spatial structures are accompanied by structures in the velocity field: The velocity dispersion σ, measured from line-widths, scales with the cloud size as $\sigma \sim L^\alpha$, where α is in the range of 0.20 to 0.6 (Blitz 1993, Goodman et al. 1993, Goodman et al. 1998). These velocities are commonly interpreted as turbulent supersonic random motions with a typical Mach number of $M \approx 10$. The observed line-width relation can be transformed into a power spectrum of the velocities, which is the Fourier transformation into k-space, where k is the wavenumber. It has been shown that a power-law power spectrum $P(k) \sim k^{-n}$ with $n = 3 \ldots 4$ describes well the properties of the clouds (Myers & Gammie 1999, Burkert & Bodenheimer 2000). In Chapter 6, we make use of these properties to get justifiable initial conditions for the cluster forming simulations.

Molecular clouds are gravitationally bound. Without an internal or external driver for the turbulence, the clouds will collapse on the dynamical timescale which is of order of $10^6\,\mathrm{yr}$, even in the presence of stabilizing magnetic fields (Mac Low et al. 1998, Mac Low 1999). However, Blitz & Shu (1980) indicate lifetimes of about $10^7\,\mathrm{yr}$. One way out might be that molecular clouds are only an intermediate stage in the overall evolution of the interstellar matter. Then, they might be short-lived and form stars without any delay (Elmegreen 2000).

However, of interest for this thesis is only the fact that turbulence in molecular clouds exists. The intrinsic density and velocity fields will imprint their properties on the velocities and spatial distribution of the forming stars and therefore may be of great importance regarding the properties of the newly-born cluster.

2.4 Observations of Young Massive Clusters

Up to now, in our Galaxy only one candidate for a young massive or globular cluster has been found by Knödlseder (2000). On the other hand, observations show that a large number of massive stellar clusters form today or have formed recently in other galaxies e.g. in the starburst regions of merging galaxies (Whitmore & Schweizer 1995, Zepf et al. 1999) or the Large Magellanic Cloud (Drissen et al. 2000). An extensive list of galaxies with young globular clusters is given by Schweizer (1999).

The crucial question is whether these observed compact, bright blue objects really will evolve into systems that look like the globular clusters today. Zepf et al. (1999) identified more than 1000 of such objects in the galaxy merger NGC 3256. As many of them show masses and sizes comparable to Galactic globulars, they identify them as young globular clusters. They conclude that due to the high efficiency of cluster formation, the excess of globulars around elliptical galaxies can be explained, if they form by merging of gas-rich spiral galaxies. Fritze-v. Alvensleben (1998) analysed the population of young star clusters in the galaxy merger NGC 4038/4039. Using a spectrophotometric evolutionary synthesis model, she evolves the luminosity function of the young cluster system to what it may look like in 12 Gyr. She finds that the final state is in good agreement with the observed gaussian luminosity function, which reflects the gaussian mass distribution mentioned in Section 2.1.

Schweizer (1999) emphasizes that the young clusters in advanced mergers already have ages which are of order 10 times the dynamical timescale of the systems. If they were not gravitationally bound from the beginning, they now would resemble a loosely bound, expanding association. To proof that these young massive clusters are really the progenitors of today's globulars, one also has to make sure that these system are compact enough to survive in the tidal fields of their host galaxies.

Coming back to the universal formation scenario for open and globular clusters, we recall that one difference between these two populations is the mass distribution, which is tightly connected to the luminosity function. Whitmore et al. (1999) measured the young cluster luminosity function in the merger NGC 4038/4039. They showed that it can be described by a power-law like the open clusters in our Milky Way. Destruction of low mass clusters during the evolution then could evolve this power-law into the gaussian distribution observed for the globulars.

Observations of young clusters in the Large Magellanic Cloud even allow the measurement of radial luminosity distributions (Elson 1991), which is not possible for the distant galaxy mergers. Such observations are the ideal test case for comparisons with theoretical formation models.

Another point that has to be covered by formation models is the structure of the young cluster systems as a whole: In the Large Magellanic Cloud, more than 10% of the young objects are binary clusters (Dieball & Grebel 2000). There are hints that these binary clusters formed approximately at the same time from one single giant molecular cloud (Dieball, Grebel & Theis 2000). Bhatia & MacGillivray (1988) even give possible evidence for a merging binary star cluster. On the other hand, observations of the young double cluster NGC 1850 by Gilmozzi et al. (1994) give hints that the smaller subcluster is considerably younger and may result from induced star formation caused by the gas expulsion of the main cluster (see Figure 2.4, left).

The residual gas left over from star formation will leave the system after a few dynamical timescales as suggested e.g. by observations of the gas-free young clusters (see also Figure 2.4, left). This gas expulsion is probably caused by feedback of young massive stars, like ionizing radiation, stellar winds or supernova explosions. The effect on the evolution of massive stellar clusters will be examined in detail in Chapter 5. Gas expulsion from open clusters in our Galaxy can be observed at the very moment (see Figure 2.4, right).

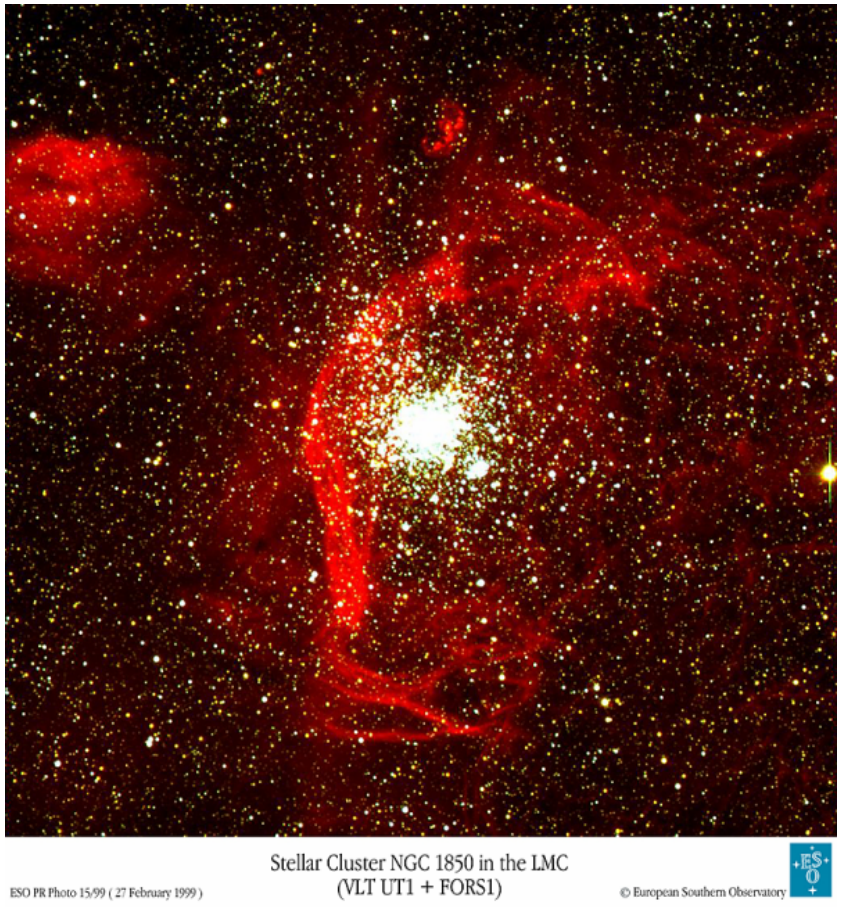

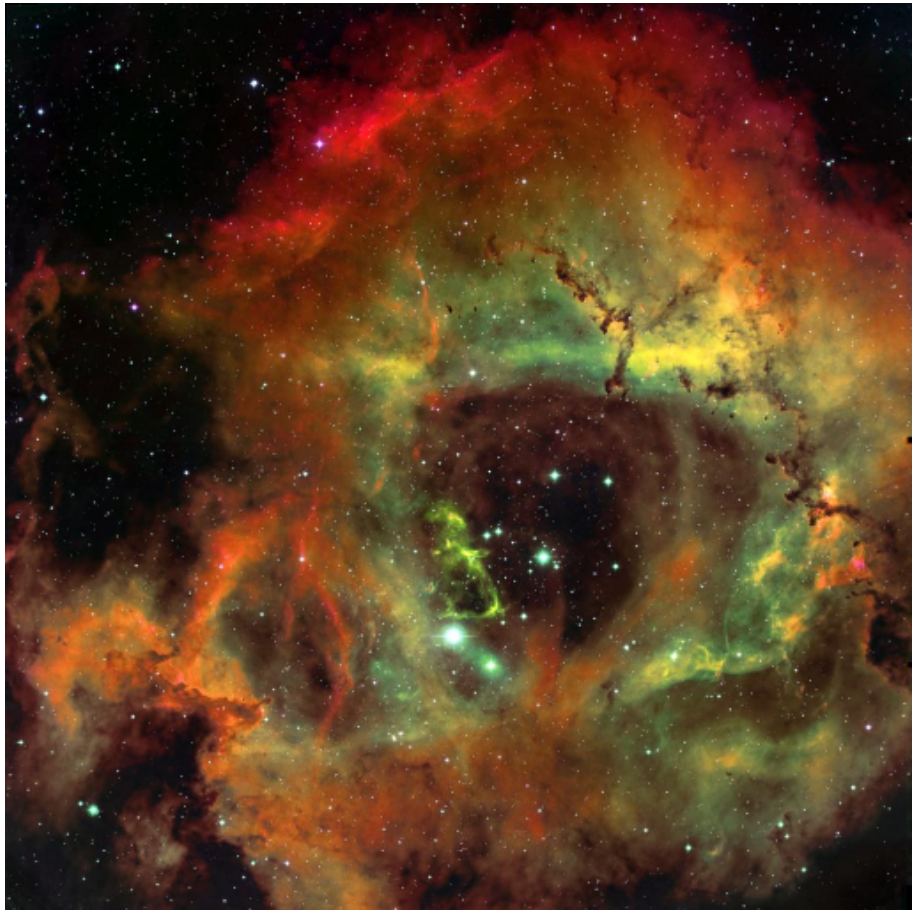

Figure 2.4: ***Left:*** *The young double cluster NGC 1850 in the Large Magellanic Cloud; the formation of the smaller cluster may have been induced by the gas expelled from the main cluster. Credit: VLT UT1 + FORS1, ESO PR Photo 15/99 (27 February 1999).* ***Right:*** *The Rosette Nebula in Hydrogen, Oxygen, and Sulfur; the central star cluster currently expels its residual gas and has already blown a hole into the surrounding medium. Credit: T. A. Rector, B. Wolpa, M. Hanna (AURA/NOAO/NSF).*

Chapter 3

Basic Physical Concepts and Numerical Methods

The complex evolution of astronomical problems like N–body systems or the gas dynamics of the interstellar medium often can be solved only by numerical simulations. The numerical results can be compared to actual observations. Through this cooperation, valuable new insights into the physical understanding can be gained. This chapter describes the numerical techniques that are used in this thesis:

Pure N–body methods are a useful tool to simulate the dynamical evolution of a large amount of gravitationally interacting point masses. Beyond that, this method will be extended to simulate the influence of a hydrodynamical gas on an embedded N–body system by applying external forces.

For simulations of molecular clouds and star formation, the proper treatment of the hydrodynamical gas is essential. We use Smoothed Particle Hydrodynamics (SPH), because of its unique ability to follow the dynamical evolution of fragmenting gas clouds over a wide range of scale lengths. SPH is intrinsically a particle method and makes way for a straight forward idealized star formation and stellar feedback implementation.

In the first section of this chapter we derive the hydrodynamic equations needed for the description of physical gases. In the following section we present the gravitational N–body problem and its connections to the hydrodynamic equations. The chapter ends with a description of the used SPH, N–body and combined SPH & N–body codes.

3.1 The Hydrodynamic Equations Derived from the Boltzmann Equation

In the following, we derive the basic ideas of hydrodynamics. The macroscopic physics of gases is successfully described by just one equation – the Boltzmann equation:

$$\frac{d}{dt} f(\vec{r}, \vec{v}, t) = \mathcal{C} f(\vec{r}, \vec{v}, t) \,. \tag{3.1.1}$$

The distribution function $f(\vec{r}, \vec{v}, t)$ is defined such that $f(\vec{r}, \vec{v}, t)\, d^3r\, d^3v$ gives the number of gas molecules inside the phase space volume $\mathcal{P}$ defined by $[\vec{r} \ldots \vec{r} + d\vec{r}]$ and $[\vec{v} \ldots \vec{v} + d\vec{v}]$ at time t. The total derivative is d/dt. The following derivations are explained in detail by Reif (1987).

In hydrodynamics, collisions between gas particles play an important role. In Equation (3.1.1) they are described by the operator $\mathcal{C}$ acting on the distribution function $f(\vec{r},\vec{v},t)$. Gas molecules can be scattered into or away from the observed phase space volume $\mathcal{P}$. We assume that the particle density is low enough, so that only two-body interactions are of importance and the velocities of the molecules before a collision are uncorrelated. Additionally, we neglect the influence of external forces on the scattering cross section and suppose that the distribution function stays approximately constant during the interaction time and inside the space volume defined by the scope of the interaction forces. One can find that the collisional term is given by

$$\mathcal{C}f(\vec{r},\vec{v},t) = \int\limits_{\vec{v}_1}\int\limits_{\Omega'} d\Omega'\, d^3v_1\, (f(\vec{r},\vec{v}',t)\, f(\vec{r},\vec{v}_1',t) - f(\vec{r},\vec{v},t)\, f(\vec{r},\vec{v}_1,t))\, |\vec{v}-\vec{v}_1|\, \sigma(\vec{v}'-\vec{v}_1')\,, \quad (3.1.2)$$

where $\vec{v},\vec{v}_1$ and $\vec{v}',\vec{v}_1'$ are the velocities of the two molecules before and after the collision, respectively. Because of momentum conservation, the scattered velocities $\vec{v}',\vec{v}_1'$ are functions of $\vec{v},\vec{v}_1$ and the scattering angle Ω'. The differential scattering cross section of two particles with the relative velocity $\vec{v}'-\vec{v}_1'$ is $\sigma(\vec{v}'-\vec{v}_1')$. The integration covers all possible velocities $\vec{v}_1$ and solid angles. The neglect of collisions involving three or more molecules shows up in Equation (3.1.2): Only second order products of the distribution function $f(\vec{r},\vec{v},t)$ appear.

The basic idea of hydrodynamics is to consider only the observable macroscopic spatial and time dependent properties of the system. These are obtained by averaging microscopic properties $\mathcal{G}(\vec{r},\vec{v},t)$ over the velocity space weighted with the distribution function:

$$<\mathcal{G}(\vec{r},t)>_{\vec{v}} = \frac{1}{n(\vec{r},t)} \int\limits_{\vec{v}} d^3v\, f(\vec{r},\vec{v},t)\, \mathcal{G}(\vec{r},\vec{v},t)\,, \quad (3.1.3)$$

where $n(\vec{r},t)$ represents the particle density.

Multiplying the left hand side of the Boltzmann Equation (3.1.1) (using Einstein summation convention from now on; r_i and v_i represent the components of the spatial position and velocity, respectively)

$$\frac{df}{dt} = \frac{\partial f}{\partial t} + \frac{dr_i}{dt}\frac{\partial f}{\partial r_i} + \frac{dv_i}{dt}\frac{\partial f}{\partial v_i} \quad (3.1.4)$$

by $\mathcal{G}$ and averaging over the velocity space we get after some mathematics

$$<\mathcal{G}\,\frac{d}{dt}\,f>_{\vec{v}} = \frac{\partial}{\partial t}(n\ <\mathcal{G}>_{\vec{v}}) + \frac{\partial}{\partial r_i}(n\ <v_i\,\mathcal{G}>_{\vec{v}}) - n\ <\frac{d}{dt}\,\mathcal{G}>_{\vec{v}}\ . \quad (3.1.5)$$

To compute the collisional term on the right hand side of Equation (3.1.1), we make use of the equality $\int d\Omega\, \sigma(\vec{v}'-\vec{v}_1') = \int\int d^3v'\, d^3v_1'\, \sigma(\vec{v},\vec{v}_1 \to \vec{v}',\vec{v}_1')$:

$$<\mathcal{G}\,\mathcal{C}f>_{\vec{v}} = \int\limits_{\vec{v}}\int\limits_{\vec{v}_1'}\int\limits_{\vec{v}'}\int\limits_{\vec{v}_1'} d^3v\, d^3v'\, d^3v_1\, d^3v_1' \cdot$$
$$(f(\vec{r},\vec{v}',t)\, f(\vec{r},\vec{v}_1',t) - f(\vec{r},\vec{v},t)\, f(\vec{r},\vec{v}_1,t))\, |\vec{v}-\vec{v}_1|\, \sigma(\vec{v},\vec{v}_1 \to \vec{v}',\vec{v}_1')\, \mathcal{G}(\vec{r},\vec{v},t)\,. \quad (3.1.6)$$

Scattering processes are symmetric under permutation of $(\vec{v}, \vec{v}_1) \leftrightarrow (\vec{v}', \vec{v}_1')$ (inverse collision). Next, the integration allows the formal permutation of $(\vec{v}, \vec{v}') \leftrightarrow (\vec{v}_1, \vec{v}_1')$. Applying both substitutions to Equation (3.1.6) leads to a total of three equal expressions for $<\mathcal{G}\,\mathcal{C}f>_{\vec{v}}$. Summing these up, we get

$$<\mathcal{G}\,\mathcal{C}f>_{\vec{v}} = \frac{1}{2}\int\limits_{\vec{v}}\int\limits_{\vec{v}_1}\int\limits_{\vec{\Omega}'} d^3v\, d^3v_1\, d\Omega'\, f(\vec{r},\vec{v},t)\, f(\vec{r},\vec{v}_1,t))|\vec{v}-\vec{v}_1|\,\sigma(\vec{v}'-\vec{v}_1')\,\Delta\mathcal{G} \tag{3.1.7}$$

with $\Delta\mathcal{G} = \mathcal{G}(\vec{r},\vec{v}',t) + \mathcal{G}(\vec{r},\vec{v}_1',t) - \mathcal{G}(\vec{r},\vec{v},t) - \mathcal{G}(\vec{r},\vec{v}_1,t)$.

It is straightforward to see that conservation laws can be derived for the special cases where $\Delta\mathcal{G} = 0$. The collisional term (3.1.7) of the integrated Boltzmann Equation $<\mathcal{G}\,\frac{d}{dt}\,f>_{\vec{v}} = <\mathcal{G}\,\mathcal{C}f>_{\vec{v}}$ cancels out and only the left hand side, Equation (3.1.5) remains:

$$n\,<\frac{d}{dt}\,\mathcal{G}>_{\vec{v}} - \frac{\partial}{\partial t}\,<n\,\mathcal{G}>_{\vec{v}} - \frac{\partial}{\partial r_i}\,<n\,v_i\,\mathcal{G}>_{\vec{v}} = 0\,. \tag{3.1.8}$$

The scattering process conserves the total mass, the total momentum, the total angular momentum and, assuming that there are no internal degrees of freedom of the individual molecules, the total kinetic energy of the participating particles. Thus, Equation (3.1.8) is valid for

$$\begin{aligned} \mathcal{G} &= m_\mu \\ \mathcal{G} &= m_\mu\, v_j \quad j = 1,2,3 \\ \mathcal{G} &= m_\mu\, \epsilon_{ijk}\, r_j\, v_k \quad i = 1,2,3 \\ \text{and}\quad \mathcal{G} &= \frac{1}{2}\, m_\mu\, \vec{v}^2\,. \end{aligned} \tag{3.1.9}$$

Here m_μ is the molecular mass and ϵ_{ijk} the Levi–Cevita tensor. In detail, from Equation (3.1.8) we get the following conservation laws:

Mass Conservation

Let $\mathcal{G} = m_\mu$. With the flow velocity $\vec{u}(\vec{r},t) = <\vec{v}>_{\vec{v}}$ and the gas density $\rho(\vec{r},t) = m_\mu\, n(\vec{r},t)$ we immediately get the continuity equation or the macroscopic conservation of mass:

$$\frac{\partial\rho}{\partial t} + \vec{\nabla}(\rho\,\vec{u}) = 0\,. \tag{3.1.10}$$

Momentum Conservation

Now, let $\mathcal{G} = m_\mu\, v_j$. The total derivative of the microscopic velocity, which is the acceleration, is equal to the external force per mass: $dv_i/dt = F_i/m_\mu$. Thus, Equation (3.1.8) leads to

$$\frac{\partial}{\partial t}(\rho\, u_j) + \frac{\partial}{\partial r_i}(\rho\, <v_i\, v_j>_{\vec{v}}) = \rho\,\mathcal{F}_j\,, \tag{3.1.11}$$

where $\vec{\mathcal{F}} = \vec{F}/m_\mu$ is the force per mass unit, which, in case of e.g. gravitation, is independent of the velocity. This holds for the density ρ, too. Thus both quantities are not affected by the

averaging over the velocity. We define $\vec{w}$ as the particle velocity with respect to the flow velocity $\vec{u}$, therefore $\vec{v} = \vec{u} + \vec{w}$. Keeping in mind that $\vec{u} = <\vec{v}>_{\vec{v}}$ and $<\vec{w}>_{\vec{v}} = 0$, we know that mixed terms like $<u_i\, w_j>_{\vec{v}} = 0$. We therefore replace

$$\rho\, <v_i\, v_j> = \rho u_i\, u_j + P_{ij} \quad \text{with} \quad P_{ij} = \rho\, <w_i\, w_j> \tag{3.1.12}$$

in the second term of Equation (3.1.11) and get

$$\frac{\partial}{\partial t}(\rho\, u_j) + \frac{\partial}{\partial r_i}(\rho\, u_i\, u_j) + \frac{\partial P_{ji}}{\partial r_i} = \rho\, \mathcal{F}_j\,. \tag{3.1.13}$$

It can be shown (e.g. Lüst 1978) that the stress tensor P_{ji} can be decomposed into a sum of the hydrostatic stress tensor, which includes the gas pressure p and the viscous stress tensor: $P_{ij} = p\, \delta_{ij} + \sigma_{ij}$. We get

$$\frac{\partial}{\partial t}(\rho\, u_j) + \frac{\partial}{\partial r_i}(\rho\, u_i\, u_j) + \frac{\partial p}{\partial r_j} + \frac{\partial \sigma_{ij}}{\partial r_i} = \rho\, \mathcal{F}_j\,. \tag{3.1.14}$$

By introducing the momentum flux tensor $\overleftrightarrow{\Pi} = \rho\, \vec{u} \circ \vec{u} + \overleftrightarrow{P}$ we get the short form of the momentum equation:

$$\frac{\partial(\rho\, \vec{u})}{\partial t} + \overleftrightarrow{\nabla}\overleftrightarrow{\Pi} = \rho\, \vec{\mathcal{F}}\,, \tag{3.1.15}$$

where we define the tensor divergence as $(\overleftrightarrow{\nabla})_{ij} = \partial/\partial r_i$. In a Newtonian medium, the components of the stress tensor are proportional to the velocity gradient: $\sigma_{ij} = A_{ijkl}\, \partial u_k/\partial x_l$. Assuming that σ_{ij} is isotropic (thus it vanishes for rigid body rotation) and symmetric in i and j, the most general form for the tensor A_{ijkl} is

$$A_{ijkl} = a\, \delta_{ij}\, \delta_{kl} + b\, (\delta_{ik}\, \delta_{jl} + \delta_{il}\, \delta_{jk}) \tag{3.1.16}$$

and we have

$$\sigma_{ij} = \eta\, (\frac{\partial u_j}{\partial r_i} + \frac{\partial u_i}{\partial r_j}) + (\zeta - \frac{2}{3}\, \eta)\, \delta_{ij}\, \frac{\partial u_l}{\partial r_l}\,, \tag{3.1.17}$$

by introducing the shear viscosity $\eta = a$ and bulk viscosity $\zeta = b + 2\, a/3$. This form of the momentum equation describes the hydrodynamics of viscous media.

Energy Conservation

In the case $\mathcal{G} = m_\mu\, v_i\, v_i/2$ (kinetic particle energy) we get, using again $v_i = u_i + w_i$,

$$\begin{aligned} &\rho\, \vec{u}\, \vec{\mathcal{F}} - \frac{1}{2}\, \frac{\partial}{\partial t}\, \rho\, \vec{u}^2 - \frac{1}{2}\, \frac{\partial}{\partial r_i}\, \rho\, u_j\, \vec{u}^2 - \frac{\partial}{\partial r_i}\, u_j\, P_{ij} \\ &\quad - \frac{1}{2}\, \frac{\partial}{\partial t}\, \rho\, <\vec{w}^2>_{\vec{v}} - \frac{1}{2}\, \frac{\partial}{\partial r_i}\, \rho\, <w_i\, \vec{w}^2>_{\vec{v}} - \frac{1}{2}\, \frac{\partial}{\partial r_i}\, \rho u_i\, <\vec{w}^2>_{\vec{v}} = 0\,. \end{aligned} \tag{3.1.18}$$

We can identify the internal energy per mass $\epsilon_{\rm int} = \rho\, <\vec{w}^2>_{\vec{v}}\, /2$ and the conduction heat flux $F_i = \rho\, <w_i\, \vec{w}^2>_{\vec{v}}\, /2$. Above equation can be decomposed into the conservation of the

kinetic energy, connected with the velocity flow $\vec{u}$, and the conservation of the internal energy, connected with the individual motions $\vec{w}$.

Additionally, we need one more equation to solve our system: The equation of state, which connects pressure, density and temperature: $p = p(\rho, T)$. In our case of the interstellar medium, we choose the ideal gas law $p = \rho\, R_{\rm gas}\, T/\mu$, where μ is the mean molecular weight, $R_{\rm gas}$ the universal gas constant and T the temperature of the gas.

Now we have derived the complete system of the hydrodynamic equations. In our case, the only "external" force is gravitation, which is caused by the gas itself. Therefore, we introduce the gravitational potential Φ, which is given by the Poisson equation

$$\triangle\Phi = 4\,\pi\, G\,\rho\,, \tag{3.1.19}$$

where G is the universal gravitational constant. The force per mass or acceleration on a massive particle is given by $\vec{\mathcal{F}} = -\vec{\nabla}\Phi$.

In summary, the following set of equations describes the macroscopic behaviour of a gaseous system, where $D/Dt = \partial/\partial t + \vec{u}\,\vec{\nabla}$ is the Lagrangian substantial derivative:

Continuity equation:

$$\frac{D\rho}{Dt} + \rho\,\vec{\nabla}\vec{u} = 0 \tag{3.1.20}$$

Equation of motion: Using the mass conservation equation times the velocity, one gets from Equation (3.1.15) the equation of motion

$$\rho\,\frac{D\vec{u}}{Dt} + \vec{\nabla}p + \overleftrightarrow{\nabla}\overleftrightarrow{\sigma} = -\,\rho\,\vec{\nabla}\Phi \tag{3.1.21}$$

Energy equation:

$$\frac{\partial}{\partial t}\,(\frac{1}{2}\,\rho\,\vec{u}^2 + \epsilon_{\rm int}) + \frac{\partial}{\partial r_i}\,(\frac{1}{2}\,\rho\,u_j\,\vec{u}^2 + F_i + u_i\,\epsilon_{\rm int} + \frac{\partial}{\partial r_i}\,u_j\,P_{ij}) = -\rho\,\vec{u}\,\vec{\nabla}\Phi\,, \tag{3.1.22}$$

with $j = 1, 2, 3$.
Poisson equation:

$$\triangle\Phi = 4\,\pi\, G\,\rho \tag{3.1.23}$$

Equation of state:

$$p = p(\rho, T) = \frac{\rho}{\mu}\,R_{\rm gas}\,T \tag{3.1.24}$$

3.2 Collisionless Systems

If the constituents of a medium only show gravitational interactions, we deal with a pure N–body system. In such systems, collisions only play a role if the system evolves over a time that is much larger than the relaxation timescale (Binney & Tremaine 1987)

$$t_r = \frac{N}{8 \ln N} t_d \quad \text{with} \quad t_d = \sqrt{\frac{1}{G \bar{\rho}}}, \tag{3.2.25}$$

where t_d is the typical crossing or dynamical timescale of the system, N the number of individual particles and $\bar{\rho}$ the average density inside a typical volume of the system. The "typical volume" is often defined as the innermost volume containing half the mass of the system. The relaxation timescale gives an estimation for the time after which one particle completely lost information about its initial dynamical properties due to interactions with the other particles. As we investigate the early evolution of stellar clusters, the evolution time is always less than the relaxation timescale. Thus, regarding the stellar part, collisions can be neglected. If the number of interacting particles is large, we can describe the system statistically by the collisionless Boltzmann Equation (compare Equation (3.1.1))

$$\frac{d}{dt} f(\vec{r}, \vec{v}, t) = 0 . \tag{3.2.26}$$

Here $f(\vec{r}, \vec{v}, t)$ is understood as the distribution function for one particle species with the individual masses m_i.

By integrating over moments of the Boltzmann equations, like in section 3.1, but omitting the collisional terms, we get the Jeans Equations, which are similar to the hydrodynamic equations without the pressure term (Binney & Tremaine (1987)). Using the particle density $n = \rho/m_i$ we infer from Equation (3.1.20) the continuity equation

$$\frac{\partial n}{\partial t} + \vec{\nabla}(n \, \vec{u}) = 0 . \tag{3.2.27}$$

The equation of motion (3.1.21) leads to

$$n \frac{\partial \vec{u}}{\partial t} + n \, (\vec{u}\vec{\nabla}) \, \vec{u} = - \frac{1}{m_i} \overleftrightarrow{\nabla} \overleftrightarrow{\sigma} - n \vec{\nabla} \Phi , \tag{3.2.28}$$

where $\overleftrightarrow{\sigma}$ is again the stress tensor.

Bound star clusters, if in a first approximation assumed collisionless, will be in a stationary condition, that is their distribution functions do not evolve in time. We need a tool to theoretically describe such distributions.

We define an integral of motion I as any function of the phase-space coordinates $\vec{r}$ and $\vec{v}$ that is constant in time

$$\frac{d}{dt} I(\vec{r}(t), \vec{v}(t)) = \frac{\partial I}{\partial \vec{r}} \frac{d\vec{r}}{dt} + \frac{\partial I}{\partial \vec{v}} \frac{d\vec{v}}{dt} = 0 . \tag{3.2.29}$$

By comparing to Equation (3.1.4), we see that this equals the condition for a stationary solution of the Boltzmann equation. We conclude that any stationary solution of the Boltzmann equation

Table 3.1: *Scale Factors*

code units		scale factor	physical units
mass	M'	$\hat{M}$	$M = \hat{M}\, M'$
length	L'	$\hat{L}$	$L = \hat{L}\, L'$
time	t'	$\hat{t} = \sqrt{\hat{L}^3/(G\,\hat{M})}$	$t = \hat{t}\, t'$
velocity	v'	$\hat{v} = \sqrt{G\,\hat{M}/\hat{L}}$	$v = \hat{v}\, v'$
density	ρ'	$\hat{\rho} = \hat{M}/\hat{L}^3$	$\rho = \hat{\rho}\, \rho'$
energy	E'	$\hat{E} = \hat{M}^2\, G/\hat{L}$	$E = \hat{E}\, E'$
energy per mass	$\epsilon' = E'/M'$	$\hat{\epsilon} = \widehat{(E/M)} = G\,\hat{M}/L_0$	$\epsilon = E/M = \widehat{(E/M)}\, E'/M'$
energy per volume	E'/L'^3	$\widehat{(E/L^3)} = G\,\hat{M}^2/\hat{L}^4$	$E/L^3 = \widehat{(E/L^3)}\, E'/l'^3$
temperature	$T' = \epsilon'$	$\hat{T} = G\hat{M}\,\mu/(\hat{L}\, R_{\rm gas}\,\bar{\gamma})$	$T = \hat{T}\, T'$
pressure	p'	$\hat{p} = G\hat{M}^2/\hat{L}^4$	$p = \hat{p}\, p'$
Grav.const.	$G' = 1$		$G = 6.6726 \cdot 10^{-11}\mathrm{N\,m^2\,kg^{-2}}$
Gas const.	$R'_{\rm gas} = 1/\bar{\gamma}$		$R_{\rm gas} = 8.3145\,\mathrm{J\,K^{-1}\,mol^{-1}}$

depends only on integrals of motion. Vice versa, any distribution function f, only depending on integrals of motion, is a stationary solution (**Jeans Theorem**). Three well-known integrals of motion are the total energy and the components of the angular momentum.

3.3 Scaling of Physical Systems & Code Units

In gravitational or hydrodynamical systems we have the freedom to use arbitrary scale factors. This enables us to compare one single numerical simulation with different examples in nature. Additionally, this allows us to convert the absolute values into the number range which is best fitted for the computer architecture.

In pure gravitational systems we can choose a scale factor $\hat{M}$ for the mass and $\hat{R}$ for the length. For convenience, we build our conversions such that the gravitational constant is equal to 1 in code units. In hydrodynamical systems, we additionally have the freedom to demand that the mass per energy and the temperature have the same absolute values in code units.

However, If we put additional physical parameters into the simulations, like energy feedback, we will have to convert the constants into code units, thus fixing the scale factors. By dimensional argumentations we can find the appropriate scale factors given in table 3.1. In this units, the equation of state of the ideal gas reads $p' = \rho'\, T'/\bar{\gamma}$ and the isothermal sound speed is given by $p' = a'^2_T\, T'$ or $a'_T = \sqrt{T'/\bar{\gamma}}$. Here, $\bar{\gamma} = 1/(\gamma - 1)$, where γ is the constant adiabatic exponent. For an ideal gas, $\bar{\gamma} = 3/2$.

In the following, we mark the scale factors with a hat. Where it is obvious from the context, no distinction is made between physical and dimensionless code variables. In case of doubt, code units are marked with an apostrophe.

3.4 Numerical Simulations of Collisionless N–body Particles

In this thesis, two different kinds of simulations are presented: Pure N–body simulations and combined hydrodynamical & N–body Simulations. The numerical schemes will be presented in the two following sections.

3.4.1 Time Integration

Although it is possible to get the dynamical evolution of the system by a direct evaluation of the Boltzmann Equation (e.g. Fokker-Planck methods, for a recent review see Baumgardt (2001)) in many cases the Monte-Carlo approach of an N–body particle system is more useful regarding computational aspects. We construct an N–body realization of the system by assigning phase space coordinates $\vec{r}$ and $\vec{v}$ as well as masses m_i to an ensemble of N particles, such that the mass inside a given finite phase space volume $\mathcal{P}$ is equal in both cases:

$$\iint_{\mathcal{P}} \tilde{f}(\vec{r},\vec{v},t) = \sum_{i\in\mathcal{P}} m_i \,, \tag{3.4.30}$$

where the sum goes over all particles inside $\mathcal{P}$.

Here we use the mass distribution function $\tilde{f}(\vec{r},\vec{v},t)$, which gives the total mass inside the phase space volume $[\vec{r}\ldots\vec{r}+d\vec{r}]$ and $[\vec{v}\ldots\vec{v}+d\vec{v}]$ at time t.

If we choose an equal mass realization with $m_i = \int\int d^3v\, d^3r\, \tilde{f}(\vec{r},\vec{v},t)/N$, the mass distribution function $\tilde{f}(\vec{r},\vec{v},t)$ essentially depends on the phase space number density of particles and we can choose our realization by selecting phase space coordinates $\vec{r}$ and $\vec{v}$ according to the probability which is proportional to $\tilde{f}(\vec{r},\vec{v},t)$.

The evolution of these bodies is determined by the Newtonian equations of motion, which form a set of differential equations

$$\frac{d\vec{v}_i}{dt} = \vec{\mathcal{F}}(\vec{r}_i) \quad \text{and} \quad \frac{d\vec{r}_i}{dt} = \vec{v}_i \,, \tag{3.4.31}$$

where $\mathcal{F}(\vec{r}_i)$ is the specific force, only depending on the particle position $\vec{r}_i$, as we deal with gravitation only. Thus, we have to solve the system of differential equations

$$\frac{d}{dt}\,\vec{y} = \dot{\vec{y}} = \vec{f}(t,\vec{y}) \quad \text{with} \quad \vec{y} = \begin{pmatrix} \vec{r} \\ \vec{v} \end{pmatrix} \quad \text{and} \quad \vec{f} = \begin{pmatrix} \vec{v} \\ \vec{\mathcal{F}}(\vec{r}) \end{pmatrix} . \tag{3.4.32}$$

We use the leapfrog method which implements the time symmetric step $\vec{y}(t+\delta t/2) = \vec{y}(t-\delta t/2) + \delta t\vec{f}(t,\vec{y}(t))$. Using the definitions in (3.4.32) and shifting the equation involving $\vec{r}_i$ by $\delta t/2$ we get the scheme

$$\vec{v}_i(t+\delta t/2) = \vec{v}_i(t-\delta t/2) + \delta t\,\vec{\mathcal{F}}(\vec{r}_i) \tag{3.4.33}$$

and

$$\vec{r}_i(t+\delta t) = \vec{r}_i(t) + \delta t\,\vec{v}_i(t+\delta t/2)\,. \tag{3.4.34}$$

With an expansion in a Taylor series, one can show that the leapfrog scheme is second order accurate.

3.4.2 Self–Gravity: Treecode & GRAPE

In pure gravitational systems, the force per mass acting on a particle is given by the gradient of the gravitational potential $\mathcal{F} = -\vec{\nabla}_{\vec{r}}\Phi$. The potential itself is given by the Poisson equation

$$\triangle_{\vec{r}}\Phi = 4\,\pi\,G\,\rho\,. \tag{3.4.35}$$

In the case of a set of infinitesimal small point masses, we get the force acting on particle i by a superposition of the Newtonian forces caused by all other particles:

$$\vec{F}_i = \sum_{j,\,j\neq i}^{N} \frac{G\,m_i\,m_j}{|\vec{r}_j - \vec{r}_i|^2}\,\frac{\vec{r}_j - \vec{r}_i}{|\vec{r}_j - \vec{r}_i|}\,. \tag{3.4.36}$$

A direct implementation of this force term fails on encounters between two or more N–bodies: If the distance of two particles is too low, the forces and thus the acceleration and velocities will be huge, requiring very low time steps that would make the code too inefficient. As our simulations only take place in the collisionless regime, we can neglect N–body encounters and apply the widely-used Plummer smoothing

$$\vec{F}_i = \sum_{j,\,j\neq i}^{N} \frac{G\,m_i\,m_j(\vec{r}_j - \vec{r}_i)}{(|\vec{r}_j - \vec{r}_i|^2 + \epsilon^2)^{3/2}}\,, \tag{3.4.37}$$

which avoids the divergences for small distances. The smoothing parameter ϵ should be of the order of the mean interparticle distance. With smoothing, systems containing a huge number of particles can be described by simulations using only a small number of N–bodies: The smoothing increases the numerical relaxation time (3.2.25) of the N–body system. As long as the evolution time of the N–body system is less than the relaxation time of the physical system, the numerical simulation describes well the real evolution.

Even in pure N–body codes, one can study the influence of e.g. a gaseous environment by superposition of a suitable external potential. Then the external force $\vec{F}_{\mathrm{i,ext}}$ is added to the inter-particle forces (3.4.37) for each particle:

$$\vec{F}_{\mathrm{i,tot}} = \vec{F}_i + \vec{F}_{\mathrm{i,ext}}\,. \tag{3.4.38}$$

For a system consisting of N particles, using the direct summation (3.4.37), the computational effort scales as N^2. Deriving the gravitational potential of a self–gravitating system is the most time consuming step in the simulation of a gravitational system and thus limits the number of particles that can be used. To speed up the computation, we present two possible solutions: The hardware device GRAvity piPE (GRAPE) and the Tree method.

The GRAPE board releases the host computer from the force computation. This is done by a hardwired 'pipe'-system which allows the simultaneous computation of several two-body forces and its summation over all pairs (Okumura et al. 1993; Umemura et al. 1993; Steinmetz 1996; Makino et al. 1997).

The second way reducing the computational effort, the tree mechanism, was proposed by Barnes & Hut (1986). Here the number of computations scales with $N \ln N$. Performance

characteristics of tree codes by Hernquist (1987) show that the method is well suited for collisionless systems.

All particles of the ensemble are arranged on a hierarchical binary tree. The tree is constructed starting with the particles as leaves (first level). On the second level, all mutual particle neighbours are grouped together to nodes. On the next level, mutual neighbours among nodes plus particles left over from the foregoing levels are grouped together and also replaced by nodes. This procedure is repeated until the top level of the tree is reached, consisting of only one node which contains all the particles of the ensemble. In total, we get $2N-1$ positions in the tree. The tree represents the physical clumping of the system, which allows a fast search for neighbours needed for the SPH algorithm described in the following section.

To speed up the computation of the gravitational force on particle i, we do not compute the contributions of all other particles separately, but use the joint properties of a higher level node:

For every node n, the total mass $m_n = m_k + m_l$, the center of mass and its quadrupole moments are computed using masses m_k and m_l and positions $\vec{r}_k$ and $\vec{r}_l$ of its daughter nodes or particles k and l.

Now we need a criterion when to "open" a node, that is, when we have to use the components rather than the node itself. It has been useful to introduce an opening angle criterion

$$\frac{R_n}{r_{in}} = \Theta\,, \tag{3.4.39}$$

where the radius of a node is defined as

$$R_n = \max(\frac{m_i}{m_n}\,|\vec{r}_k - \vec{r}_l| + R_l, \frac{m_j}{m_n}\,|\vec{r}_k - \vec{r}_l| + R_k) \tag{3.4.40}$$

and r_{in} is the distance to the node. If the particle "sees" the node under an angle that is less than Θ, it is sufficient to compute the forces just with that node. Including quadrupole moments of the node decreases the error. In the other case, the node is expanded into its daughters and the opening angle criterion is applied recursively. In the limit $\Theta \to 0$ the method is exact. If Θ is too large, errors increase too much. A value of $\Theta = 0.5$ has proved to produce acceptable results and is chosen in this thesis.

3.5 Solving the Hydrodynamic Equations by Smoothed Particle Hydrodynamics

Smoothed Particle Hydrodynamics (SPH) is a Lagrangian method for the numerical integration of the hydrodynamic equations. Instead of a discrete grid describing the hydrodynamic properties of the fluid, in SPH the grid cells are replaced by *gas particles*, which carry mass, momentum and internal energy. These gas particles arrange themselves and build up their own computational grid. The hydrodynamical properties are obtained by averaging a sufficient number of gas particles inside the *smoothing kernel*. Detailed reviews on SPH have been published by Benz (1990) and Monaghan (1992). Mathematically, we replace the hydrodynamical partial differential equations by simpler ordinary ones.

We give a basic description of the SPH method and state the representations of the hydrodynamic equations. In the next chapter, the implementation of star formation and stellar feedback is explained in detail.

3.5.1 Basic Equations

In the SPH formalism, the hydrodynamical properties of the fluid are obtained by an averaging process: Convolution of the physical quantity $f(\vec{r})$ with a *kernel function* $W(\vec{r}-\vec{r}',h)$ gives the smoothed representation

$$\langle f(\vec{r})\rangle = \int\limits_{V(h)} W(\vec{r}-\vec{r}',h) f(\vec{r}') d^3r' \,. \tag{3.5.41}$$

The Kernel must be normalized,

$$\int\limits_{V(h)} W(\vec{r}-\vec{r}',h)\, d^3r' = 1\,, \tag{3.5.42}$$

and its width must scale with the smoothing length h, leading to

$$\lim_{h\to 0} W(\vec{r}-\vec{r}',h) = \delta(\vec{r}-\vec{r}')\,, \tag{3.5.43}$$

where $\delta(\vec{r}-\vec{r}')$ is the three dimensional Dirac's delta distribution. Hence, we have

$$\lim_{h\to 0} \langle f(\vec{r})\rangle = f(\vec{r})\,. \tag{3.5.44}$$

The integration in Equation (3.5.41) has to be taken over the entire volume $V(h)$ where the smoothing kernel is greater than zero. By adopting a spherical symmetric kernel, it can be shown that

$$\langle f(\vec{r})\rangle = f(\vec{r}) + c\,\frac{h^2}{6}\vec{\nabla}^2_{\vec{r}} f(\vec{r}) + \mathcal{O}(h^3)\,. \tag{3.5.45}$$

Therefore, replacing the exact scalars $f(\vec{r})$ by its smoothed representations $<f(\vec{r})>$ is accurate up to first order in the smoothing length h. To derive the hydrodynamic equations of motion in the SPH notation, one can also show that in first order

$$\frac{d}{dt}\,<f(\vec{r})> = <\frac{d}{dt}\,f(\vec{r})> \quad \text{and} \quad \vec{\nabla}\,<f(\vec{r})> = <\vec{\nabla}\,f(\vec{r})> \tag{3.5.46}$$

and

$$\left\langle \frac{A(\vec{r})}{B(\vec{r})} \right\rangle = \frac{\langle A(\vec{r})\rangle}{\langle B(\vec{r})\rangle} + O(h^2)\,. \tag{3.5.47}$$

The basic task to derive the equations of the SPH formalism is to evaluate integrals of the type

$$\int\limits_{V(h)} f(\vec{r}')\, W(\vec{r}-\vec{r}',h) d^3r' \,. \tag{3.5.48}$$

We use the idea of Monte-Carlo integration: For the evaluation of the integral

$$I = \int\limits_{V} g(\vec{r}') d^3r' \,, \tag{3.5.49}$$

where $g(\vec{r})$ is an arbitrary integrable scalar function, we use N sampling vectors $\vec{r}_i$ to get the sampling values $g_i = g(\vec{r}_i)$. The exact integral divided by the integration volume

$$\bar{I} = \int\limits_V \frac{1}{V}\, g(\vec{r}')d^3r' \tag{3.5.50}$$

and the mean of the sampling values

$$\bar{g} = \sum_{i\in\mathcal{N}} \frac{1}{N}\, g(\vec{r}_i) \tag{3.5.51}$$

will be equal if the number N of the vectors $\vec{r}_i$ is sufficient. The summation goes over the entire set $\mathcal{N} = [1, \ldots, N]$ of vectors. Thus,

$$\int\limits_V g(\vec{r}')d^3r' \simeq \sum_{i\in\mathcal{N}} \frac{V}{N}\, g(\vec{x}_i) = \sum_{i\in\mathcal{N}} \frac{1}{\nu}\, g(\vec{x}_i)\,. \tag{3.5.52}$$

In the last step, we introduced the spatial density ν of the sampling points.

In SPH, each of the points carries a given mass m_i. These points can be understood as *gas particles*, leading to the name *smoothed particle hydrodynamics*. If we use the density $\rho_i = \rho(\vec{r}_i) =< \rho(\vec{r}_i) >$, which is accurate to first order in h (see Equation (3.5.45)) the spatial density is $\nu_i = \rho_i/m_i$. Substituting $g(\vec{r}')$ by the product $f(\vec{r}')\, W(\vec{r} - \vec{r}', h)$ we have

$$< f(\vec{r}) >= \sum_{i\in\mathcal{N}} \frac{m_i}{\rho_i}\, f(\vec{r}_i)\, W(\vec{r} - \vec{r}_i, h)\,. \tag{3.5.53}$$

That's SPH :-) .

The smartness of SPH lies in the computation of the smoothed spatial gradient without making use of finite differences or a grid. Integrating

$$< \vec{\nabla}_{\vec{r}}\, f(\vec{r}) >= \int\limits_{V(h)} (\vec{\nabla}_{\vec{r}}\, f(\vec{r}'))\, W(\vec{r} - \vec{r}', h)d^3r' \tag{3.5.54}$$

by parts and neglecting the surface term, we have

$$< \vec{\nabla}_{\vec{r}}\, f(\vec{r}) >= \int\limits_{V(h)} f(\vec{r}')\, (\vec{\nabla}_{\vec{r}'}\, W(\vec{r} - \vec{r}', h))d^3r' \tag{3.5.55}$$

or, using Equation (3.5.53),

$$< \vec{\nabla}_{\vec{r}}\, f(\vec{r}) >= \sum_{i\in\mathcal{N}} \frac{m_i}{\rho_i}\, f(\vec{r}_i)\, \vec{\nabla}_{\vec{r}_i} W(\vec{r} - \vec{r}_i, h)\,. \tag{3.5.56}$$

For the evaluation of expressions of the type (3.5.53) or (3.5.56), we need the density ρ at the particle positions $\vec{r}$. We get this from

$$<\rho(\vec{r})>=\sum_{i\in\mathcal{N}} m_i\, f(\vec{r}_i)\, W(\vec{r}-\vec{r}_i,h)\,. \tag{3.5.57}$$

The gas particle mass is smoothed over the kernel volume.

The summation in the above equations has to be taken over the complete set of gas particles $\mathcal{N}=[1,\ldots,N]$. However, realizing that gas properties are local quantities, the computational effort can be decreased by choosing a suitable kernel function $W(\vec{r}-\vec{r}_i,h)$, which rejects particles outside the smoothing volume. We call the particles that lie inside the kernel of one particle its "neighbours". Then the summations in above equations have to be taken only over the list of neighbours $\mathcal{N}_j=[n_{j,1},n_{j,2},\ldots,n_{j,N_j}]$, with N_j being the number of neighbours of particle j. A suitable kernel, proposed by Monaghan & Lattanzio (1985), is the spherical symmetric spline kernel

$$W(r_{ij})=\frac{1}{\pi\, h^3}\begin{cases} 1-\frac{3}{2}\,v^2+\frac{3}{4}\,v^3 & \text{if} \quad 0\le v<1 \\ \\ \frac{1}{4}\,(2-v)^3 & \text{if} \quad 1\le v<2 \qquad \text{with} \quad v=\dfrac{r_{ij}}{h}\,. \\ \\ 0 & \text{if} \quad v\ge 2 \end{cases} \tag{3.5.58}$$

This kernel has compact support and thus limits the number of neighbours. In our code, the kernel and its derivatives are tabulated for fast access.

3.5.2 The Hydrodynamic Equations in SPH notation

In short, the principal SPH equations for computing physical quantities read

$$f_j=\sum_{i\in\mathcal{N}_j}\frac{m_i}{\rho_i}\,f_i\,W_{ji} \quad \text{and} \quad \left(\vec{\nabla}_{\vec{r}}\,f\right)_j=\sum_{i\in\mathcal{N}_j}\frac{m_i}{\rho_i}\,f_i\,\left(\vec{\nabla}_{\vec{r}_i}W\right)_{ji} \tag{3.5.59}$$

with

$$\rho_j=\sum_{i\in\mathcal{N}_j} m_i\, f_i\, W_{ji}\,, \tag{3.5.60}$$

where $f_i=f(\vec{r})$, $W_{ji}=W(\vec{r}_j-\vec{r}_i)$, etc.

We now derive the SPH implementation of the hydrodynamic equations:

Continuity Equation:

The continuity equation (3.1.20) is fulfilled automatically, as mass is conserved as long as no particles are lost or created during the simulation.

Equation of Motion:

The equation of motion (3.1.21) for one SPH particle j without viscosity and other forces reads

$$\frac{D\vec{u}_j}{Dt}=-\left(\frac{\vec{\nabla}p}{\rho}\right)_j-\left(\vec{\nabla}_{\vec{r}}\Phi\right)_j\,. \tag{3.5.61}$$

To evaluate the pressure gradient term, we use the symmetric form (Monaghan 1992) $(\vec{\nabla}p)/\rho = \vec{\nabla}(p/\rho) + p(\vec{\nabla}\rho)/\rho^2$ to get

$$\left(\frac{\vec{\nabla}p}{\rho}\right)_j = \sum_{i\in\mathcal{N}_j}\left(\frac{p_i}{\rho_i^2}+\frac{p_j}{\rho_j^2}\right) m_i \left(\vec{\nabla}_{\vec{r}_i}W\right)_{ji} . \tag{3.5.62}$$

The pressure itself is computed via the equation of state, knowing density and temperature (internal energy).

Artificial Viscosity:

In SPH, an artificial viscosity is necessary to prevent gas particles from penetrating each other and for the proper treatment of shock fronts. We use the artificial viscosity term described by Monaghan (1992):

$$\sum_{i\in\mathcal{N}_j} m_i \Gamma_{ji} \left(\vec{\nabla}_{\vec{r}_i}W\right)_{ji} . \tag{3.5.63}$$

where Γ_{ji} is given by

$$\Gamma_{ji} = \begin{cases} \dfrac{-\alpha\,(c_i+c_j)/2\,\mu_{ji}+\mu_{ji}^2}{(\rho_i+\rho_j)/2} & \text{if} \quad \vec{v}_{ji}\cdot\vec{r}_{ji}\le 0 \\ 0 & \text{if} \quad \vec{v}_{ji}\cdot\vec{r}_{ji}>0 \end{cases} \quad \text{with} \quad \mu_{ji}=\frac{h\,\vec{v}_{ji}\,\vec{r}_{ji}}{\vec{r}_{ji}^{\,2}+\epsilon^2} \tag{3.5.64}$$

Here, $\vec{r}_{ji}=\vec{r}_j-\vec{r}_i$, $\vec{v}_{ji}=\vec{v}_j-\vec{v}_i$ and c_i and c_j are the sound velocities at the particle positions. The parameter $\epsilon = 0.01\,h$ prevents divergences for small particle distances. The artificial viscosity only contributes to the equation of motion if the two particles are approaching each other ($\vec{v}_{ji}\cdot\vec{r}_{ji}>0$). The term linear in the velocity produces a bulk and shear viscosity, whereas the quadratic term helps handling high Mach number shocks. It vanishes for rigid body rotation like the stress tensor introduced in Equation (3.1.17) and conserves total linear and angular momenta (Monaghan 1992)

Energy Equation:

In our simulations, we restrict ourselves to an isothermal equation of state. We therefore do not integrate the energy equation (3.1.22) in time. However, an implementation for the adiabatic case can be found in Benz (1990).

Gravitation:

Due to the particle treatment of the gas dynamics, the implementation of self-gravity in SPH is straightforward: The gravitational acceleration $\vec{\mathcal{F}}=-\vec{\nabla}\Phi$ on gas particle j due to gas particles k is given by

$$\vec{\mathcal{F}}_j = \sum_{i\in\mathcal{N}} \frac{G\,\tilde{m}_k}{|\vec{r}_{kj}|^2}\,\vec{e}_{kj}\,, \tag{3.5.65}$$

where the unit vector is $\vec{e}_{kj}=\vec{r}_{kj}/|\vec{r}_{kj}|$. As the masses of SPH particles are smeared out over the kernel volume, particle j only sees the mass (assuming a spherical symmetric kernel)

$$\tilde{m}_k = \int_0^{r_{kj}} dr\, 4\,\pi\, r_{kj}^2\, \tilde{\rho}_k(r_{kj}) \tag{3.5.66}$$

of its neighbour k, where $\tilde{\rho}_k(r_{kj}) = m_k\, W_{kj}$ is the smeared out density distribution of particle k. We thus get the self-gravity term for the equation of motion as

$$\vec{\mathcal{F}}_j = \sum_{i \in \mathcal{N}} \frac{G\, m_k \tilde{W}_{kj}}{|\vec{r}_{kj}|^2}\, \vec{e}_{kj} \quad \text{with} \quad \tilde{W}_{kj} = \int_0^{r_{kj}} dr\, 4\,\pi\, r_{kj}^2\, W_{kj}\,. \tag{3.5.67}$$

For all particles outside the kernel volume we have $\tilde{W}_{kj} = 1$ and get the usual gravitational law. This states the fact that the gravitational force is a long-range force, such that the summation in (3.5.67) goes over the entire ensemble of particles. In consequence, the number of calculations needed to evaluate the self–gravity scales with the number of SPH particles as N^2.

To circumvent this numerical effort, we use the tree algorithm already described in Section 3.4.2. The implementation used here for the SPH code was originally developed by Press (1986) and is extensively described by Benz et al. (1990).

As already mentioned in Section 3.4.2, too, the hardware device GRAPE is another possibility to increase the computational speed. The code we used for the SPH simulations cannot handle gas and N–body-particles simultaneously when using GRAPE. Therefore, our gaseous simulations exclusively base on the tree method. A code making use of GRAPE for simulations with gas and N–bodies has been developed by Wetzstein et al. (2001) and will be of interest for future simulations.

Resolution Limits of SPH with Self-Gravity:

Bate & Burkert (1997) showed that SPH has a mass-limited resolution: In order to follow fragmentation processes properly, the mass resolution of the code, of the order of the mass inside one smoothing length h, must be sufficient to resolve the local Jeans mass. The rule of thumb that the smallest mass that a SPH code can resolve is twice the number of particle neighbours $N_{\rm neigh}$ leads to a maximum density that can be resolved:

$$\rho_{\rm crit} = \frac{15}{32\,\pi} \left(\frac{a^2}{G}\right)^3 \left(\frac{N}{N_{\rm neigh}\, M}\right)^2 . \tag{3.5.68}$$

Here, N is the total number of SPH particles, $a^2 = R_{\rm gas}\, T/\mu$ the square of the isothermal sound speed and M the total mass of the system. Whitworth (1998) analytically confirmed this result.

3.5.3 Variable Smoothing Length

Until now, the smoothing length h was thought to be constant in time and space. To fully take advantage of the abilities of SPH, we must note that, if we assume constant gas particle masses, in high density regions the number of particles is high, too. SPH generates its own adjustable "grid". The statistical errors in evaluating the integrals in the form (3.5.59) will be connected to the number of sample vectors or gas particles we use. It is therefore sufficient to use a smaller smoothing length in high density regions and a larger one in low density regions, respectively.

To keep the errors constant, we assign each gas particle i a smoothing length h_i such that the number of neighbours N_i is approximately constant in time. Given the smoothing length at time t, we can estimate the new smoothing length at time $t + \delta t$ by

$$h_i(t + \delta t) = h_i(t) \left(\frac{\rho_i(t)}{\rho_i(t + \delta t)} \right)^{1/3} . \tag{3.5.69}$$

We have the problem that to compute $h_i(t+\delta t)$ we need to know $\rho(t+\delta t)$ in advance – and vice versa. Benz (1990) suggests to use the time derivative dh_i/dt and evolve $h_i(t)$ in time. Using the Taylor expansion of $h_i(t + \delta t)$ and $\rho(t + \delta t)$ with respect to time we get

$$\frac{dh_i}{dt} = -\frac{h_i}{3\,\rho_i} \frac{d\rho_i}{dt} = \frac{h_i}{3} \vec{\nabla} \vec{v}_i \,. \tag{3.5.70}$$

In the last step we inserted the continuity equation (3.1.20). Thus we need to compute the velocity divergence at the particle positions. We use the symmetric form $\rho \vec{\nabla} \vec{v} = \vec{\nabla}(\rho\, \vec{v}) - \vec{v}(\vec{\nabla}\rho)$ and get

$$(\rho \vec{\nabla} \vec{v})_j = \sum_{i \in \mathcal{N}_j} \vec{v}_{ij} \left(\vec{\nabla}_{\vec{r}_i} W \right)_{ji} = \sum_{i \in \mathcal{N}_j} \frac{\vec{v}_{ij}\, \vec{r}_{ji}}{|\vec{r}_{ji}|} \left(\frac{\partial}{\partial r_i} W \right)_{ji} , \tag{3.5.71}$$

where we made use of the kernel gradient pointing in the direction of $\vec{r}_j - \vec{r}_i$.

To make sure that, even if systematic errors occur, the number of neighbours is approximately constant, corrections to the smoothing length are applied if the number falls below or rises beyond certain limits.

3.5.4 Time Evolution

We solve the system of differential equations for one particle

$$\frac{d}{dt}\, \vec{y} = \dot{\vec{y}} = \vec{f}(t, \vec{y}) \quad \text{with} \quad \vec{y} = \begin{pmatrix} \vec{r} \\ \vec{v} \end{pmatrix} \quad \text{and} \quad \vec{f} = \begin{pmatrix} \vec{v} \\ \vec{a}(t, \vec{r}, \vec{v}) \end{pmatrix} , \tag{3.5.72}$$

where $\vec{a}(t, \vec{r}, \vec{v})$ is the acceleration caused by the sum of all forces in the equation of motion. As the SPH formalism is of first order, the general first order Runge-Kutta formula (Kutta 1901) to predict the evolution of $\vec{y}$ is sufficient:

$$\vec{y}(t + \delta t) = \vec{y}(t) + \delta t\, c_0\, \vec{f}(t, \vec{y}(t)) + \delta t\, c_1\, \vec{f}(t + \alpha_1 \delta t, \vec{y} + \beta_1\, \delta t \vec{f}(t, \vec{y})) \,, \tag{3.5.73}$$

We use the Runge-Kutta-Fehlberg scheme (Fehlberg 1969), where the error is given by the difference to the next higher order Runge-Kutta formula. Expanding the right hand side of this second order formula into a Taylor series and comparing with the Taylor series of the first order formula above, we get the error term

$$E = |\dot{y}(t)\, \delta t^2\, (\alpha_1 c_1 - \frac{1}{2})| \,. \tag{3.5.74}$$

A more general description of the method is given by Stoer & Bulirsch (1990). In the Fehlberg scheme, we choose the remaining coefficients such that the error is small but not zero. If it was

zero, the pair of functions would degenerate, making it impossible to obtain the error. Fehlberg (1969) proposes $\alpha_1 = \beta_1 = 1/2$, $c_0 = 1/256$ and $c_1 = 255/256$. Thus, $E = |\dot{y}(t)\,\delta t^2\,1/512|$.

Concluding, our system is evolved by

$$\vec{r}_{\text{new}} = \vec{r} + \delta t\,\frac{1}{256}\,\vec{v} + \delta t\,\frac{255}{256}\,[\vec{v} + \frac{1}{2}\,\delta t\,\vec{a}(t,\vec{r},\vec{v})] \tag{3.5.75}$$

and

$$\vec{v}_{\text{new}} = \vec{v} + \delta t\,\frac{1}{256}\,\vec{a}(t,\vec{r},\vec{v}) + \delta t\,\frac{255}{256}\,\vec{a}(t+\frac{1}{2}\,\delta t, \vec{r}+\frac{1}{2}\,\delta t\,\vec{v}, \vec{v}+\frac{1}{2}\,\delta t\,\vec{a}(t,\vec{r},\vec{v}))\,. \tag{3.5.76}$$

The evolution of the smoothing length and the internal energy is done accordingly.

As our error is of second order, we must adapt our time step like $\delta t_{\text{new}} = \delta t\,\sqrt{E_{\text{tol}}/E}$ to make sure our error is smaller than a given tolerance E_{tol} (Press et al. 1999). If we approximate $\dot{y}(t) = (y(t+\delta t) - y(t))/\delta t$ we get the new time step

$$\delta t_{\text{new}} = \delta t\,\sqrt{\frac{512\,E_{\text{tol}}}{\delta t\,|y(t+\delta t) - y(t)|}}\,. \tag{3.5.77}$$

In our simulations, we chose $E_{\text{tol}} = 1.0\,10^{-5}$ in code units for all quantities, assuming that all physical variables are of the same order in code units. For $|y(t+\delta t) - y(t)|$ we take the largest absolut error of all quantities which are evolved in time.

In the previous section we argued that assuming different smoothing lengths for each of the particles is a natural extension of the SPH formalism. Like that, it is consequent to introduce individual timesteps for the particles: Gas particles in low density regions with slow dynamical evolution need, regarding the above given time step criterion, far smaller time steps than the ones in high density regions, and vice versa. By introducing individual timesteps, computing time is efficiently distributed among the particles, and SPH shows its full power in following simulations over large orders of density.

But evolving each particle with an arbitrary timestep would increase the computational effort for the time integration immensely. Bate (1995) introduced a timestep scheme, where particles are grouped together on predefined timestep bins L which have sizes $1/2^L$ times a fixed global timestep dt (Figure 3.1). Thereby, although allowing individual timesteps, with every substep whole groups of particles can be advanced together. With regard to the maximum allowed integer number in the code, we assign the maximum time step dt the integer 2^{20} (level $L = 0$). If we assign, to be on the safe side, the minimum step to 2^1 (level $L = 19$), the individual timesteps can be as low as $dt/2^L = 2^{-19}\,dt$. For the time integration of the particles on level L_i, the properties of lower level particles $L < L_i$ are linearly interpolated to the substep in order to compute the force terms correctly.

After each timestep, the time bin level for each particle is computed from the new timestep. Shifting the particle to lower levels is only possible, if its time is synchronized with the particles on the lower level (left arrow in Figure 3.1). We only allow changing to the adjacent level. If the new level is higher, the particle can be shifted at once to the new track, as synchronization is obviously fulfilled. Skipping intermediate levels is allowed (right arrow in Figure 3.1)

The individual timestep scheme makes it necessary to introduce two new timestep criteria (Bate 1995). First we use the Courant condition, which basically is the restriction that one

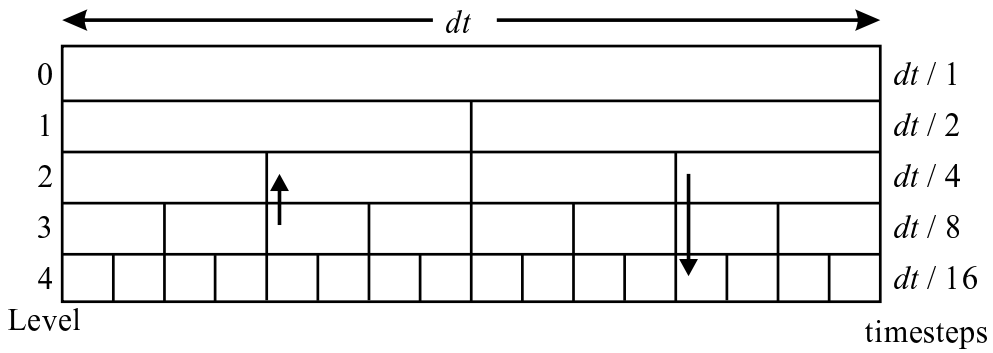

Figure 3.1: *Example for a timestep scheme with the global timestep dt (level $L = 0$) corresponding to an integer 2^4. Here, the highest level $L = 4$ has a time step of $dt/2^4$. Arrows indicate possible shifts of particles from lower to higher levels and vice versa.*

particle must not move further than its smoothing length during one timestep. The full formula is

$$\delta t_{\mathrm{cour}} = \frac{0.3\,h}{a + h\,|\vec{\nabla}\,\vec{v}| + 1.2\,(\alpha\,a + \beta\,h\,|\vec{\nabla}\vec{v}|)}\,, \tag{3.5.78}$$

where α and β are the artificial viscosity parameters discussed above and a the sound speed. The last term in the denominator is only included if $\vec{\nabla}\vec{v} < 0$. The second criterion, similar to the Courant condition, makes sure that a particle does not move further than one smoothing length due to its acceleration $\vec{a}$:

$$\delta t_{\mathrm{acc}} = 0.3\,\sqrt{\frac{h}{|\vec{a}|}}\,. \tag{3.5.79}$$

The minimum of all three criteria is taken as the new particle timestep.

3.5.5 SPH & N–body

For the evolution of a system consisting of a hydrodynamic gas and a collisionless N–body part, we use a code made available by Matthew Bate (Bate, Bonnell & Price 1995).

The SPH particles are treated in the same way as shown in the foregoing sections. The gravitational softening is done as described by Equation (3.5.67). The gravitational interaction between different N–body particles and between N–body and SPH particles is softened using the Plummer softening given in Equation (3.4.37). The timestep for N–body particles is computed via the error (3.5.77) given by the Runge-Kutta-Fehlberg scheme only.

The difference between the second order leapfrog integrator of the pure N–body code and the first order Runge-Kutta-Fehlberg scheme shows up when looking at the simple testcase of a bound system of two stars in circular orbit with relative distance a_0. Figure 3.2 shows, for each of the two codes, the time evolution of the relative error $(a(t) - a_0)/a_0$. Both simulations used exactly the same initial conditions and timesteps. With the leapfrog integrator (left), the distance fluctuates and the maximum deviation is about 10^{-5}. In contrast, the Runge-Kutta-Fehlberg scheme shows severe deviations – at the end of the simulation the error is about 0.7.

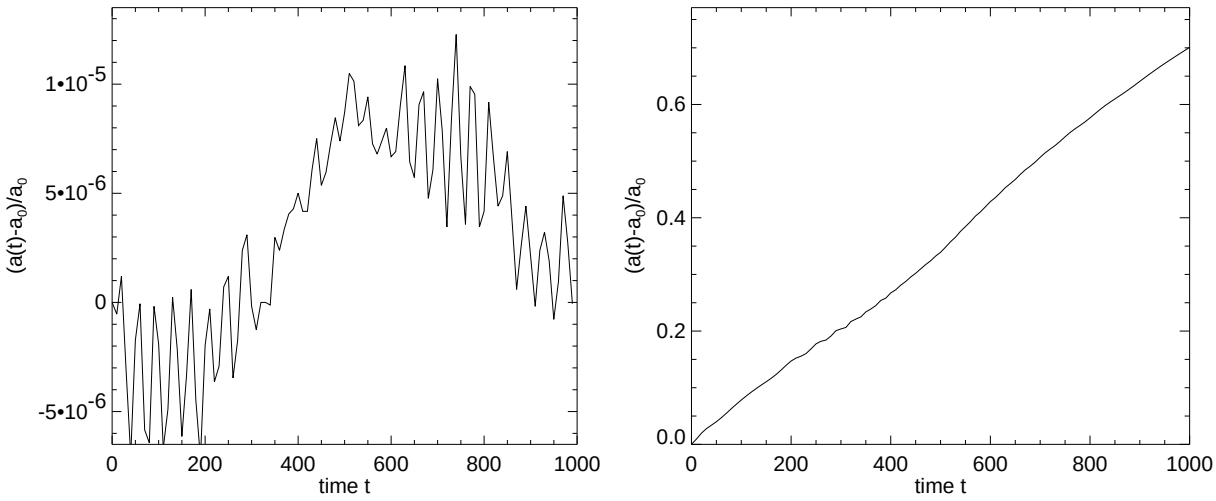

Figure 3.2: *Evolution of the error in distance of two stars in circular orbits. Initially, the stars have a distance* $a_0 = 1.0000$*, equal masses* $m = 1.0000$ *and initial velocities* $v = 0.707107$ *in dimensionless code units. The orbit time is* $t_o = 4.4429$*. Plummer softening is switched off; timestep* $\Delta t = 0.1$*.* ***Left:*** *Leapfrog.* ***Right****: Runge-Kutta-Fehlberg scheme.*

Later simulations with stationary N–body models show that this does not have effects on collisionless simulations using many particles. However, if two-body interactions get important, the first order scheme may induce errors.

Chapter 4

Star Formation, Stellar Feedback and Stability of Young Stellar Clusters

Feedback from stars is probably the most important limiting factor for the star formation efficiency and the formation of bound stellar clusters. During the formation of star clusters gas expulsion, caused by feedback of young massive stars, terminates the star formation epoch and can unbind the stellar system. Many mechanisms leading to gas loss exist, like ionizing radiation, stellar winds or supernova explosions. It is still uncertain which of those play the major role. The gas expulsion reduces the binding energy of the cluster and can lead to a disruption of the system.

After explaining how star formation can be included in SPH simulations, this chapter gives an overview of the possible expulsion mechanisms and estimates the amount of energy fed into the interstellar medium. Next, analytical criteria to get a limit for the star formation efficiency with regard to bound cluster formation are derived. In the last section, an implementation for feedback in SPH simulations is proposed.

4.1 Implementation of Star Formation in SPH

Various ideas for the inclusion of star formation in SPH are discussed in the literature. Bate, Bonnell & Price (1995) use sink particles, which are formed by replacing all particles inside a gravitational unstable and collapsing region of the size of a smoothing length by one N–body particle. Corrections for the gaseous forces at the boundary of the sink are applied. Sinks can also accrete more gas. This method has been successfully applied to the numerical simulation of fragmentation of molecular clouds and star formation (Klessen 1998). However, using sink particles only makes sense where the mass of the individual particles is smaller than the mass of the forming stars. In this case this method allows studying the properties of individual stars that form and may give hints to the initial mass function.

As we deal with molecular clouds with masses of order $10^5\,M_\odot$, the mass of one gas particle in simulations with about 10^5 particles is of the order of one solar mass. We therefore apply the idealized star formation prescription used e.g. in galaxy formation simulations. In those simulations, the mass of a gas particle equals that of a molecular cloud and is thus much larger than the mass of individual stars: If such a region of gas is collapsing, a certain fraction or the whole mass of that SPH particle is converted into one N–body particle. This particle has no further gas properties and represents several stars. Various implementations can be found in

Katz (1992), Gerritsen & Icke (1997), Thacker & Couchman (2000) and Springel (2000). In our case of a $10^5\,M_\odot$ cloud, the SPH particles have masses of order of molecular cloud cores.

In our simulations, the individual N–body particles do not represent individual stars, but are thought to represent the distribution function of the stars in the statistical sense given in Section 3.4.1.

For the idealized star formation mechanism, we need criteria to decide whether an individual or a group of SPH particles forms a star. The main criterion we make use of is the Jeans criterion, which tells whether the region around the SPH particle is gravitational unstable or not. We use the Jeans mass M_J given by Scheffler & Elsässer (1992):

$$M_J = (\frac{\pi\, R_{\rm gas}\, T}{4\, G\, \mu})^{3/2}\, \rho^{-1/2} \tag{4.1.1}$$

or

$$M'_J = (\frac{\pi\, T'}{4\, \gamma})^{3/2}\, \rho'^{-1/2} \tag{4.1.2}$$

in dimensionless code units.

If the density is roughly constant over one smoothing length h, the mass inside the smoothing volume of one SPH particle is $M = 4\,\pi\,h^3\rho/3$. If we assume that stars only form in regions where this mass exceeds the local Jeans mass, $M > M_J$, we get the density criterion

$$\rho > (\frac{3^2\,\pi}{4^5})^{(1/3)}\, \frac{R_{\rm gas}\, T}{h^2\, G\, \mu} \tag{4.1.3}$$

or

$$\rho' > (\frac{3^2\,\pi}{4^5})^{(1/3)}\, \frac{T'}{h'^2\, \gamma}\,. \tag{4.1.4}$$

Another method, used by Nakasato, Mori & Ken'ichi (2000), is to compare the dynamical timescale $t_d = 1/\sqrt{4\,\pi\,G\,\rho}$ with the sound crossing time $t_c = h/a$, where $a^2 = R_{\rm gas}\,T/\mu$ is the isothermal sound speed. If the dynamical time is less than the sound crossing time, $t_d < t_c$, the gas region is considered to collapse:

$$\frac{1}{\sqrt{4\,\pi\,G\,\rho_i}} < \frac{h_i}{a_i} \tag{4.1.5}$$

or

$$\rho_i > \frac{R_{\rm gas}\, T_i}{4\,\pi\, G\, \mu\, h_i^2}\,, \tag{4.1.6}$$

which gives nearly the same result as (4.1.3). Nakasato et al. (2000) give an estimation for the smoothing length $h = \beta\,(m_i/\rho)^{1/3}$, where β is a parameter between 1 and 2. They get

$$\rho_i > (\frac{R_{\rm gas}}{4\,\pi\, G\, \mu})^3\, \frac{T^3}{m_i^2}\, \frac{1}{\beta^6}\,, \tag{4.1.7}$$

so both criteria depend primary on the temperature.

In addition, stars are only allowed to form where the flow is converging, which requires

$$\vec{\nabla}\vec{v} < 0 \tag{4.1.8}$$

for the divergence of the velocity. By this we exclude regions which are Jeans unstable but are actually expanding.

Another criterion to check is that the SPH particle remains in the unstable condition for a time t_u that is longer than the collapse timescale (Gerritsen & Icke 1997)

$$t_u > (4\,\pi\,G\rho)^{-1/2}\,. \tag{4.1.9}$$

To prevent unphysical star formation in Jeans unstable low density regions, one can further assume that star formation is prohibited for densities smaller than a global density $\rho_{\rm global}$.

4.2 Stellar Feedback

Observations of globular clusters and old open clusters show that these system do not contain a significant amount of gas. Consequently, the residual gas, which has been left over from the star formation process, must have been expelled during or shortly after star formation took place. The stars itself can feed an amount of energy into the surrounding interstellar medium that is of the same order as the potential energy of the gas and can thus cause the expulsion of the gas. Three different feedback mechanisms are discussed in the literature: stellar winds, ionizing radiation and supernova explosions.

For a simple estimation on how much energy is needed to expel the residual gas, we consider a spherically symmetric, homogeneous initial gas cloud. To completely expel the residual gas from the cluster, the amount of energy fed into the gas must be comparable or greater than the binding energy of the gas, which in case of a homogeneous density distribution for gas and stars is

$$W_{\rm gas} = 4\,\pi \int_0^R (\frac{1}{2}\,\rho_g\,\phi_g + \rho_g\,\phi_s)\,r^2\,dr = \frac{3\,(\epsilon^2-1)\,G\,M_c^2}{5\,R}, \tag{4.2.10}$$

where ϵ is the star formation efficiency, ρ_g and ϕ_g are the constant density and the gravitational potential of the gas and ϕ_s is the potential of the stars.

For a typical molecular cloud with mass $M_c = 10^5\,{\rm M}_\odot$ and radius $R = 10\,{\rm pc}$, the binding energy of the gas is $W_{\rm gas} \approx (\epsilon^2-1)\,5.2\cdot 10^{49}\,{\rm erg} = (\epsilon^2-1)\,5.2\cdot 10^{42}\,{\rm J}$.

Supernovae release energies of about $10^{51}\,{\rm erg} = 10^{44}{\rm J}$ and therefore are surely sufficient to expel all the gas from the cluster on a short timescale. However, they take place not until the end of the lifetime of massive stars. Earlier processes may be more effective. The energy feedback by the stellar wind for a $15\,M_\odot$ star is about $8.5\cdot 10^{48}\,{\rm erg} = 8.5\cdot 10^{41}\,{\rm J}$ (Abbott 1982). With a lifetime of about $10^7\,{\rm yr}$ we get a rate of about $2.4\cdot 10^{34}{\rm erg/s} = 2.4\cdot 10^{27}{\rm J/s}$.

Can the ionizing radiation of massive OB stars dominate the gas expulsion process ? A typical ionizing star has an initial Strömgren radius $R_{\rm str} = 20\,n^{-2/3}\,{\rm pc\,cm^{-2}} = (1-\epsilon)^{-2/3}\,0.36\,{\rm pc}$ with the column density $n = \rho_g\,N_A/\mu$ of the surrounding gas and $\mu = 2.36\,{\rm g/mol}$ in the case of a molecular cloud. The mass therein is $M_{\rm str} = 4\,\pi/3\,\rho_g\,R_{\rm str}^3 = (1-\epsilon)^{-1}\,4.7\,{\rm M}_\odot$. During the expansion phase (Spitzer 1968), the time dependent mass inside the H II region is (Franco, Shore & Tenorio-Tagle 1994)

$$M_i = M_{\rm str}\,(1 + \frac{7\,a_i\,t}{4\,R_{\rm str}})^{6/7}, \tag{4.2.11}$$

where $a_i = \sqrt{R_{\rm gas}\,T/\mu} = 8.0\,{\rm km/s}$ is the sound speed inside the ionized region with $T = 1.0 \cdot 10^4\,{\rm K}$ and $\mu = 1.3\,{\rm g/mol}$. After $t = 10^7\,{\rm yrs}$, the typical lifetime of an OB star, we have $M_i \approx (1-\epsilon)^{-3/7}\,7.9 \cdot 10^2\,{\rm M}_\odot$. To completely ionize the whole gas cloud, we therefore need $M_g/M_i = (1-\epsilon)^{10/7}\,1.3 \cdot 10^2$ OB stars. This is in good agreement with reasonable initial mass functions. Knödlseder (2000) showed that Cygnus OB2, a probable young globular cluster in the Galactic disk, contains about 120 O stars, while the total mass could be as high as $10^5\,{\rm M}_\odot$. We conclude, that the ionizing radiation from high mass stars is sufficient to expel the residual gas.

We can estimate the rate of energy fed back into the interstellar medium by ionizing radiation looking at the formation phase (Spitzer 1968) of the H II region: If a massive OB star starts ionizing its surroundings, the radius R_I of the ionization front will evolve like

$$R_I = R_{\rm str}\,(1 - e^{-t/t_I})^{1/3}\,, \tag{4.2.12}$$

where $t_I = 1/n_H\,\alpha_B$ is the typical timescale for the formation phase and

$$R_{\rm str} = \left(\frac{3\,S_0}{4\,\pi n_H^2\,\alpha_B}\right)^{1/3} \tag{4.2.13}$$

the Strömgren radius. We define S_0 as the flux of ionizing Lyman–α photons with energies $E_\nu = 13.6\,{\rm eV}$, n_H as the number density of hydrogen atoms and $\alpha_B = 2.6 \cdot 10^{-19}{\rm m}^3/{\rm s}$ as the recombination coefficient. As for temperatures greater than $10^4\,{\rm K}$ cooling becomes efficient, this temperature can be taken as an upper limit. As we deal with cool gas clouds only, the temperature change is of order of $\Delta T = 10^4\,{\rm K}$. The deposit of thermal energy into the interstellar medium during the formation phase is then

$$\Delta E = \frac{\gamma\,R_{\rm gas}}{\mu}\,\Delta T\,M_{\rm str}\,. \tag{4.2.14}$$

Using the mass density $\rho = n_H\,\mu/N_A$, where N_A is the Avogadro constant, and the ionized mass inside the Strömgren sphere $M_{\rm str} = 4\,\pi\,R_{\rm str}^3\,\rho/3$, we get

$$\Delta E = \frac{\gamma\,R_{\rm gas}}{N_A}\,\Delta T\,S_0\,t_I\,. \tag{4.2.15}$$

Comparing this with the energy flux of the ionizing star integrated in time during the formation phase $E_{\nu,{\rm tot}} = S_0\,E_\nu\,t_I$ we get the ratio

$$\frac{\Delta E}{E_{\nu,{\rm tot}}} = \frac{\gamma R_{\rm gas}\Delta T}{N_A\,E_\nu}\,. \tag{4.2.16}$$

Inserting the physical constants and $\Delta T = 10000\,{\rm K}$ we conclude that about 10 % of the ionization energy is deposited in the surrounding medium. With a typical mean flux for OB stars of $S_0 = 10^{48}\,{\rm s}^{-1}$, given by Franco et al. (1994), we get an energy input rate of about $2 \cdot 10^{29}\,{\rm J/s}$ for one typical OB star, which is about 100 times higher than the estimated energy input by the stellar wind.

4.3 Theoretical Limits for Bound Stellar Clusters after Gas Expulsion

We now give two analytical approaches to determine the necessary conditions to obtain bound stellar cluster after the residual gas has been expelled. We only consider gas expulsion timescales that are less than the dynamical timescales of the stellar part.

4.3.1 Radial Expansion due to the Gas Loss

We first present a criterion obtained by Hills (1980). He showed that a system of stars and gas loosing more than half of its mass in less than a dynamical timescale will disrupt:

We consider a virialized, spherically symmetric gas cloud before the onset of star formation. The cloud has the kinetic energy $E_{\rm kin,0} = 1/2\, M_0 \overline{v_0^2}$ and the potential energy $E_{\rm pot,0} = -\alpha G M_0^2/R_c$. Here, M_0 is the mass, $\overline{v_0^2}$ the square of the velocity dispersion due to thermal movement of the molecules and R_0 the radius of the original cloud. The geometric factor α allows the application to different spatial structures, assuming that the gas cloud changes its size homogeneously (Mathieu 1983). Using the virial theorem, $2\,E_{\rm kin,0} + E_{\rm pot,0} = 0$, we get the square of the velocity dispersion

$$\overline{v_0^2} = \alpha\,\frac{GM_0}{R_0}\,. \tag{4.3.17}$$

Next we assume that a certain fraction, the star formation efficiency ϵ, of the gas mass is transformed into stars with the same velocity dispersion. We thus get the mass $M_s = \epsilon M_0$ of the stellar system after the star formation event and the mass $M_g = (1-\epsilon)M_0$ of the residual gas which is driven out of the cluster shortly afterwards by feedback processes of the stars.

If the time that is needed to drive the gas out of the system (gas expulsion timescale) is small compared to the dynamical timescale of the stars, the stars cannot react and will retain their velocities and kinetic energies during the gas expulsion. Consequently, the radius of the stellar system stays constant. The total energy $E = E_{\rm kin} + E_{\rm pot}$ shortly after the gas loss is therefore

$$E = \frac{1}{2}\,M_s\overline{v_0^2} - \alpha\,\frac{GM_s^2}{R_0}\,. \tag{4.3.18}$$

Substituting $\overline{v_0^2}$ by Equation (4.3.17), we get

$$E = \frac{1}{2}\,M_s\alpha\frac{GM_0}{R_0} - \alpha\,\frac{GM_s^2}{R_0}\,. \tag{4.3.19}$$

On a longer timescale, the system will again reach virial equilibrium by adapting its radius to the new value R. The total energy then is $E = E_{\rm pot}/2$ or

$$E = -\,\frac{1}{2}\,\alpha\,\frac{GM_s^2}{R}\,. \tag{4.3.20}$$

By equating the last two expressions (4.3.19) and (4.3.20) we obtain the ratio of the new to the initial radius:

$$\frac{R}{R_0} = \frac{\epsilon}{2\,\epsilon - 1}\,. \tag{4.3.21}$$

Hills (1980) concludes that "if less than half the mass of an interstellar cloud forms into stars before the rest disperses [...], the new stellar system dissociates and forms an expanding association". Thus, to obtain bound stellar clusters, a star formation efficiency $\epsilon > 0.5$ is needed. As the typical star formation efficiencies are less than 10%, the formation of gravitationally bound old open clusters and globular clusters is an interesting and yet unsolved problem.

On the other hand, if the expulsion timescale is much longer than the dynamical time, the cluster will expand adiabatically. In that case $R \cdot M$ is constant and therefore (Hills 1980; Mathieu 1983) the ratio of final to initial radius is

$$\frac{R}{R_0} = \frac{M_0}{M_s} = \frac{1}{\epsilon}\,. \tag{4.3.22}$$

Numerical simulations investigating the stability of young star clusters after gas expulsion have been done by Lada, Margulis & Dearborn (1984). They showed that open star clusters, initially in virial equilibrium with the surrounding residual gas and containing up to 100 stars, can remain bound even if the star formation efficiency is as low as 30%. In their simulations they treated the residual gas as a variable external potential added to that of the stars. Goodwin (1997) extended these simulations to globular clusters, increasing the number of particles, allowing for different gas expulsion mechanisms and including loss of stars due to the galactic tidal field. Klessen & Burkert (2000) and Klessen & Burkert (2001) presented high-resolution simulations of cluster formation in turbulent molecular clouds. Their models lead to bound clusters for very low star formation efficiencies. Additionally, a semi–analytic model by Adams (2000) also claims that the formation of bound star clusters occurs even for global star formation efficiencies much smaller than 50%.

4.3.2 Influence of Different Density Distributions on Stability

Now we look at a more detailed model to obtain a threshold for the star formation efficiency. We assume that the stars after their formation virialize in their own potential and that of the residual gas. We again consider instantaneous gas expulsion only. Is the remaining system of stars still bound after the gas has been ejected ?

We assume different spherical symmetric density distributions $\rho_s = \bar{\rho}_s\, r^{-n_s}$ for the stars and $\rho_0 = \bar{\rho}_0\, r^{-n_g}$ and $\rho_g = \bar{\rho}_g\, r^{-n_g}$ for the gas before and after star formation, respectively. Beyond the cut-off radius R, the densities are set to zero. This describes a globally stable gas cloud with constant radius, that only shows local fragmentation and star formation.

The total masses $M = \int_0^R 4\,\pi\, r^2\, \rho(r)\, dr$ of the original gas cloud, the residual gas and the stars are

$$M_0 = \frac{4\,\pi}{3-n_g}\,\bar{\rho}_0\, R^{3-n_g} \quad , \quad M_g = \frac{4\,\pi}{3-n_g}\,\bar{\rho}_g\, R^{3-n_g} \quad \text{and} \quad M_s = \frac{4\,\pi}{3-n_s}\,\bar{\rho}_s\, R^{3-n_s}\,. \tag{4.3.23}$$

For the convergence of the integration, $n_g, n_s < 3$ is required. If we adopt a global star formation efficiency $\epsilon = M_s/M_0$ we get the relations

$$\frac{\bar{\rho}_s}{\bar{\rho}_0} = \epsilon^* \quad \text{with} \quad \epsilon^* = \frac{3-n_s}{3-n_g}\, R^{n_s-n_g}\, \epsilon \quad \text{and} \quad \frac{\bar{\rho}_g}{\bar{\rho}_0} = 1-\epsilon\,. \tag{4.3.24}$$

The local star formation efficiency, measured at a certain point in the cloud, may vary with radius.

We apply the virial equilibrium condition given by Spitzer (1978) to the stars in our system:

$$2\,E_{\rm kin,0} + E_{\rm sg} = 0 \quad \text{with} \quad E_{\rm sg} = -\int\limits_V d^3r\,\rho_s(r)\,r\,\frac{d\Phi_{\rm sg}}{dr}\,. \tag{4.3.25}$$

Here, $E_{\rm kin}$ is the kinetic energy of the stars and $E_{\rm sg}$ is the potential energy of the stars with respect to the potential $\Phi_{\rm sg}$ caused by the stars itself and the surrounding residual gas.

After gas expulsion, the remaining stellar system will only stay bound, if the total energy

$$E_{\rm tot} = E_{\rm kin} + E_{\rm s} < 0 \quad \text{with} \quad E_{\rm s} = -\int\limits_V d^3r\,\rho_s(r)\,r\,\frac{d\Phi_{\rm s}}{dr}\,, \tag{4.3.26}$$

where $E_{\rm s}$ and $\Phi_{\rm s}$ are the potential energy and the potential of the stars, respectively. If we again consider only fast gas expulsion, the stars will keep their kinetic energies and $E_{\rm kin} = E_{\rm kin,0}$. Now, inserting $E_{\rm kin,0}$ from Equation (4.3.25) leads to the condition

$$E_{\rm s} < \frac{1}{2}\,E_{\rm sg} \tag{4.3.27}$$

for bound stellar clusters (Elmegreen & Efremov 1999).

To derive $E_{\rm s}$ and $E_{\rm sg}$, we directly apply the definitions in (4.3.25) and (4.3.26). However, the term including only the stellar potential can also be written as the usual potential energy term

$$E_{\rm s} = \frac{1}{2}\int\limits_V d^3r\,\rho_s(r)\,\Phi_{\rm s}(r)\,, \tag{4.3.28}$$

which can be evaluated more straight forward. The gravitational potentials inside and outside a sphere are given by

$$\Phi\,(r) = -\,4\,\pi\,G\,\left(\frac{1}{r}\int\limits_0^r \rho\left(r'\right)\,r'^{\,2}\,dr' + \int\limits_r^\infty \rho\left(r'\right)\,r'\,dr'\right)\,. \tag{4.3.29}$$

The first term of the potential (4.3.29) comes from the sphere inside the radius r replaced by a point mass, the second term is the constant potential in the center of a shell integrated from r to infinity. To obtain $\Phi_{\rm s}$, we have to replace $\rho = \rho_s$ in above equation. To obtain $\Phi_{\rm sg}$, we have to insert the sum $\rho = \rho_s + \rho_g$.

Carrying out the integrations in eqs. (4.3.28), (4.3.25) and (4.3.29) using the given density distributions, which are zero for $r > R$, the criterion (4.3.27) leads to

$$\epsilon > \frac{5 - 2n_s}{10 - 3n_s - n_g}\,. \tag{4.3.30}$$

The results are visualized in Figure 4.1. In the special case, where the stars and the gas follow the same density distribution, $n_s = n_g$, we get a local star formation efficiency that is constant over the entire radius. The criterion then simplifies to $\epsilon > 1/2$, which is equal to the result obtained by Hills (1980) as shown in section 4.3.1.

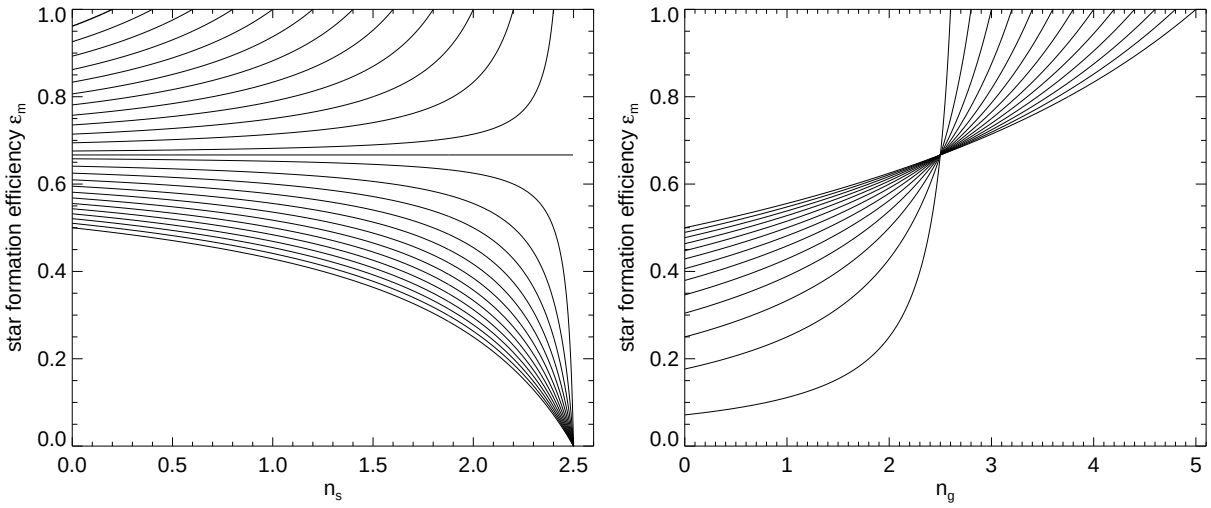

Figure 4.1: *The minimum star formation efficiency ϵ_m that is needed to get a bound star cluster.* ***Left:*** *ϵ_m with respect to the index n_s of the star cluster. The different lines correspond, from bottom to top, to different indices $n_g = 0, 0.2, 0.4, \ldots, 5.0$ of the gas cloud.* ***Right****: ϵ_m with respect to the index n_g of the residual gas. The different lines correspond, again from bottom to top, to different indices $n_s = 0, 0.2, 0.4, \ldots, 2.5$ of the stellar part. We emphasize that $n_g \geq 3$ leads to infinite masses (corresponding to curves above the straight line in the left diagram)*

In the more general case, the more concentrated the stars are with respect to the gas, the lower is the critical star formation efficiency that allows the formation of bound clusters. This expresses the fact that under this conditions the local star formation efficiency in the center of the cloud is higher than the global one.

As the typical Galactic star formation efficiencies are less than 10 %, different approaches were made to explain bound cluster formation in clouds with low star formation efficiencies. One way out may be a collapse of the star cluster before the gas is completely expelled, leading to a higher "effective" star formation efficiency. Lada et al. (1984) and Verschueren (1990) proposed a low or zero initial velocity dispersion to explain the collapse. This would decrease the kinetic energy in (4.3.26) and allow a greater change in the potential energy. Saiyadpour, Deiss & Kegel (1997) considered the effect of dynamical friction on the stellar cluster to reduce the stellar velocities.

4.4 Implementation of Stellar Feedback in SPH

Stellar feedback by high mass stars causes the self regulation of the star formation process. Thacker & Couchman (2000) examine various methods of implementing supernova feedback in simulations of galaxy formation. They either distribute the feedback energy as thermal energy over the SPH smoothing length or deposit it into one single particle. Nakasato, Mori & Ken'ichi (2000) take into account energy feedback by supernova and stellar winds. Assuming that thermalisation is fast enough, they distribute the energy as thermal energy smoothly over the nearest neighbours. They also consider mass ejection. However, most destructive is the ionizing radiation – once the interstellar medium is ionized, star formation will be terminated

immediately.

Nearest Neigbour Heating

In our simulations we include feedback by massive stars by heating up the gas around each N–body particle that has formed. We now estimate the amount of energy one N–body particle feeds back into the medium, which is proportional to the relative amount of massive stars contained in the particle. This energy is then smoothly distributed to the nearest gas particles, using the SPH kernel, at every timestep of the N–body particle.

To get an idea on the initial number of OB stars in a star cluster we assume a Salpeter (1955) initial mass function (IMF) $f(m)$ which gives the number of stars inside the mass interval $[m \dots m + dm]$:

$$f(m)\, dm = k\, m^{-\alpha}\, dm\,. \tag{4.4.31}$$

The parameter α gives the slope of the IMF. Given the total mass M of the stellar system, the normalization constant k is fixed by evaluation of the integral $\int m\, f(m)\, dm$ from the lowest allowed mass $m_{\min}$ to the highest allowed mass $m_{\max}$:

$$k = \frac{(2-\alpha)\, M}{m_{\max}^{2-\alpha} - m_{\min}^{2-\alpha}}\,. \tag{4.4.32}$$

The total number of stars is

$$N = \int_{m_{\min}}^{m_{\max}} f(m)\, dm = \frac{2-\alpha}{1-\alpha}\, M\, \frac{m_{\max}^{1-\alpha} - m_{\min}^{1-\alpha}}{m_{\max}^{2-\alpha} - m_{\min}^{2-\alpha}}\,. \tag{4.4.33}$$

The cases $\alpha = 1$ and $\alpha = 2$ must be treated separately.

Thus, the total number N_{OB} of OB stars with masses greater than m_{OB} is

$$N_{\mathrm{OB}} = \int_{m_{\mathrm{OB}}}^{m_{\max}} f(m)\, dm \tag{4.4.34}$$

and the number of OB stars per stellar mass is

$$\kappa = \frac{2-\alpha}{1-\alpha}\, \frac{m_{\max}^{1-\alpha} - m_{\mathrm{OB}}^{1-\alpha}}{m_{\max}^{2-\alpha} - m_{\min}^{2-\alpha}}\,. \tag{4.4.35}$$

For typical parameters $m_{\min} = 0.1\, M_\odot$, $m_{\max} = 100\, M_\odot$, $m_{\mathrm{OB}} = 10\, M_\odot$ and $\alpha = 2.35$ we have $\kappa = 0.0054/M_\odot$

If we assume a mean energy rate $\bar{\eta}$ which is fed into the interstellar medium by one typical high mass star, with the above definition of the number of OB stars per mass, the energy rate per mass is $\kappa\, \bar{\eta}$. Additionally, if we assume that every single N–body particle feeds back energy to its surroundings according to its mass and the ratio of OB stars κ, we get the energy feedback from one N–body particle with mass m_i evolved one timestep Δt as $\Delta E = \kappa\, \bar{\eta}\, m_i\, \Delta t$.

For example, stellar wind energy rates of $\bar{\eta} = 2.4 \cdot 10^{27}\mathrm{J/s}$ lead to

$$\Delta E = 6.4 \cdot 10^{-6}\,\mathrm{J/(s\,kg)}\, m_i\, \Delta t\,, \tag{4.4.36}$$

and ionizing energy rates of $\bar{\eta} = 2 \cdot 10^{29}\mathrm{J/s}$ to

$$\Delta E = 5 \cdot 10^{-4}\,\mathrm{J/(s\,kg)}\, m_i\, \Delta t\,. \tag{4.4.37}$$

In code units, for a simulation with units $\hat{R} = 50\,\mathrm{pc}$ and $\hat{M} = 10^5\,M_\odot$ we have (Table 3.1) $\Delta E' = 3.9 \cdot 10^2\, m_i'\, \Delta t'$ for winds and $\Delta E' = 3 \cdot 10^4\, m_i'\, \Delta t'$ for ionization, respectively.

In our simulations, we have the additional freedom to choose when we turn on the heating from a N–body particle after its formation. This delay time t_{delay} may have severe influence on the star formation efficiency and the boundness of the cluster.

Chapter 5

Numerical Simulation of Gas Expulsion from Star Forming Regions

In this chapter we present simulations of gas expulsion from star forming regions. As shown in Chapter 4, the loss of the residual gas can unbind the embedded stellar system and thus determines the fate of the young cluster.

Our simulations start after the cluster has formed with a given star formation efficiency, but before the residual gas has been expelled. The dynamical timescale of a typical globular cluster with mass $10^5\,M_\odot$ and radius 10 pc is $t_d \approx 1.5 \cdot 10^6$ yr. Assuming that the cluster contains about $N \approx 10^5$ stars, we get the relaxation time of $t_r \approx 1.6 \cdot 10^9$ yr (Equation (3.2.25)). As we restrict our simulations to the early evolution of young clusters, relaxation effects can be neglected and we can represent the stellar system by collisionless, equal mass N–body particles.

In the first section, the effect of the ejection of the residual gas on the stellar system is treated as a time variable external potential, similar to the approach of Lada, Margulis & Dearborn (1984). Varying the assumed star formation efficiency and the timescale of gas expulsion shows their effect on the boundness and the evolution of the density distribution of the young star cluster.

To describe the physics more properly, we replaced the simple description of the residual gas using an external potential by extending our simulations using SPH to follow the hydrodynamic evolution of the gas.

Parts of this Chapter have already been published (Geyer & Burkert 2001).

5.1 Gas Expulsion in Pure N–body Simulations

In the following, all quantities are given in dimensionless code units (see Section 3.3). Thus, taking typical globular cluster properties $\hat{M} = 10^5\,\mathrm{M}_\odot$ and $\hat{R} = 10$ pc as mass and length units, respectively, we obtain a time unit $\hat{t} = (G\,\hat{\rho})^{-1/2} = 1.5 \cdot 10^6$ yr with the density unit $\hat{\rho} = \hat{M}/\hat{R}^3$.

5.1.1 Initial Configuration and the Gas Expulsion Phase

As mentioned in the overview given in Section 2.1, globular clusters can be well described by King (1966) distribution functions

$$f(\mathcal{E}) = \begin{cases} \rho_1 \, (2\,\pi\,\sigma^2)^{-3/2} \, (e^{\mathcal{E}/\sigma^2} - 1) & \mathcal{E} > 0 \\ 0 & \mathcal{E} \leq 0 \end{cases} . \tag{5.1.1}$$

As they only depend on an integral of motion, the energy, this is an isotropic equilibrium solution of the collisionless Boltzmann equation as described in Section 3.2. The notation suggested by Binney & Tremaine (1987) uses the relative potential and energy

$$\Psi = -\Phi + \Phi_0 \quad \text{and} \quad \mathcal{E} = -E + \Phi_0 = \Psi - \frac{1}{2}\,v^2 \,, \tag{5.1.2}$$

where σ is the velocity-dispersion parameter and the constant Φ_0 is chosen such that the distribution function vanishes for $\mathcal{E} \leq 0$. Here Φ is the gravitational potential and E the total energy per mass. King models can be parameterized by either the dimensionless quantity $W_0 = \Psi(0)/\sigma^2$ or the concentration $c = \log_{10}(r_t/r_0)$, using the King radius $r_0 = (9\sigma^2/4\,\pi\,G\,\rho(0))^{1/2}$.

The radial density $\rho(r)$ and the potential $\Psi(r)$ can be computed by numerical integration of the Poisson equation $\triangle\Psi = -\,4\,\pi\,G\,\rho(\Psi)$ or, using the dimensionless radius $R = r/r_0$ and dimensionless potential $W = \Psi/\sigma^2$,

$$\frac{d}{dR}\,(R^2\,\frac{dW}{dR}) = -\,9\,R^2\,\frac{\rho(W)}{\rho_0} \,. \tag{5.1.3}$$

The density is obtained by integrating the distribution function over the velocity space:

$$\rho(W) = \rho_1\,(e^W\,\mathrm{erf}\,(\sqrt{W}) - \sqrt{\frac{4\,W}{\pi}}\,(1 + \frac{2}{3}\,W)) \,. \tag{5.1.4}$$

The main advantage of a King model is its finite radius: Outside the tidal radius r_t the density vanishes. The tidal radius grows rapidly with increasing W_0. In the limit $W_0 \to \infty$, the King distribution equals the isothermal sphere.

To obtain a stable initial configuration of stars and gas, in a first step the stars are distributed according to a King distribution function with total mass equal to that of the initial gas cloud. The potential is tabulated and is used for modelling the external gas potential during the simulation. Therefore, stars and gas have equal density distributions. Finally, the mass of the stars and the gas are scaled according to the given star formation efficiency. Now the stars are in virial equilibrium within the sum of their own potential and the potential of the gaseous component. The parameters of the different models are given in Table 5.1. The dynamical timescales were obtained as described in Section 3.2 with $t_d = \sqrt{1/(G\,\bar{\rho})}$. For each model, the star formation efficiency is varied between 0.15 and 0.80.

To test whether the initial system is in virial equilibrium, several calculations without gas expulsion are performed. The density distributions are well conserved.

For analysing the data, we use the following method to define the cluster center: We calculate the center of mass for all particles inside a sphere with given boundary radius. The center of mass of that sphere is shifted to the center of the coordinate system. Then the boundary radius is increased and the scheme is repeated until the center of mass lies within the desired error limit. Velocities are shifted to the frame of rest of the clusters.

Table 5.1: *Parameters of the Initial Configurations (N–body)*

model	W_0	t_d	R_t	$R_{1/2}$	N	δ
N1	3.0	0.57	1.26	0.34	1000	0.1
N2	5.1	0.34	1.33	0.24	1000	0.1
N3	3.0	0.57	1.26	0.34	4000	0.05

$W_0 = \psi(0)/\sigma^2$: scaled central potential of the King profile; t_d: dynamical timescale at half-mass radius; R_t: tidal radius of King profile; $R_{1/2}$: half–mass radius; N: number of particles used in simulation; δ: numerical (Plummer) smoothing length; total mass (stars and gas) of all models was set to 1; all quantities are given in dimensionless code units (see text).

We simulate the gas expulsion starting at time $t = t_0$ by multiplying the external potential by a time dependent factor

$$\xi = \begin{cases} 1 & t < t_0 \\ 1 - (t - t_0)/t_{\rm exp} & \text{if} \quad t_0 < t < t_0 + t_{\rm exp} \\ 0 & t > t_0 + t_{\rm exp} \end{cases} , \tag{5.1.5}$$

where $t_{\rm exp}$ is the time that is needed to drive the gas out of the system (gas expulsion time).

We can estimate the order of the gas expulsion time: The isothermal sound speed of a molecular cloud gas with temperature $T = 10\,\mathrm{K}$ and molecular weight $\mu = 2.36\,\mathrm{g/mol}$ is $a = \sqrt{R_{\rm gas}\,T/\mu} = 0.19\,\mathrm{km\ s^{-1}}$, where $R_{\rm gas}$ is the gas constant. If we consider a disruptive process that starts at the centre of a cloud as given by model N1 and travels outwards with sound speed, it will need approximately a time of $t_{\rm exp} = R_t\,a^{-1} \approx 6.6\,10^6\,\mathrm{yr}$ (or $t_{\rm exp} \approx 4$, given the dimensionless code units above) to reach the edge of the cloud. Fast processes (e.g. supernova explosions) may remove the gas on shorter timescales. The gas expulsion time will therefore presumably be of the order of a dynamical time which is equal to the unit of time. In the simulations we use $t_{\rm exp} = 0, 2, 4$ and 10, which are equal to $0, 3.5, 7.0$ and 18 dynamical timescales at half-mass radius of model N1 and N3 and $0, 5.9, 12$ and 29 dynamical timescales of model N2.

5.1.2 Dynamics of the Cluster During and After Gas Expulsion

The typical evolution of the N–body part of a cluster with $t_{\rm exp} = 2$ (3.5 dynamical timescales) is displayed in Figure 5.1. Starting at $t = 20$ the external potential is slowly reduced to zero as described in the previous section. The cluster expands. A certain amount of stars gets unbound and starts leaving the system. The bound ones relax after the gas has been completely removed, forming a broader configuration. A particle is supposed to be unbound if its total energy (kinetic energy plus potential energy) is positive. This criterion is different from the one used in similar simulations by Goodwin (1997), who marked all stars outside a given tidal radius as unbound.

Figure 5.2 shows the evolution of the Lagrangian radii containing 10%, 50% and 70% of the *current bound* mass of the system and the virial ratio $\eta = -2\,E_{\rm kin}/E_{\rm pot}$ of the bound particles. The constant mass radii and virial ratios before gas expulsion show that initially the system is indeed in virial equilibrium. When the superimposed gas potential decreases ($t > 20$), the mass radii increase rapidly and relax for $t > t_{\rm exp}$. This behaviour is also reflected in the virial ratio: The decreasing absolute value of the potential increases the virial ratio and causes expansion of

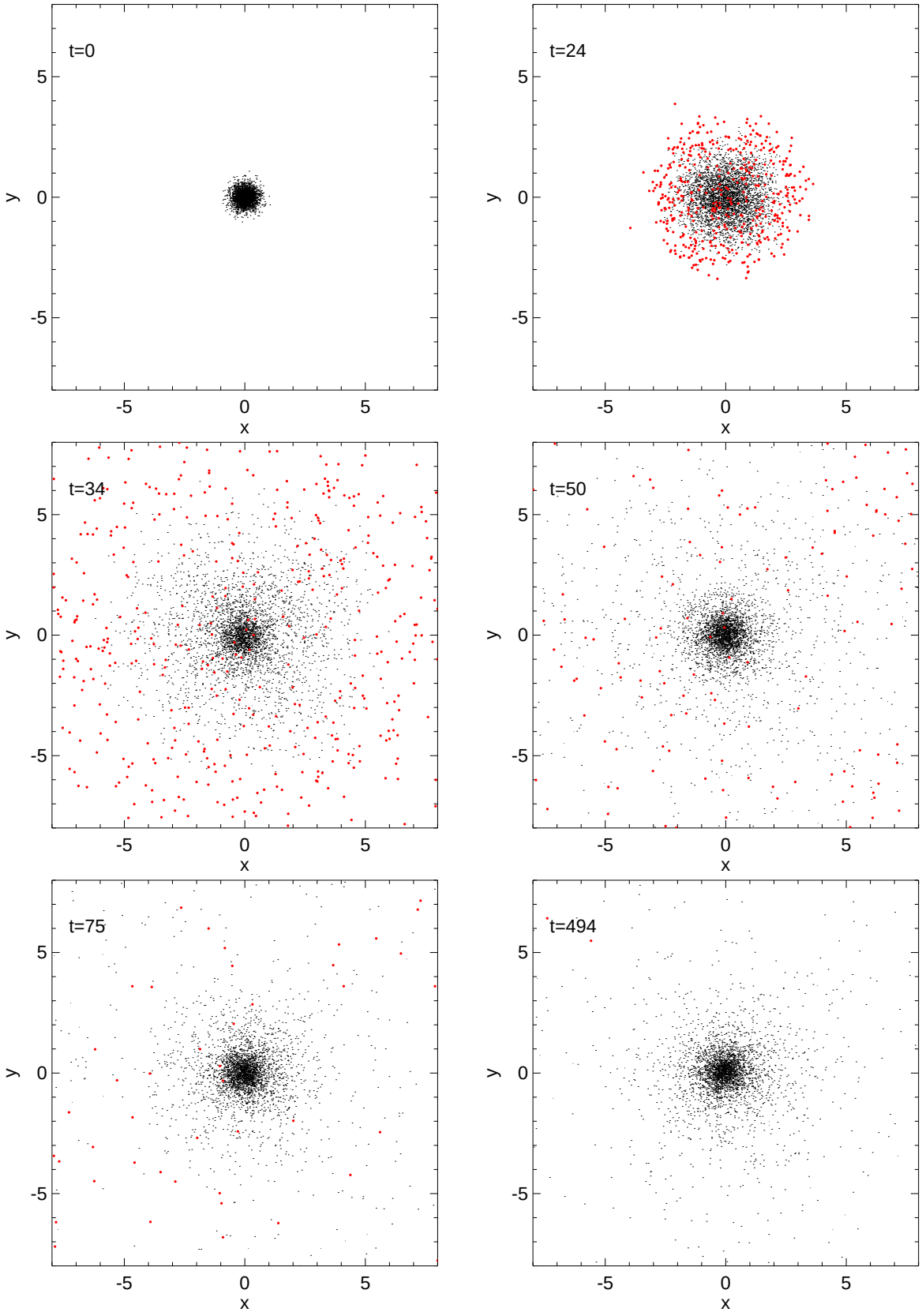

Figure 5.1: *Time evolution of model N3. The time t is given in dimensionless units. The star formation efficiency is $\epsilon = 0.4$, expulsion time $t_{\rm exp} = 2$. The plots show the N–body particles projected onto the x–y–plane; unbound particles are marked red. Gas expulsion starts at time $t = 20$.*

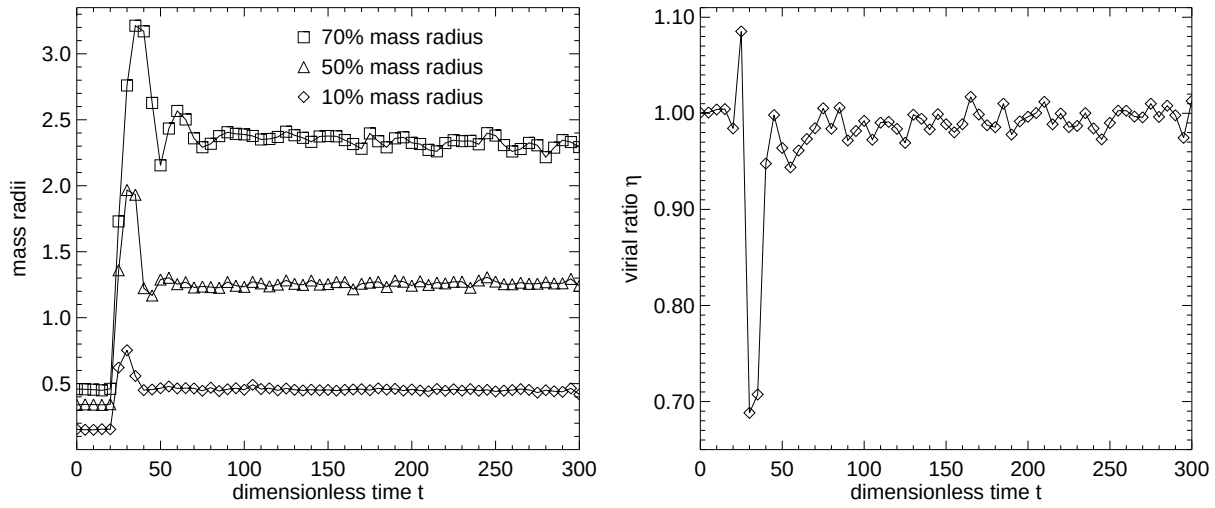

Figure 5.2: *Time evolution of the mass radii (left panel) and the virial ratio η (right panel) of the system shown in Figure 5.1.*

the system. By that expansion, the potential increases again and counteracts the actual motion – the stellar system contracts again. Examining the 70% mass radius, several oscillation can be observed. At the end, the system achieves a more extended equilibrium state, with a virial ratio that deviates less than 3% from the equilibrium case $\eta = 1.0$.

The radial expansion factor of the cluster can be estimated in the adiabatic case (expulsion timescale is much longer than the dynamical time), where $R \cdot M$ is constant, by Equation (4.3.22). This gives the ratio of final to initial radius

$$\frac{R_f}{R_i} = \frac{M_c}{M_s} = \frac{1}{\epsilon} \quad \text{with} \quad 0 < \epsilon \leq 1\,. \tag{5.1.6}$$

On the other hand, if the expulsion time is short compared to the dynamical time, we can apply conservation of kinetic energy per particle during the ejection of the gas which leads to Equation (4.3.21):

$$\frac{R_f}{R_i} = \frac{\epsilon}{2\,\epsilon - 1} \quad \text{with} \quad \frac{1}{2} < \epsilon \leq 1. \tag{5.1.7}$$

If $\epsilon \leq 0.5$ the final system is unbound.

Figure 5.3 shows the ratio of the final to the initial half-mass radii of the *bound* particles at the end of the simulations N3 and N2, compared to the theoretical predictions of Equation 5.1.6 and 5.1.7. If stars are lost and the bound mass of the cluster is not conserved, Equation 5.1.6 and 5.1.7 are not strictly valid any more and discrepancies to the analytic approximations occur.

As expected, the simulations with long gas expulsion timescales fit well the solid curve, representing the adiabatic case. The faster the gas expulsion, the larger is the ratio of the final to the initial radius compared to the theoretical result.

The models with fast gas expulsion follow the dashed curve well for high star formation efficiencies. For low star formation efficiencies, the ratio of final to initial radii is smaller than the analytical prediction, which emphasizes that the divergence for $\epsilon = 0.5$ does not occur in numeric simulations: The final radius is decreased by excluding the unbound particles which are

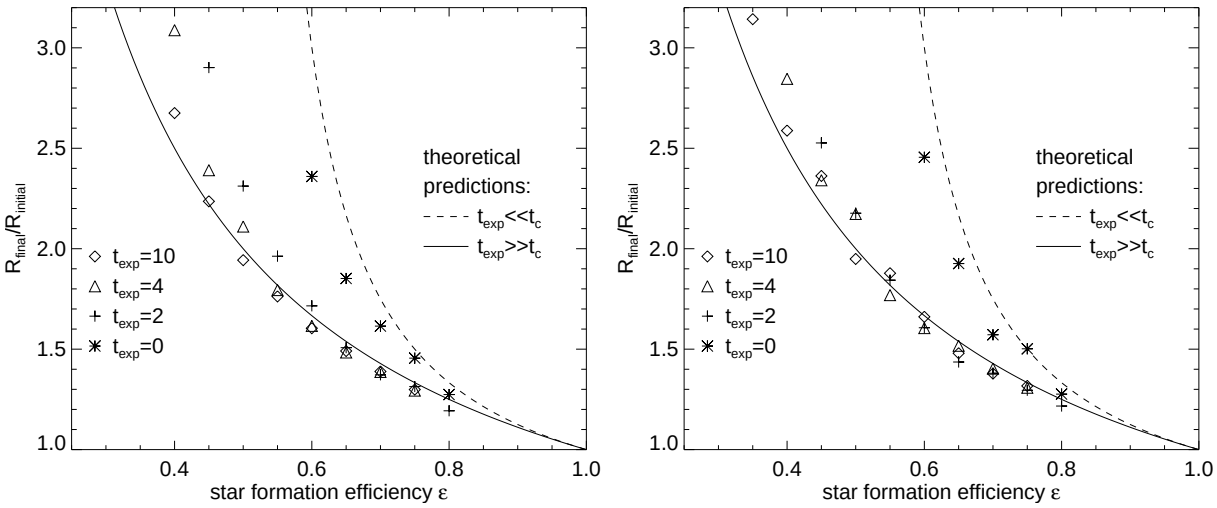

Figure 5.3: *Ratio of the final to the initial half–mass radii versus star formation efficiency of the simulations (left: model N3; right: model N2) for various expulsion timescales* $t_{\rm exp}$.

located preferentially at high radii. Additional, the outgoing particles reduce the total energy of the remaining system and leave behind a tighter bound core.

Ashman & Zepf (2001) stress that for understanding the globular cluster formation process, one needs to explain that giant molecular clouds follow a tight mass–radius relation, whereas globular clusters show no correlation between radius and mass. They propose that a star formation efficiency, that varies from cloud to cloud, causes the different final radii of the formed star clusters.

5.1.3 Constraints on the Star Formation Efficiency

After the gas expulsion the system of the remaining bodies relaxes again (Figure 5.2). Figure 5.4 shows the ratio of the number of finally bound stars to the initial number of stars for various star formation efficiencies and gas expulsion timescales. The upper panel provides a resolution study of the runs N1 and N3 with 1000 and 4000 particles, respectively. Within the uncertainties they are indistinguishable. Large dots show results from Lada et al. (1984) obtained from simulations with 50 (!) stars. As can be seen, the number of particles used does not influence the results, at least in the instantaneous gas expulsion case. This proves that the early results obtained by Lada et al. (1984) for open clusters also hold for globular clusters. For finite gas expulsion timescales we use the dynamical timescale t_d as a basis for comparison: Our curves with $t_{\rm exp} = 3.5$, 7.0 and $18\,t_d$ overlap with the points obtained by Lada et al. (1984) for $t_{\rm exp} = 3$ and $4\,t_d$.

The right panel compares the initially more concentrated King model (N2) to the less concentrated one (N1). We find that the curves of model N2 with $t_{\rm exp} > 0$ are shifted to lower star formation efficiencies or higher ratios of bound stars, respectively. This is due to the lower half-mass dynamical time of the more concentrated cluster N2 (Table 5.1), confirming that only the ratio of the expulsion timescale to the dynamical timescale is important. Thus, more concentrated clusters have a larger chance to survive. In the case of instantaneous gas expulsion ($t_{\rm exp} = 0$) the models N1 and N2 yield the same curve.

The ratio of bound to unbound stars gives a threshold for the star formation efficiency ϵ

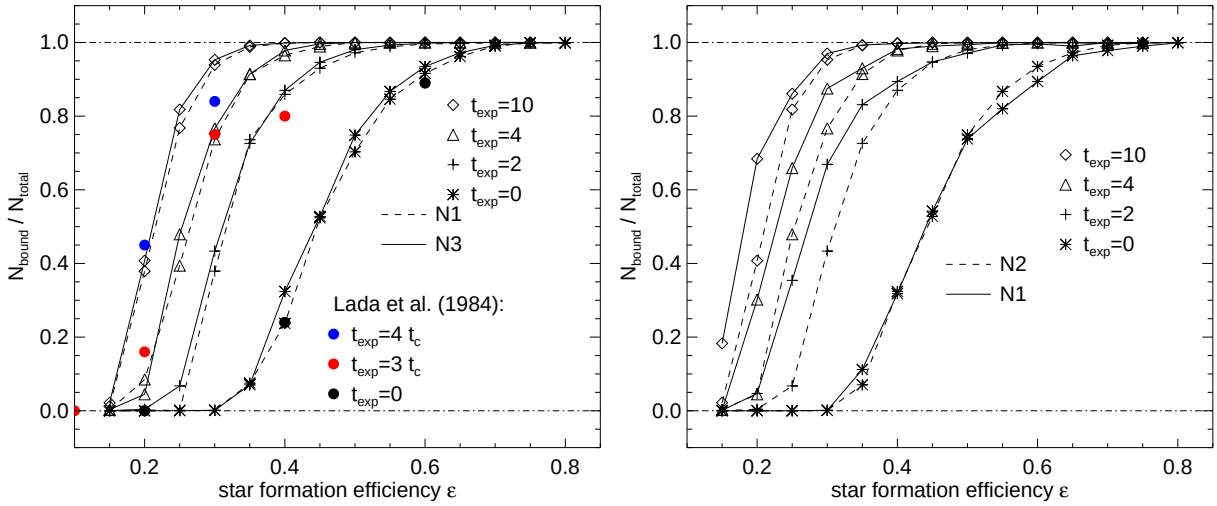

Figure 5.4: *Ratio of the number of bound stars to the initial number of stars in the relaxed system after gas expulsion.* ***Left:*** *models N1 and N3;* ***Right:*** *models N1 and N2; each symbol represents one run with given star formation efficiency and gas expulsion time; large dots are results taken from Lada et al. (1984), Figure 2 therein.*

necessary to form bound clusters. In case of instantaneous gas expulsion (see Figure 5.4) the curves are centered around $\epsilon = 0.45$, which is somewhat less than the theoretical limit $\epsilon = 0.5$ for bound clusters given by Hills (1980).

Adams (2000) recently gave analytic approximations for the dependency of the number of bound stars on the star formation efficiency in the case of instantaneous gas expulsion. For a star formation efficiency $\epsilon = 0.5$ about 73% of the stars are kept, in good agreement to our results from Figure 5.4 ($t_{\rm exp} = 0$). However, our results show a stronger dependence of mass loss on the star formation efficiency ϵ. Contrary to Adams (2000), star clusters with a star formation efficiency lower than $\epsilon = 0.4$ are dissolved in our simulations. This discrepancy can be understood from the fact that Adams uses density distributions of gas and stars with very different concentrations. Thus, even if the global star formation efficiency is small, the local star formation efficiency in the region of star formation could be as high as 90%, leading to a bound system.

Besides these results in the instantaneous gas expulsion case, our simulations show that the number of finally bound stars increases with the gas expulsion time. In order for more than 50% of all the stars to remain bound the star formation efficiency must be equal to 45%, 30%, 25% and 20% for gas expulsion times $t_{\rm exp}$ =0, 2, 4 and 10, respectively. The Galactic average star formation efficiency in giant molecular clouds is of the order of a few percent (Myers et al. 1986, Williams & McKee 1997). Koo (1999) has observed star formation efficiencies up to 15% in the star forming-region W51B, maybe due to shock-interaction with a spiral density wave. Given these star formation efficiencies, unrealistic high gas expulsion timescales are required to obtain bound clusters. Only few clouds show star formation efficiencies up to 30% or 40% (Lada 1992) and may stay bound.

Kroupa, Aarseth & Hurley (2001) showed that in simulations, which include collisions between particles, one third of all stars of the initial cluster remains bound in case of a global star formation efficiency of 30%. The gas is removed on a timescale of order of the dynamical

timescale. They argue that two-body encounters in the radial outwards flow scatter back particles. By that, kinetic energy is redistributed from radial outflow into orbital motions. This process might enhance the number of final bound particles compared to our simulations.

5.2 Combined N–body and Hydrodynamical Simulations

In Section 5.1, the effect of gas removal is treated as a time variable external potential. To describe the physics more properly, we extend our simulations using smoothed particle hydrodynamics as described in Section 3.5.

The conversion from code units to physical units is the same as in Section 5.1.1. Additionally, we describe the internal energy of the gas with the dimensionless temperature that scales with $\hat{T} = G\,\hat{M}\,\mu/(\hat{L}\,R_{\rm gas}\,\bar{\gamma})$ as given in Table 3.1. For an ideal gas with $\bar{\gamma} = 3/2$ and $\mu = 1.0\,\mathrm{g/mol}$, we have $\hat{T} = 3.5\,10^3\,\mathrm{K}$.

5.2.1 Initial Configuration and Models for Gas Expulsion

Murray & Lin (1992) proposed as initial conditions pressure-confined protocluster clouds. Indeed Ashman & Zepf (2001) argue that high pressure environments like starburst galaxies or mergers of galaxies would produce more compressed giant molecular clouds which could lead to globular cluster formation.

As a reasonable initial configuration we therefore adopt a pressure-confined, isothermal Bonnor–Ebert sphere (Ebert 1955; Bonnor 1956).

Assuming spherical symmetry and equilibrium, we can derive the differential equation for the static pressure distribution using the three dimensional equation of motion (3.1.21) and the Poisson equation (3.1.23):

$$\frac{1}{r^2}\,\frac{\partial}{\partial r}\,\frac{r^2}{\rho}\,\frac{\partial p}{\partial r} = -\,4\,\pi\,G\,\rho\,. \tag{5.2.8}$$

Using the ideal equation of state $p = R\,T/\mu\,\rho$ we obtain

$$\frac{1}{r^2}\,\frac{\partial}{\partial r}\,\frac{r^2}{\rho}\,\frac{\partial \rho}{\partial r} = -\,\frac{4\pi G\,\mu\,\rho}{R_{\rm gas}\,T}\,. \tag{5.2.9}$$

With the transformations (Bonnor 1956)

$$\rho = \rho_c\,\exp(-\psi) \quad \text{and} \quad r = \sqrt{\frac{\beta}{\rho_c}}\,\xi \quad \text{with} \quad \beta = \frac{R\,T}{4\pi\,\mu\,G} \tag{5.2.10}$$

we get the *Isothermal Lane-Emden-Equation*

$$\frac{1}{\xi^2}\,\frac{\partial}{\partial \xi}\,\xi^2\,\frac{\partial \psi}{\partial \xi} = \exp(-\psi)\,. \tag{5.2.11}$$

The first boundary condition is the central density $\rho(0) = \rho_c$. The vanishing gravitational forces in the center of a spherical symmetric sphere lead to $d\rho/dr = 0$ at the center $r = 0$. Using the above variables, this reads $\psi = 0$ and $d\psi/d\xi = 0$ at $\xi = 0$. Equation (5.2.11) can only be solved

numerically. However, Bonnor (1956) showed that the solutions are stable to radial density perturbations as long as the cut-off radius of the sphere $r_{\max} < r_c$, where r_c is determined by $\xi_{\max} < \xi_c$ with $\xi_c \simeq 6.451$.

To get a SPH realization of a Bonnor–Ebert sphere we compress a homogeneous sphere, such that its mass M and radius $R = r_{\max}$ are conserved. Each particle with radius r_h in the homogeneous sphere will be assigned a new radius r_b in the Bonnor–Ebert sphere. The total masses m_h and m_b inside the spheres given by these two radii must be equal. We have

$$m_h(r_h) = \int_0^{r_h} dr'_h \, 4\,\pi\, r'^2_h \, \rho_h = \frac{4}{3}\,\pi\, r_h^3\, \rho_h \tag{5.2.12}$$

and

$$m_b(r_b) = \int_0^{r_b} dr'_b \, 4\,\pi\, r'^2_b \, \rho_b(r'_b) = 4\pi \sqrt{\frac{\beta^3}{\rho_c}} \int_0^{\xi_b} d\xi\, \xi^2 \, \exp(-\psi(\xi))\,, \tag{5.2.13}$$

where $\xi_b = \sqrt{\frac{\rho_c}{\beta}}\, R$ and $\rho_b = \rho_c \exp(-\psi(\xi))$. Equating the total masses of the homogeneous sphere and the Bonnor–Ebert sphere, $m_h(R) = m_b(R)$ we obtain

$$\frac{R^3\, \rho_H\, \sqrt{\rho_c}}{3\,\beta^{3/2}} = \int_0^{\xi_{\max}} d\xi\, \xi^2 \, \exp(-\psi(\xi))\,. \tag{5.2.14}$$

We get the central density and the parameter β of the configuration with given $\xi_{\max}$ using $r_{\max} = R = \sqrt{\frac{\beta}{\rho_c}}\, \xi_{\max}$:

$$\rho_c = \frac{\rho_H\, \xi_{\max}^3}{3 \int\limits_0^{\xi_{\max}} d\xi\, \xi^2 \, \exp(-\psi(\xi))} \quad \text{and} \quad \beta = \frac{R^2}{\xi_{\max}^2}\, \rho_c\,. \tag{5.2.15}$$

Thus, fixing $\xi_{\max}$, M and R determines ρ_c and β which essentially gives the temperature T of the sphere.

In general, equating the masses inside the particle radius r_h, $m_h(r_h) = m_b(r_b)$ we obtain

$$\int_0^{\xi_B} d\xi\, \xi^2 \, \exp(-\psi(\xi)) = \frac{r_h^3}{R^3} \int_0^{\xi_{\max}} d\xi\, \xi^2 \, \exp(-\psi(\xi))\,. \tag{5.2.16}$$

So for each particle with radius r_h we can, by numerical integration, compute the corresponding ξ_b and r_b and build up the desired Bonnor–Ebert sphere.

Stars and star clusters form in molecular clouds with temperatures of order 10 K, and are stabilized by a turbulent velocity field. In this first approach we neglect turbulence. In order to prevent global collapse we then have to increase the temperature to its virial value $T = 2.7\,10^3$ K. This implies an energy $E_t = \bar{\gamma}\, M_c\, R_{\rm gas}\, T/\mu$, corresponding to a turbulent velocity field with $v_{\rm tur} = \sqrt{2\, E_t/M_c} = 8.1$ km/s. The initial configuration of the Bonnor–Ebert sphere is given

Table 5.2: *Parameters of the Initial Configurations Including Gas Dynamics (N–body & SPH)*

model	r_h	t_d	N	T	δ	R	ξ_b
S1	0.7	0.8	2×4000	0.76	0.01	1.0	4.0
S2	0.7	0.8	2×11045	0.76	0.05	1.0	4.0

r_h: half-mass radius; t_d: dynamical timescale at half-mass radius; N: number of particles; T: gas temperature; δ: numerical (Plummer) smoothing length (N–body part only); R: cut-off radius; ξ_b: dimensionless cut-off radius, see Bonnor (1956); total mass (stars and gas) of all models was set to 1; all quantities are given in dimensionless code units (see text).

in Table 5.2. Simulations of a cold 10 K molecular gas cloud stabilized initially by a turbulent velocity field will be discussed in the following chapter.

To get a combined system of gas and stars, we add N–body particles with an equal density distribution, scaling the masses of the stars and the gas according to the star formation efficiency ϵ. The velocity dispersion of the particles is chosen according to the temperature of the gas.

Isothermal spheres extend to infinity. In order to get a finite configuration, the gas density is set to zero at an arbitrary radius. To stabilize the gas sphere an external pressure is applied: For each SPH particle, the individual pressure p_i is decreased by the external pressure $p_{\rm ext}$, which is given by the pressure at the cut-off radius of the Bonnor–Ebert sphere:

$$p_{\rm ext} = p(R) = \frac{R}{\mu}\,\rho(R)\,T = \frac{R}{\mu}\,T\,\rho_c\,\exp(\psi(\xi_{\rm max}))\,. \tag{5.2.17}$$

Test calculations with pure gaseous Bonner-Ebert spheres using this procedure were in equilibrium and showed no dynamical evolution. If we convert a certain fraction of the mass inside the Bonnor–Ebert sphere to stars with a given star formation efficiency ϵ, we decrease the density distribution: $\rho_{\rm gas} = (1-\epsilon)\rho$. Equation (5.2.9) is not altered, so the system is still in hydrodynamic equilibrium. But the pressure of the system decreases and we have

$$p_{\rm ext} = \frac{R_{\rm gas}\,T}{\mu}\,(1-\epsilon)\,\rho(R)\,. \tag{5.2.18}$$

The N–body part of the system cannot be supported by an external pressure. Therefore the velocity dispersion of the N–body particles is decreased and the system is allowed to relax until a stable configuration is obtained.

Figure 5.5 shows the evolution of one typical setup prior to gas removal. About 2% of the N–body particles are lost, but after some oscillations the main part achieves an equilibrium state. This configuration is then used as initial model for following investigations. The different models used are shown in Table 5.2.

To completely expel the residual gas from the cluster, the amount of energy fed into the gas must be comparable or greater than the binding energy of the gas, which in case of a homogeneous density distribution for gas and stars is

$$W_{\rm gas} = 4\,\pi \int_0^R (\frac{1}{2}\,\rho_g\,\phi_g + \rho_g\,\phi_s)\,r^2\,dr = \frac{3\,(\epsilon^2-1)\,G\,M_c^2}{5\,R}, \tag{5.2.19}$$

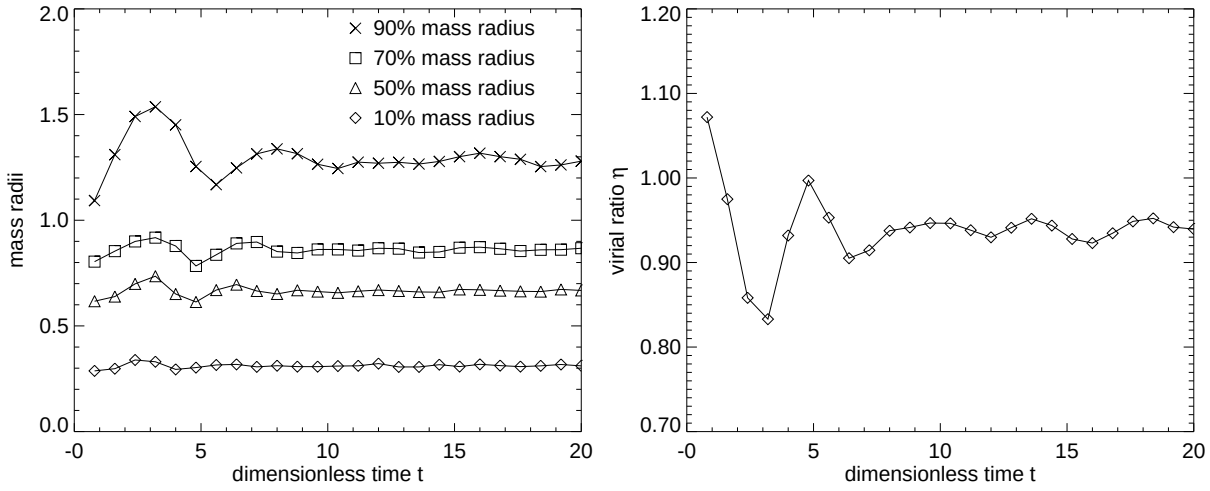

Figure 5.5: *Evolution of the mass radii (left) and virial ratio (right) of a combined N–body and SPH simulation. At the end of the stability test the system is in equilibrium.*

where ρ_g and ϕ_g are the constant density and the gravitational potential of the gas and ϕ_s is the potential of the stars.

As the processes of gas expulsion are not well understood, we choose two simplified scenarios, where the energy input of the stars is high enough to expel all the residual gas: In our first model we heat up the whole gas cloud by a factor of 10. This might resemble a young cluster where the gas is heated up homogeneously by stellar winds or ionizing radiation (see Section 4.2). As a result, the gas starts to expand and is removed. Our models are scale free and can be applied to various initial conditions. For a typical molecular cloud with the parameters given in Section 5.1, the binding energy of the gas is $W_{\rm gas} \approx (\epsilon^2 - 1)\, 5.2 \cdot 10^{42}\,\mathrm{J}$ and the temperature increase is $\Delta T = 2.4 \cdot 10^4\,\mathrm{K}$, which is equivalent to an energy input of $\Delta E = \bar{\gamma}\, M_g\, R_{\rm gas}\, \Delta T/\mu \approx (1-\epsilon)\, 5.9 \cdot 10^{43}\,\mathrm{J}$, where $M_g = (1-\epsilon)\, M_c$ is the mass of the residual gas.

In our second scenario we simulate an outward propagating shock front, disrupting the gas cloud. Such shock fronts may be generated by combined supernova explosions and winds from central high-mass stars. The formation of supershells and their ability to disrupt the cloud are discussed in various papers with regard to chemical self-enrichment of globular clusters (Morgan & Lake 1989; Brown et al. 1995; Parmentier et al. 1999). Goodwin, Pearce & Thomas (2000) investigate single supernovae in gas clouds. In our simulation we heat up a small inner core with radius $R = 0.2$. All 229 SPH particles inside R are heated by a factor of 200. Applying again the typical parameters given in Section 5.1, the temperature increase is $\Delta T = 5.2\,10^5\,\mathrm{K}$, corresponding to an energy input of $\Delta E \approx (1-\epsilon)\, 2.7\, 10^{43}\,\mathrm{J}$. This is less than the typical energy $E_{\rm SN} = 10^{44}\,\mathrm{J}$ of a single supernova. However, it must be taken into account that only a few percent of the supernova energy is fed into the gas (Goodwin, Pearce & Thomas 2000) and therefore several supernovae may be needed to disrupt the cloud.

5.2.2 Evolution of the Cluster During and After Gas Expulsion

Figure 5.6 shows the time evolution of a system with gas ejection in a supershell. The shell reaches a velocity up to 5 times the sound speed of the initial system. Once the internal pressure of the expanding gas is smaller than the adopted external pressure, the outward propagating

shell becomes unstable and develops substructures. At that stage, less than two dynamical timescales after the gas removal started, the gas density in the cluster region is so low that its gravitational effect on the stellar component is negligible. We therefore remove the gas and follow the evolution of the stars alone. The globally heated cloud models show a very similar evolution and are treated in the same manner.

Figure 5.7 corresponds to Figure 5.4 in the pure N–body case. For comparison, the dashed curves reproduce the results of the pure N–body simulations.

For instantaneous gas expulsion (all the gas particles are removed at once), corresponding to the case $t_{\rm exp} = 0$ in Section 5.1, the simulations using the Bonnor–Ebert sphere as initial configuration are in very good agreement with the simulations using a King density distribution. The slightly higher dynamical timescale of the Bonnor–Ebert sphere (see Table 5.2) may cause the small differences for small star formation efficiencies: the simulation was not run long enough for all particles to get unbound. We therefore conclude that the density distribution has no influence on the number of bound particles after gas expulsion, at least if $t_{\rm exp} = 0$.

The asterisks in Figure 5.7, right panel, show system S1 where the temperature of the whole cloud was increased by a factor of 10 with respect to the equilibrium model. The number of bound stars increases slightly compared to the case with instantaneous gas expulsion. The diamonds in the left panel show the results for a cloud centrally heated to $T = 152$ (system S2). Compared to the first model S1, no significant differences are visible. Again, the number of bound stars increases slightly. However, the gas expulsion process in both cases is much faster than the timescales adopted in Section 5.1. Therefore, also in more realistic cases, high star formation efficiencies are needed to sustain a bound star cluster.

One way out may be a collapse of the star cluster before the gas is completely expelled, leading to a higher "effective star formation efficiency". Lada et al. (1984) and Verschueren (1990) proposed a low or zero initial velocity dispersion to explain the collapse. Saiyadpour, Deiss & Kegel (1997) considered the effect of dynamical friction on the stellar cluster.

We implement the first approach by setting the initial velocity dispersion of the stars to zero and heating the whole gas cloud. In each of the simulations, the cluster virializes after gas expulsion within a half-mass radius that is about 40% of the initial radius, or about 2.7 pc applying again the typical units. Only few stars that gain velocities higher than the escape velocity of the cluster are ejected. For a wide star formation efficiency range the percentage of bound stars at the end of the simulations is nearly constant and higher than 80% (Figure 5.7, left panel, triangles). Even our run with the lowest star formation efficiency $\epsilon = 0.02$ leads to a bound system. However, small star formation efficiencies by definition lead to low mass star clusters. In order to obtain observed globular cluster masses, our initial cloud mass has to be rescaled to higher values. Even if this scenario is very unlikely, for reasonable initial conditions bound clusters can be formed with masses and radii similar to observed globular clusters.

5.3 Density Distributions of the Star Cluster after Relaxation

We now study the structural evolution of the star clusters during the gas expulsion and after relaxation. We fit King profiles to the density distribution ρ of the cluster in the following way: The total mass of the cluster was set to the value given by the total mass of bound stars at the given time. Fixing of two more parameters, in this case the scaled central potential W_0 and the tidal radius r_t, determines the King density distribution ρ_k completely. The radial density

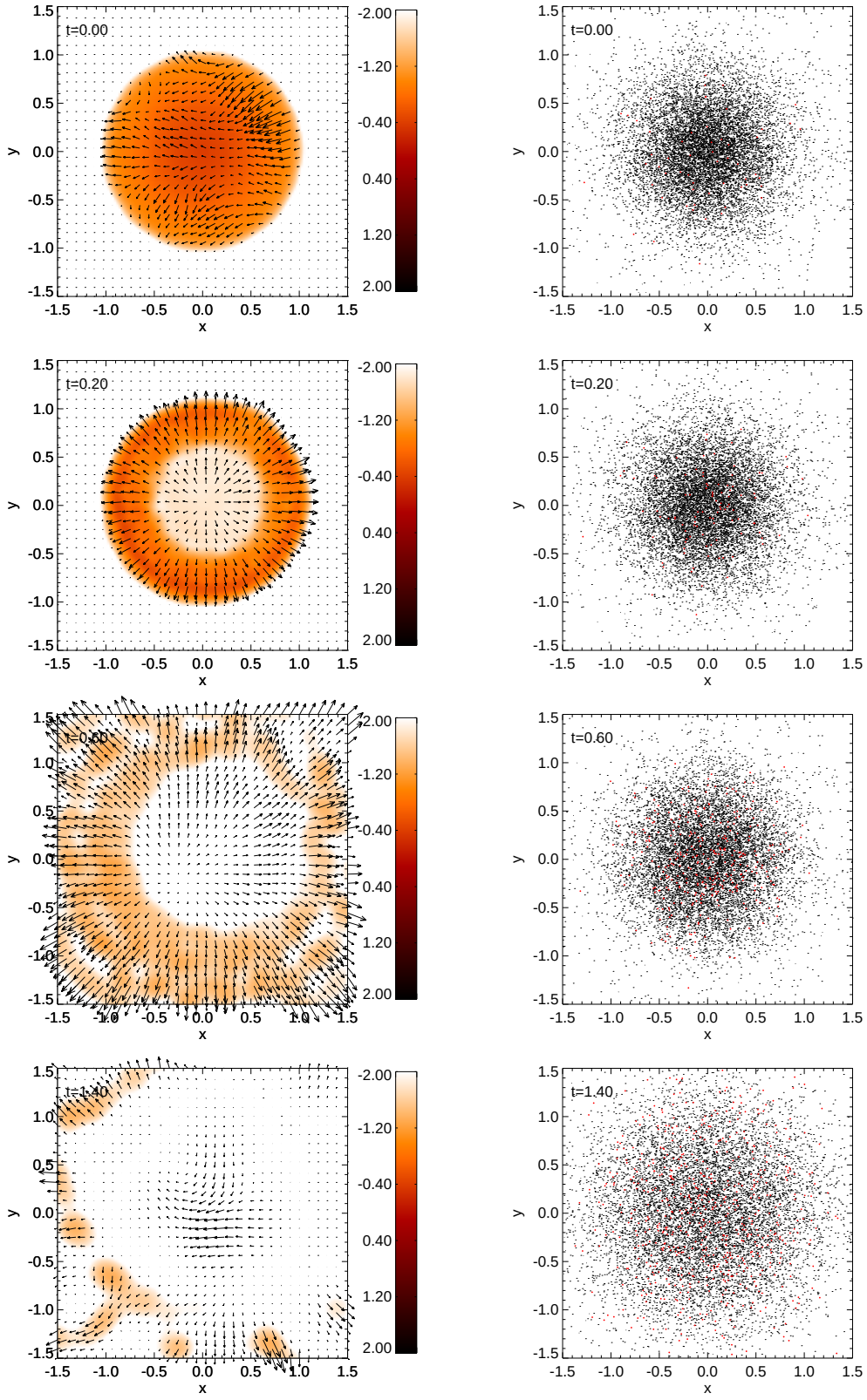

Figure 5.6: *Time evolution of model S2 during the gas expulsion phase (dimensionless time t). The star formation efficiency is $\epsilon = 0.4$ and central heating is applied. The plots show the N–body particles (right) projected onto the x–y–plane; unbound particles are marked red. The left figures show the logarithmic gas density in the x–y–plane; arrows indicate the velocity field.*

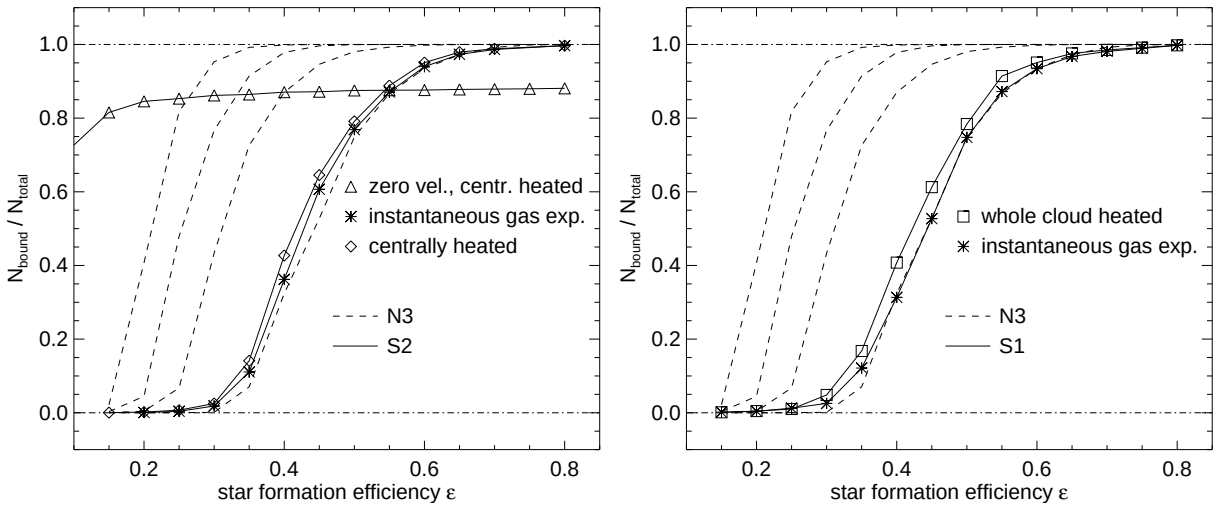

Figure 5.7: *Ratio of the number of bound stars to the initial number of stars in the relaxed system after gas expulsion; dashed lines indicate the results from Figure 5.4, model N3.*

distribution is obtained by dividing the cluster into spherical shells with an equal number of 40 particles for run N3 to keep the error constant over the whole cluster radius. Only bound particles were considered. For the fit, we used tabulated King profiles ρ_k with $W_0 = [1.0, 1.1, \ldots, 9.9, 10.0]$. Now, in a first step, the radius r_t was fitted using an χ^2 fit with

$$\chi^2 = \sum_i \frac{(\rho_k(r_i) - \rho(r_i))^2}{\rho(r_i)} \tag{5.3.20}$$

for all values of the scaled potential W_0. In a second step, the best fit for the scaled potential W_0, regarding the above χ^2, was chosen. Another logarithmic criteria to choose the best W_0 proved useful:

$$\chi^2 = \sum_i (\log \rho_k(r_i) - \log \rho(r_i))^2 \,. \tag{5.3.21}$$

Figure 5.8 shows the fits for different timesteps. In the first timestep, both methods reproduce the initial values. During and shortly after the gas expulsion, deviations from King profiles occur: The density distribution shows an enhancement compared to the King profile in the inner parts and a depression in the outer parts. This may be caused by particles getting unbound preferentially in the outer parts of the system. After relaxation, the profiles again fit well the remaining cluster. The method using the logarithm takes into account that the density varies between several orders of magnitude. As can be seen, this method leads to better fits in the outer parts of the clusters, where the density is low. Thus, the non-logarithmic fit leads to smaller tidal radii and lower W_0. Also, in the time evolution, the logarithmic method shows less scatter. The discrepancies between the two methods show that the errors in determining W_0 are not better than ± 1.0.

The fitted values during the gas expulsion phase have to be taken with caution: From Figure 5.9 we see that during gas expulsion the scaled potential raises fast and relaxes afterwards at a value between 5.0 to 7.0. The diagram also shows the mean scaled potential regarding Milky Way globular cluster as well as intervals containing 50% and 70% of all Milky Way globulars.

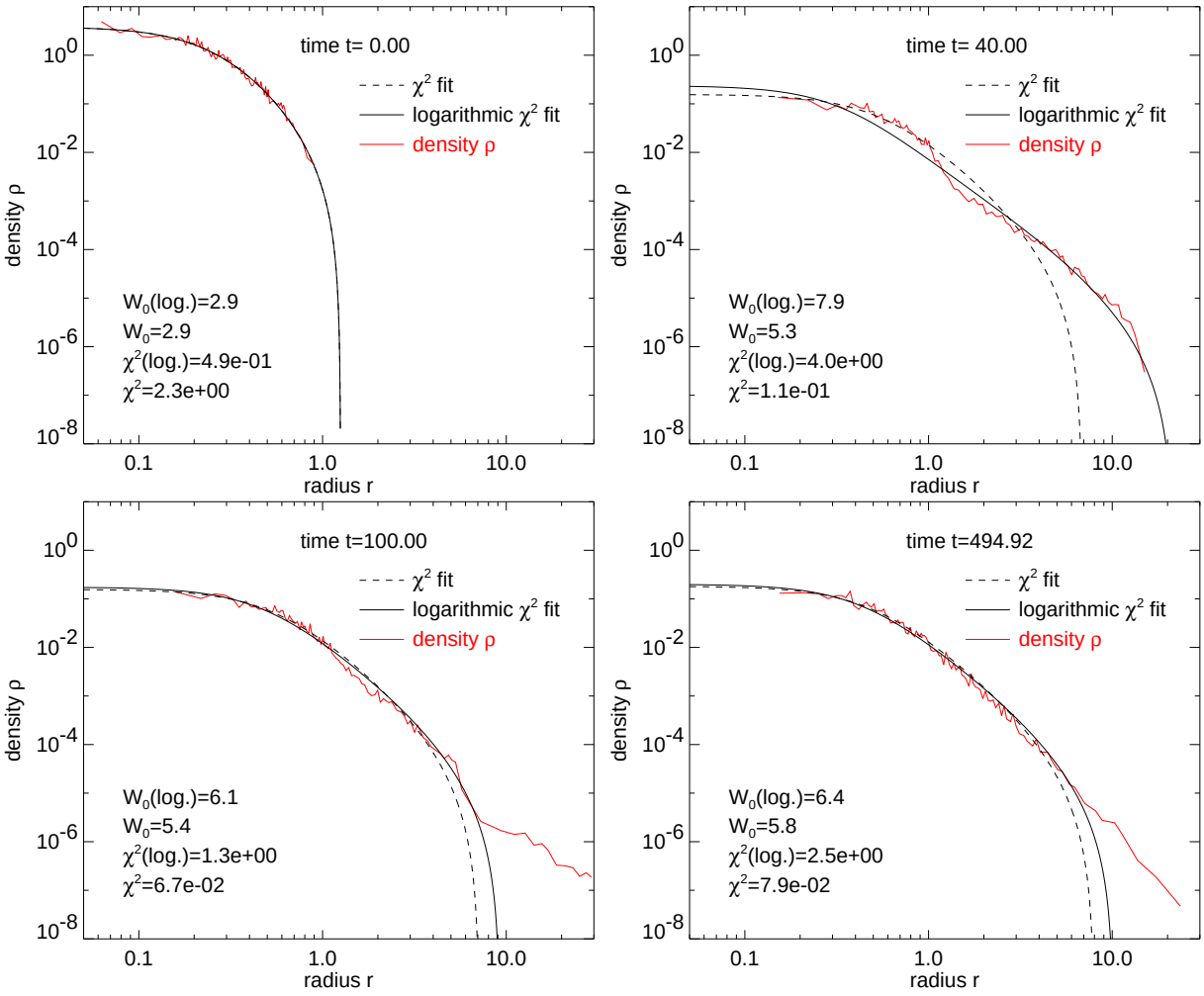

Figure 5.8: *Radial density and fitted King profiles at given timesteps; data taken from model N3, star formation efficiency* $\epsilon = 0.4$ *and expulsion time* $t_{\rm exp} = 2$.

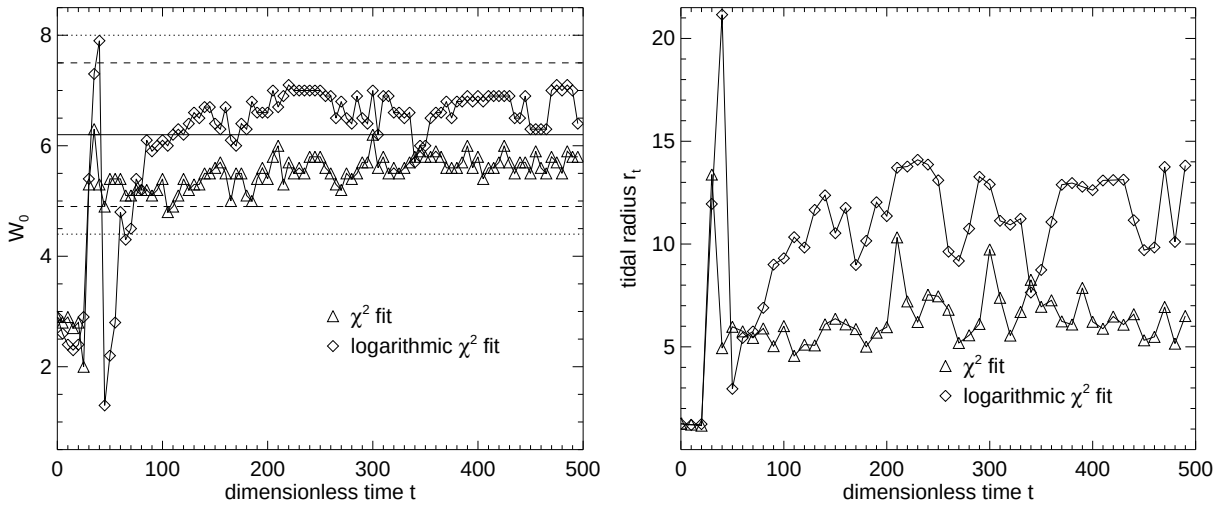

Figure 5.9: *Evolution of the scaled central potential (left) and tidal radius (right), obtained with the two fitting procedures described in the text; data taken from model N3, star formation efficiency* $\epsilon = 0.4$ *and expulsion time* $t_{\rm exp} = 2$*; the horizontal solid line in the left diagram gives the mean scaled potential* W_0 *regarding Milky Way globular clusters (see Figure 2.2). The dashed and dotted lines give the intervals containing 50% and 70% of all Milky Way globulars, respectively.*

Comparing these properties of more than 10 Gyr old clusters to those of the young clusters of our simulations is reasonable, because they are preserved even during this long timescale (Murray & Lin 1992). The good agreement of the chosen exemplary run with the mean scaled potential is of course by chance. The variation of the final scaled potential W_0 with the star formation efficiency for the different expulsion times is shown in Figure 5.10. As one would expect from the global expansion, the clusters tend to increasing concentrations with increasing star formation efficiencies. All obtained values for the scaled potential lie well inside the given intervals. Large scaled potentials can only be obtained in the case of fast or instantaneous gas expulsion or for low star formation efficiencies.

Concluding from these simulations, the obtained relaxed, now gas free clusters, can be well described by King profiles, like a substantial part of today's globular clusters. However, to verify the results simulations with different initial King parameters are necessary. By that, one might be able explain the observed spread in the concentrations of Milky Way globulars (Figure 2.2).

5.4 Conclusions & Outlook

N–body and combined N–body & SPH calculations to investigate the influence of the residual gas expulsion on the stellar part in star forming regions are presented.

We show that in the case of instantaneous gas expulsion, clusters with star formation efficiencies greater than $\epsilon = 0.45$ can keep more than 50% of the initial stars. Clusters with star formation efficiencies less than $\epsilon = 0.40$ are dissolved. Different concentrations of the initial models show no effect at all on the number of bound stars if the gas is expelled instantaneous.

We confirm that gas expulsion timescales which are several times longer than the dynamical timescale of the cluster can decrease the star formation efficiency needed to sustain bound

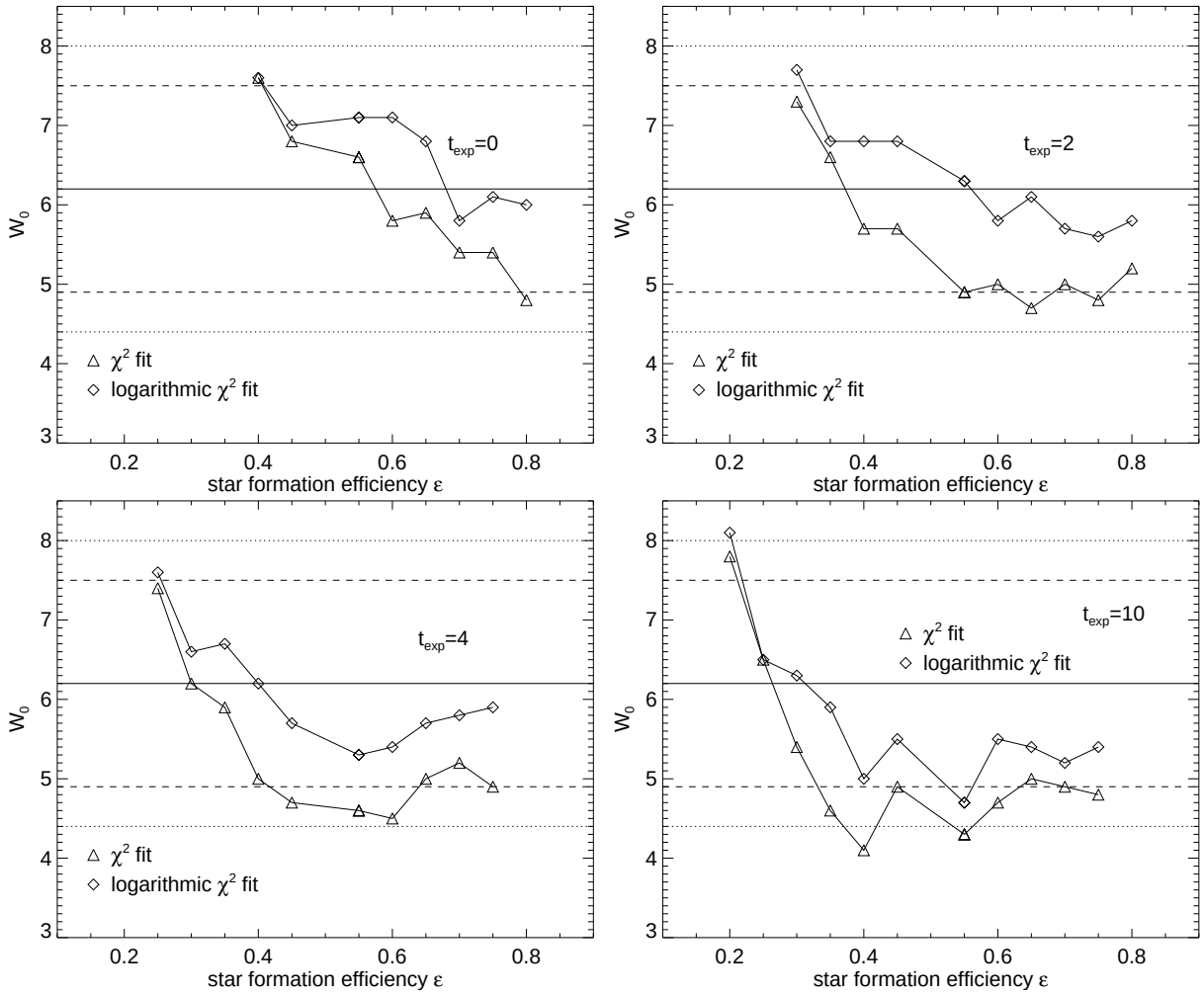

Figure 5.10: *Change in the final scaled potential W_0 with respect to the star formation efficiency ϵ; data taken from model N3; the horizontal solid line gives the mean scaled potential W_0 regarding Milky Way globular clusters (see Figure 2.2). The dashed and dotted lines give the intervals containing 50% and 70% of all Milky Way globulars, respectively.*

clusters considerably.

However, our simulations including the proper dynamics of the residual gas show that in order to destroy the whole cloud by global heating or by supershells the gas expulsion must take place on a short timescale, requiring a high star formation efficiency. Only few star forming regions show such high star formation efficiencies. However, if the global star formation efficiency averaged over a molecular cloud is low, bound cluster can form in regions where the local star formation efficiency is high (Adams 2000).

Another possibility to form bound clusters with small efficiencies is indicated from the recent simulations of Klessen & Burkert (2000) and Klessen & Burkert (2001), who study star formation in turbulent molecular clouds. They find that the stars form preferentially in fragmenting filaments, where most of the turbulent energy is dissipated. The newly-formed protostars have small relative velocities corresponding to virial ratios $\eta = -2\,E_{\rm kin}/E_{\rm pot} < 1$. We demonstrate that models with stars having an initial zero velocity dispersion lead to a compaction of the cluster and can explain bound systems even in low star formation efficiency regions: For star formation efficiencies as low as $\epsilon = 0.15$ more than 80% of the stars stay bound. Bound systems are obtained even with star formation efficiencies lower than 10%. For future investigations it is essential to know the velocity dispersion of newly-born stars in clusters. This initial velocity dispersion may be a relic of the turbulent motions in the initial molecular cloud. In the following chapter, we therefore focus on clustered star formation in a turbulent gaseous environment.

Chapter 6

Numerical Simulation of Massive Cluster Formation

The results of the foregoing chapter showed that strict conditions are necessary to form massive bound stellar clusters. In this chapter we investigate how these circumstances can be achieved during the formation process of the cluster. The formation of a bound stellar system is a race between efficient star formation and feedback processes leading to an expulsion of the residual gas. We start with a description of the initial models, representing giant turbulent molecular clouds with a given power spectrum regarding the velocities. The clouds are thought to be on the onset of instability: In our simulations, they collapse and fragment without an external driver for the turbulence.

First, we examine how the various parameters regarding the star formation and feedback implementation as presented in Chapter 4 affect the star formation process and the structure of the resulting star cluster. In a next step, it is investigated under what circumstances bound massive clusters can form. It will be shown that only rapid and spatial compact star formation will lead to success. The spatial structures and evolution of the young clusters are examined. As cloud collisions have long been proposed as a probable mechanism for triggering massive star cluster formation, we also present a study of a simple head-on collision.

6.1 Initial Models

We choose our initial conditions to match the properties of giant molecular clouds, which are generally believed to be the progenitors of massive star clusters like globular clusters. Gaussian random fields are a useful tool to describe the turbulent random motions in those molecular clouds. After a general description of gaussian random fields the realization used in the following simulations are presented.

6.1.1 Gaussian Random Fields

We realize the initial turbulent velocity field of the molecular cloud using gaussian random fields. Gaussian random fields can be fixed by their mean value, in our case the root mean square (rms) velocity $\sqrt{\overline{v^2}}$, and the power spectrum $P(\vec{k})$ with respect to the wave number k. The power is defined as the absolute value of the Fourier coefficients in k-space and thus determines the distribution of the amplitudes among the different wavelengths of the turbulent perturbations

in $\vec{r}$-space. In the following, we will assume that the power spectrum is isotropic and follows a power law.

Each velocity component $v_j(\vec{r})$ can be described using the Fourier expansion

$$v_j(\vec{r}) = \frac{1}{(2\,\pi)^3} \int \hat{v}_j(\vec{k})\, e^{i\,\vec{k}\vec{r}}\, d^3k\,. \tag{6.1.1}$$

For $v_j(\vec{r})$ to be real, $v_j(\vec{r}) = v_j^*(\vec{r})$, the complex conjugate must obey $\hat{v}_j^*(\vec{k}) = \hat{v}_j(-\vec{k})$. The convolution theorem for Fourier transformations gives the connection between the autocorrelation function and the power spectrum $P(\vec{k}) = |\hat{v}_j(\vec{k})|^2$:

$$\int v_j(\vec{r}\,')\, v_j(\vec{r}\,' + \vec{r})\, d^3r' = \frac{1}{(2\,\pi)^3} \int P(\vec{k})\, e^{-i\,\vec{k}\vec{r}}\, d^3k\,. \tag{6.1.2}$$

A measurable quantity for molecular clouds is the velocity dispersion, which is directly connected to the mean kinetic energy per mass

$$\mathcal{E}_{\rm kin} = \frac{1}{2\,V} \int v_j(\vec{r}\,')\, v_j(\vec{r}\,') d^3r'\,. \tag{6.1.3}$$

Using the above convolution theorem with $\vec{r} = 0$ and assuming an isotropic power spectrum $P(\vec{k}) = P(|\vec{k}|)$, we get

$$\mathcal{E}_{\rm kin} = \frac{1}{2\,V}\, \frac{1}{(2\,\pi)^3} \int 4\,\pi\,k^2\, P(k)\, dk\,. \tag{6.1.4}$$

If one measures the spectral energy, that is the energy of all the modes in the spherical shell in k-space between k and $k + dk$, the connection to the power spectrum will be given by $\hat{\mathcal{E}}(k) \sim k^2\, P(k)$.

For a realization of a gaussian random field, we use the discretized Fourier transformation (see Equation (6.1.1))

$$v_j(\vec{r}) = \frac{L^3}{(2\,\pi)^3} \sum_{\vec{k}} \hat{v}_{j,\vec{k}}\, e^{i\,\vec{k}\vec{r}}\,, \tag{6.1.5}$$

and assume that real and imaginary part of the Fourier coefficients $\hat{v}_{j,\vec{k}} = u_{j,\vec{k}} + i\, v_{j,\vec{k}}$ are gaussian distributed with variance $\sigma^2 = P(k)$:

$$\mathcal{P}(u,v) = \frac{1}{2\,\pi P(k)}\, e^{-\,(u^2+v^2)/2P(k)}\,. \tag{6.1.6}$$

Variable transformation to spherical coordinates gives a uniform probability density function for the phase ϕ

$$\mathcal{P}(\phi) = \frac{1}{2\,\pi} \tag{6.1.7}$$

and the Rayleigh distribution for the amplitudes w of the Fourier coefficients $\hat{v}_{j,\vec{k}} = w(\cos\phi + i\,\sin\phi)$:

$$\mathcal{P}(w) = \frac{w}{P(k)}\, e^{-\,w^2/2\,P(k)}\,. \tag{6.1.8}$$

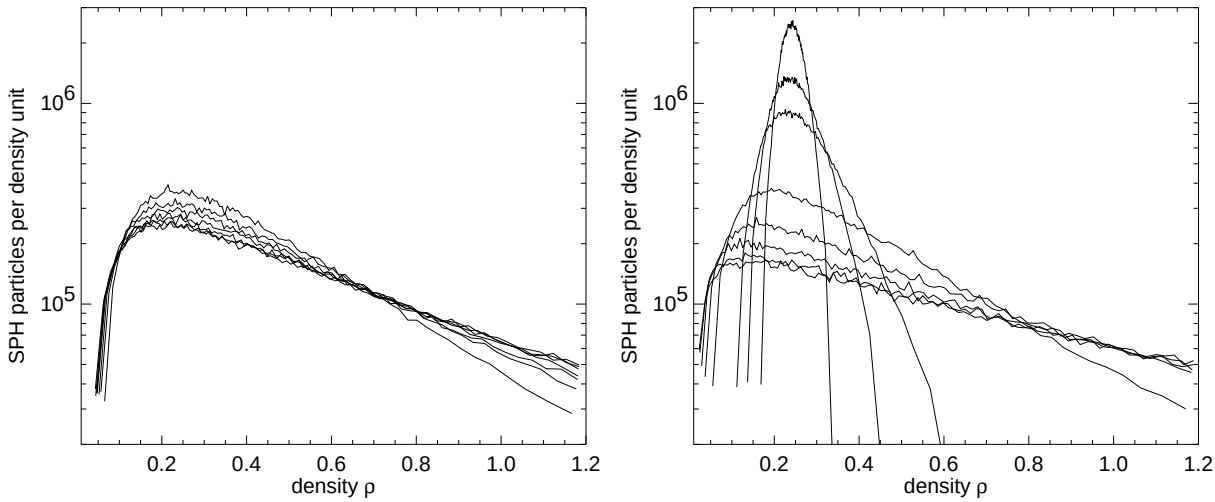

Figure 6.1: *Time evolution of the number of particles per density unit for both initial runs.* ***Left:*** *Model HIGH2,* $P(k) \sim k^{-2}$*. From top to bottom the lines show the timesteps* $t = 0.04, 0.08, 0.12, 0.16, 0.20, 0.24$ *and* 0.28*.* ***Right:*** *Model HIGH4,* $P(k) \sim k^{-4}$*. Shown timesteps are* $t = 0.01, 0.02, 0.03, 0.08, 0.13, 0.18, 0.23$ *and* 0.28*.*

This leads to the probability function $\mathcal{P}(X < w) = \int_{-\infty}^{w} \mathcal{P}(w)$ or

$$\mathcal{P}(X < w) = e^{-\,w^2/2\,P(k)}\,, \tag{6.1.9}$$

with maximum at $w = \sqrt{P(k)}$. While ϕ is equally distributed between $[0, \ldots, 2\,\pi]$, the discrete values for w can be derived by throwing a dice to get random numbers $\mathcal{P}(X < w)$ with $0 < \mathcal{P}(X < w) < 1$ and using

$$w = \sqrt{-2\,\ln(\mathcal{P}(X < w))\,P(k)}\,. \tag{6.1.10}$$

6.1.2 Realizations

To get our initial conditions for cluster forming molecular clouds, we start with a cube with length 2 in dimensionless units. Dubinski, Narayan & Phillips (1995) successfully describe the power spectrum with the Kolmogorov law $P(k) \sim k^{-11/3}$. Myers & Gammie (1999) suggest that most observed line width-size relations of molecular clouds can be produced by spectral energy laws $\hat{\mathcal{E}}(k) \sim k^p$ with $p \simeq -1 \ldots -2$. With Equation (6.1.4), this induces a power spectrum $P(k) \sim k^n$ with $n = -3 \ldots -4$. Burkert & Bodenheimer (2000) also show that such power laws can reproduce the observed projected rotational properties of molecular cloud cores. For our simulations, we use two different power laws $P(k) \sim k^{-2}$ and $P(k) \sim k^{-4}$. Table 6.1 summarizes the properties of the models. We superimpose gaussian random fields for the velocity components v_x, v_y, v_z and let the gas evolve without self-gravity but with periodic boundaries until an equilibrium in the density distribution of the gas particles is reached (Figure 6.1). The periodic force correction using the Ewald method is described by Klessen (1997). Without a driver, the turbulence starts decaying (Figure 6.2). We chose the initial rms velocity such that, as equilibrium is reached, the rms velocity is roughly 1.4 in dimensionless units. Compared to

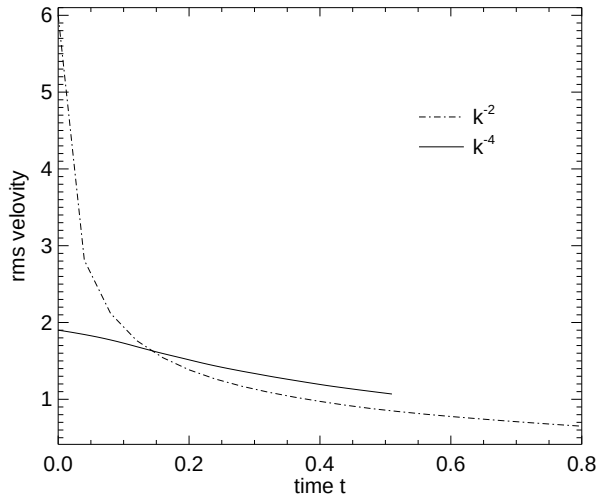

Figure 6.2: *Time evolution of the rms velocities of models HIGH2 and HIGH4 for obtaining initial conditions.*

Table 6.1: *Properties of the Realizations*

Model	Particles (cube)	Particles (sphere)	Power law	rms vel. start	rms vel. end
LOW2	80000	40000	k^{-2}	6.0	1.38
LOW4	80000	40000	k^{-4}	1.9	1.41
HIGH2	200000	100000	k^{-2}	1.9	1.38
HIGH4	200000	100000	k^{-4}	5.5	1.42

Properties of the realizations ("cube") which are then used as the initial models for the following simulations ("sphere"). In dimensionless units, the temperature of each models is $T = 0.0092$. *With the total mass* $m = 1.9$ *and the cube length* $l = 2$, *the mean initial density is* $\bar{\rho} = 0.24$. *The dynamical timescale using this mean density is* $t_d = \bar{\rho}^{-1/2} = 2.1$. *The mean isothermal sound speed is* $a_T = (T/\bar{\gamma})^{1/2} = 0.08$.

the dimensionless isothermal sound speed $a = 0.08$, this gives a turbulent Mach number $M = 18$. The slightly higher value compared to the typical one given in Chapter 2.3 ($M = 10$) makes sure that the turbulent velocity field sustains long enough during the simulations to study its effects. To get a roughly spherical cloud, we dropped particles outside the radius 1 and took this as our initial conditions for the following simulations.

Figures 6.3 and 6.4 show the power spectra of the x–component of the velocity for the initial realizations and for those timesteps, which are then used as the initial models for the following simulations. In all cases, for low values of k, the slope of the power laws k^{-2} and k^{-4} is reproduced well. Figure 6.5 shows the time evolution of the density and the velocity field of the runs HIGH2 and HIGH4. It is clearly visible, that the length scale of the turbulence in HIGH4 (k^{-4}) is greater, when compared to HIGH2 (k^{-2}). The energy stored in the modes in HIGH4 is shifted to longer wavelengths. In the following Sections, the feedback rates are scaled, following Section 4.4, to a molecular cloud with mass $\hat{M} = 10^5\,M_\odot$ and radius $\hat{R} = 50\,\mathrm{pc}$.

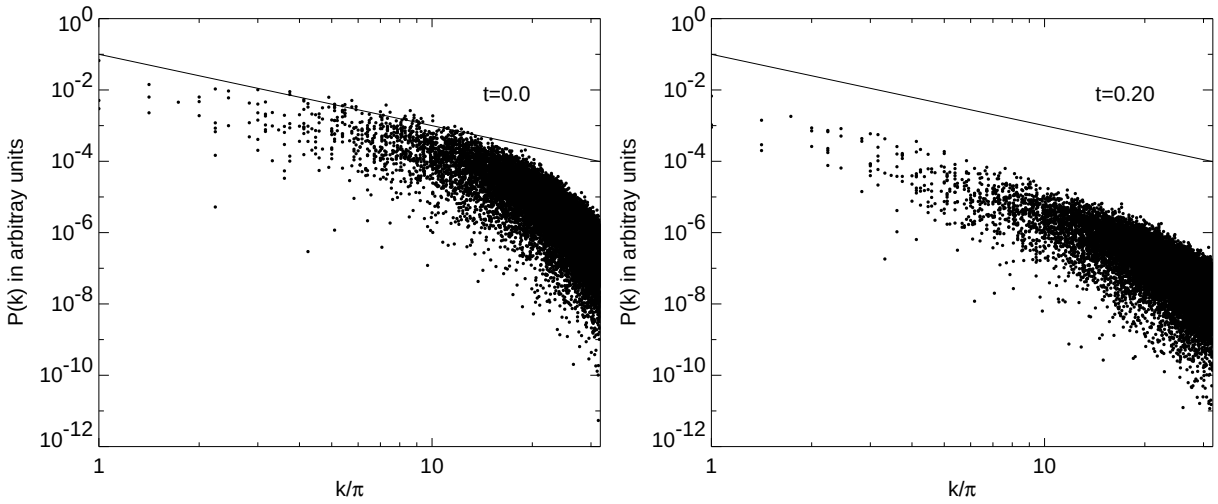

Figure 6.3: *Model HIGH2: Discrete power spectrum of the x component of the velocity at time $t = 0.0$ (initial realization, left) and $t = 0.20$ (starting model for further runs, right). The straight line indicates $P(k) \approx k^{-2}$.*

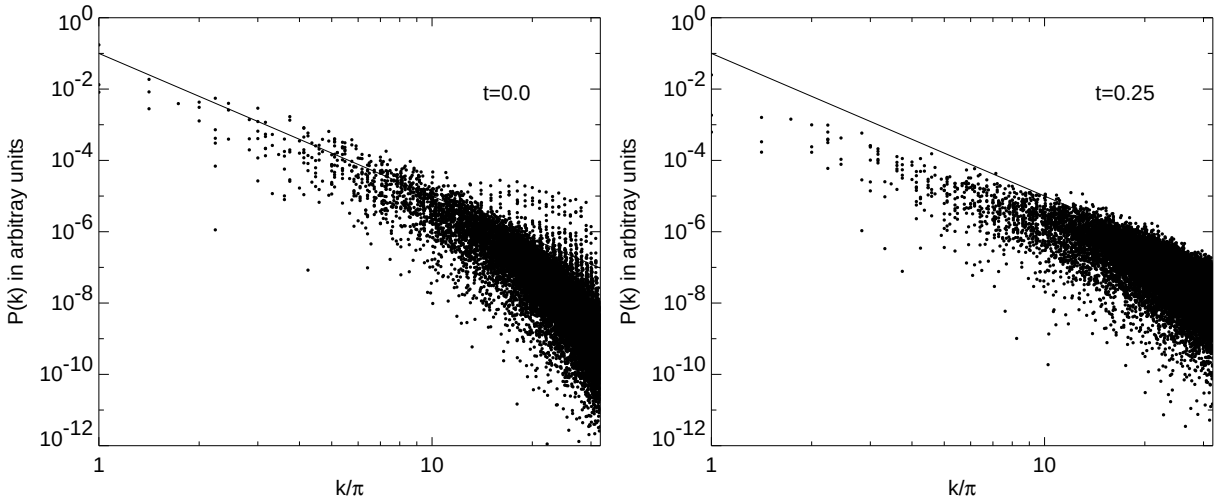

Figure 6.4: *Model HIGH4: Discrete power spectrum of the x component of the velocity at time $t = 0.0$ (initial realization, left) and $t = 0.25$ (starting model for further runs, right). The straight line indicates $P(k) = k^{-4}$.*

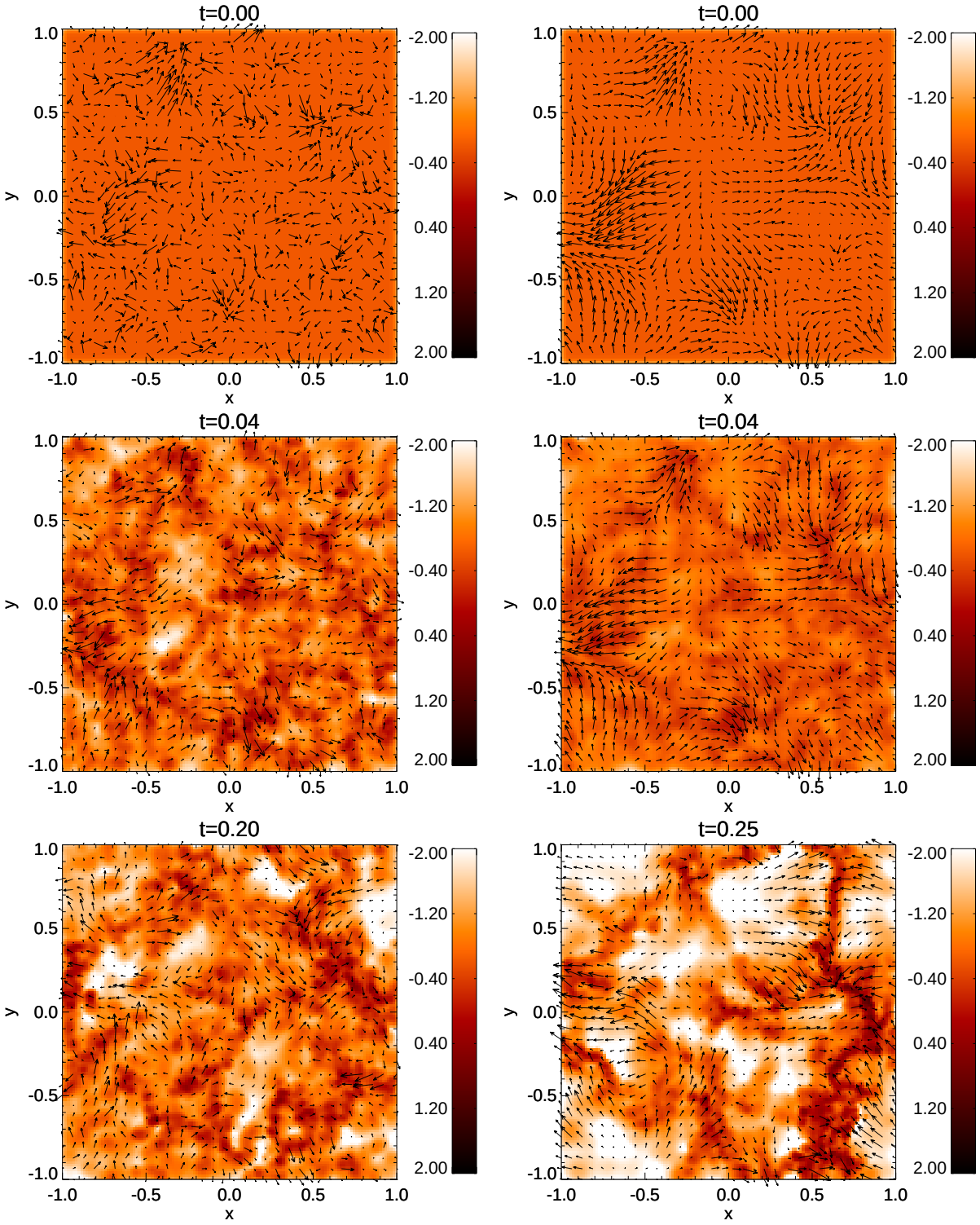

Figure 6.5: *Cut through the logarithmic density (color encoded) and velocity fields (indicated by arrows) at the spatial coordinate $z = 0$ of models HIGH2 (left) and HIGH4 (right). It is clearly visible that in model HIGH4 most energy is stored in the long wavelength modes.*

Table 6.2: *Initial Models for Cluster Formation Runs*

name	initial	power spectr.	$\rho_{\rm global}$	heating	$t_{\rm delay}$	time crit.?	$\epsilon_{\rm final}$
L1	LOW2	k^{-2}	0.0	low	0.0	yes	0.050
L2	LOW2	k^{-2}	0.0	high	0.0	yes	0.052
L3	LOW4	k^{-4}	0.0	low	0.0	yes	0.067
L4	LOW4	k^{-4}	0.0	high	0.0	yes	0.073
L5	LOW2	k^{-2}	10.0	low	0.0	no	0.046
L6	LOW2	k^{-2}	10.0	high	0.0	no	0.046
L7	LOW4	k^{-4}	10.0	low	0.0	no	0.066
L8	LOW4	k^{-4}	10.0	high	0.0	no	0.074
L9	LOW2	k^{-2}	10.0	low	0.01	no	0.053
L10	LOW2	k^{-2}	100.0	low	0.1	no	0.16
L11	LOW2	k^{-2}	100.0	low	0.01	no	0.043
L12	LOW2	k^{-2}	100.0	low	0.05	no	0.093
L13	LOW2	k^{-2}	10.0	low	0.05	no	0.12
L14	LOW2	k^{-2}	10.0	low	0.1	no	0.15
H1	HIGH2	k^{-2}	100.0	low	0.1	no	0.16
H2	HIGH4	k^{-4}	100.0	low	0.1	no	0.15
M1	LOW4	k^{-4}	100.0	low	0.1	no	0.24
M2	LOW2	k^{-2}	0.0	low	0.0	yes	0.088
M3	LOW4	k^{-4}	0.0	low	0.0	yes	0.10
M4	LOW2	k^{-4}	100.0	low	0.05	no	0.17

The initial models are described in Section 6.1.2; "time crit." tells whether the time criterion from Section 4.1 was used or not; $\rho_{\rm global}$ gives the assumed density threshold, also described in Section 4.1; $t_{\rm delay}$ gives the time delay for the heating as given in Section 4.4; the terms "low" and "high" heating refer to the heating rates by stellar winds and ionizing radiation, respectively, also given in Section 4.4; $\epsilon_{\rm final}$ is the final star formation efficiency of the runs; all quantities are given in dimensionless code units (see text).

6.2 Dependencies on Star Formation and Feedback Implementation

After the initial conditions have been fixed, we are now able to follow the collapse and fragmentation of single molecular clouds to investigate under what circumstances bound or unbound massive stellar clusters can form. During the collapse, the turbulence dissipates. Star formation and feedback are implemented as described in the Sections 4.1 and 4.4. Table 6.2 gives a list of the simulations that have been done using various sets of parameters.

Figure 6.7 compares the models L1 to L8 with shallow (left) and steep (right) initial power laws. The different implementations of the star formation criteria and heating applied in these runs only give slightly different star formation efficiencies and rates. The final star formation efficiency in all cases is less than 10% and no bound cluster is formed – the stellar system expands. Runs with the steeper power law k^{-4} initially show higher density contrasts, causing higher star formation efficiencies. Comparing the star formation rates, the runs based on LOW4

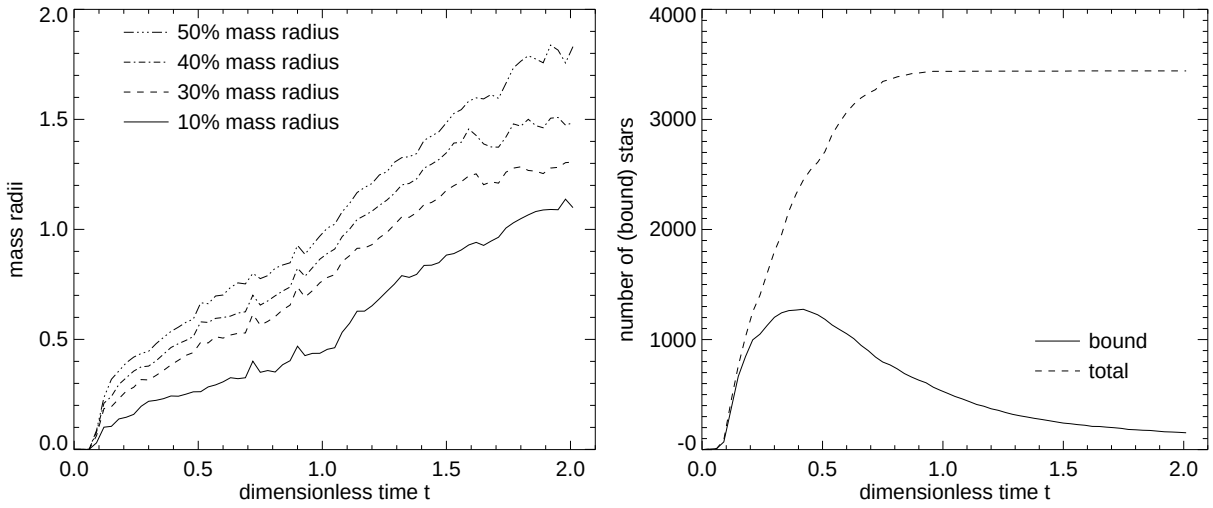

Figure 6.6: *Time evolution of simulation L4;* ***Left:*** *Mass radii;* ***Right:*** *total number of N–body particles and number of bound N–body particles.*

show that star formation starts earlier in the evolution and the rates have a steeper rise than the ones based on LOW2.

All these simulations end up in an unbound expanding association of stars. Figure 6.6 examplarily shows the evolution of the mass radii and the number of bound particles in simulation L4. At the end nearly all the stars are unbound in the system of stars and gas. The expansion will even be enhanced when all the gas has left the system.

The unboundness of the formed star clusters is caused by the low star formation efficiencies combined with large spatial extension of the formed stellar system, which causes low absolute values of the potential energy. In addition, the high velocities of the newly-formed stars due to the collapse of the molecular cloud enhance the expansion process. Examples of the gas density evolution and the structure of the forming stellar clusters will be shown in the following sections.

It is noteworthy that the whole star formation process in all simulations takes place within a dimensionless time of 1, which is about half the initial mean dynamical timescale (see Table 6.1). This rapid star formation matches the conclusions of Elmegreen (2000), who states that if molecular clouds form stars, they will do so in a time that is of order of the dynamical time of the cloud. In that picture there is no need to explain how self-gravitating molecular clouds can support themselves for longer than the dynamical timescale.

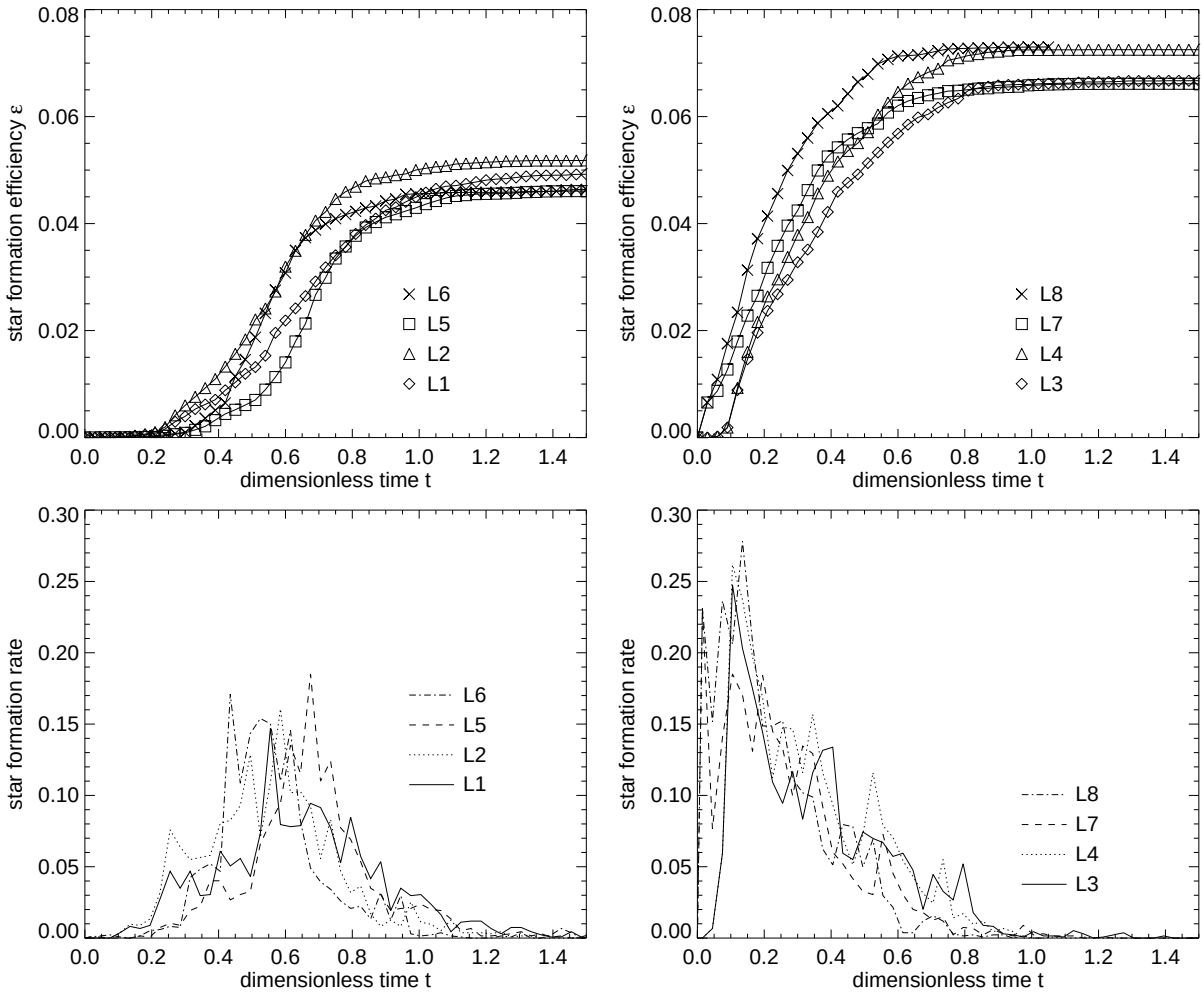

Figure 6.7: *Study of the star formation efficiency (top) and star formation rate (bottom) for the low resolution models with initial power laws k^{-2} (left) and k^{-4} (right). The star formation rate is given in dimensionless units. With the typical mass and spatial scale factors $\hat{M} = 10^5\,M_\odot$ and $\hat{L} = 50\,\mathrm{pc}$, a dimensionless rate 1.0 corresponds to $6 \cdot 10^{-3}\,M_\odot/\mathrm{yr}$ in physical units. Name of the runs as explained in Table 6.2.*

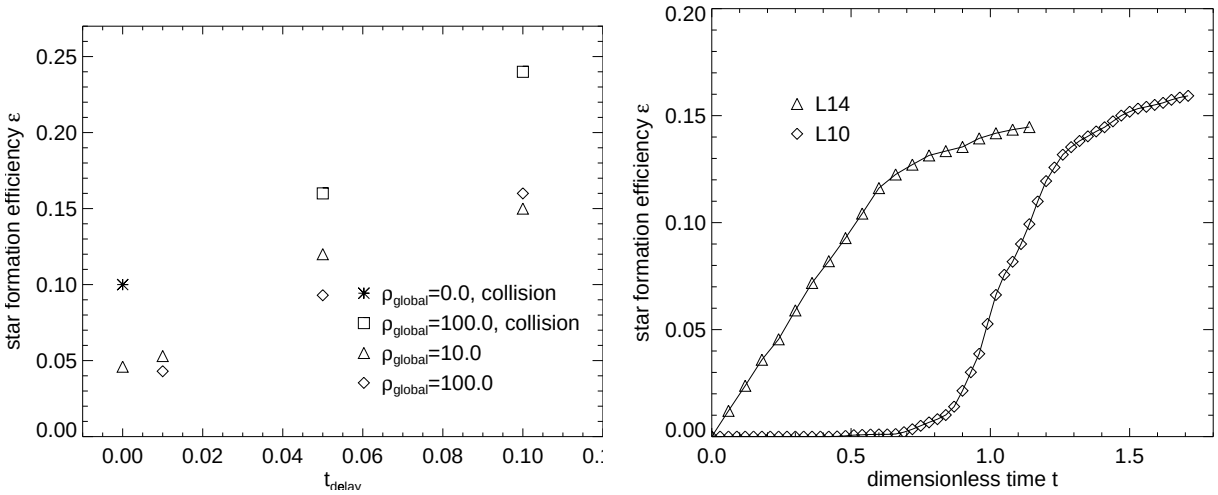

Figure 6.8: ***Left:*** *Dependence of the final star formation efficiency on the chosen time delay* $t_{\rm delay}$ *and the global density threshold* $\rho_{\rm global}$*; Data taken from Table 6.2; also shown are the results from cloud collisions presented in Section 6.5.* ***Right:*** *Time evolution of the star formation efficiencies of run L10 (*$\rho_{\rm global} = 100.0$*) and run L14 (*$\rho_{\rm global} = 10.0$*).*

6.3 On the Way to Bound Star Clusters

The simulations of the foregoing section ended in unbound, expanding stellar systems. We now look for parameters, which increase the star formation efficiency as well as the compactness of the forming cluster and thus may lead to bound clusters.

The interplay between the timescale on which a substantial part of the stars has formed and the heating timescale of the surrounding medium due to feedback essentially influences the star formation efficiency. Figure 6.8 (left) shows the dependency of the star formation efficiency on the chosen time delay, as described in Section 4.4. The higher the time delay, the longer is the time that the surrounding gas can form stars before being stopped by feedback processes, and consequently, the higher is the star formation efficiency.

The final star formation efficiencies for the single cloud models including time delay are in good agreement with recent globular cluster formation simulations done by Nakasato, Mori & Ken'ichi (2000) using SPH, too. They do not take into account the turbulent structure of the initial cloud, but include heating and cooling processes. They obtain efficiencies between 9% and 15%, depending on the number of particles and feedback parameters they use.

To conclude, a temporally delayed feedback process promotes rapid star formation. In run L10, which uses a time delay of $t_{\rm delay} = 0.1$ and also a global density threshold $\rho_{\rm global} = 100.0$ (see Section 4.1), the first stars form at $t = 0.45$. As estimated in Section 4.4, the fraction of OB stars is about $\kappa = 0.0054/M_\odot$, which means that feedback does not start before roughly 200 solar masses of stars have formed. This threshold is reached at time $t = 0.69$. The assumed time delay $t_{\rm delay} = 0.1$ is therefore reasonable. However, the star formation rate will increase substantially with time and the time delay derived from this argument decreases.

Another support for implementing a time delay is that it is still unclear when high mass stars form – there could be a correlation between formation time and stellar masses. If massive stars formed lately, the time delay could be even greater. Besides that, compact H II regions

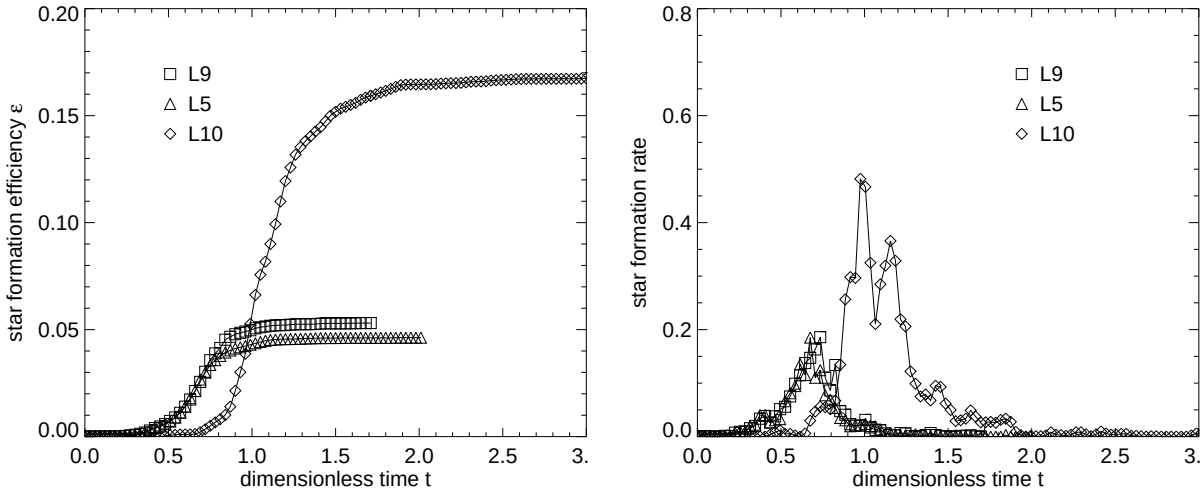

Figure 6.9: *Comparing runs with different global density criteria and time delays.* ***Left:*** *Star formation efficiency;* ***Right:*** *Star formation rate; units as in Figure 6.7.*

could also delay the effect of the ionizing radiation.

Also, star formation takes a finite time. In our simulations, a time delay of 0.1 corresponds to about $1.7 \cdot 10^6$yr. Scaling to other giant molecular cloud dimensions, given by the analysis of Elmegreen & Falgarone (1996), with radius $\hat{R} = 10\,\mathrm{pc}$, keeping the mass $\hat{M} = 10^5\,M_\odot$, we get the global time unit $\hat{t} = 1.5 \cdot 10^6$yr. A time delay of $t = 0.1$ then corresponds to $1.5 \cdot 10^5$yr, which is a reasonable timescale for star formation.

Another important parameter is the global density threshold. In run L10, we choose a global dimensionless density of $\rho_{\mathrm{global}} = 100.0$, which corresponds, if we use the scaling of Section 6.1.2, to a number density of $n = 1.4 \cdot 10^3\,\mathrm{cm}^{-1}$, which is reasonable for dense clumps inside molecular clouds. Even if Figure 6.8 (left) shows that the threshold ρ_{global} has only little effect on the final star formation efficiency, the effects on the structure of the stellar clusters are important.

Figure 6.9 compares star formation efficiencies and rates of run L10, including a high time delay, with runs with lower (L9) and no time delay and lower global density criterion (L5). Once the global density threshold is reached in run L10, rapid, spatial compact star formation starts and leads to a global star formation efficiency of more than 15%.

To work out the differences, we look at the time evolution of the gas density and the stellar system for run L5 (Figure 6.11) and L10 (Figure 6.12). In simulation L5, stars start forming very early. After a notable amount of stars has formed, feedback takes over and drives the gas out of the central region. At late stages, only some star formation still goes on in the outer parts of the molecular cloud, where the outwards driven gas shell compresses the gas. In the end, we get a spatially extended, still expanding stellar association.

In run L10, on the other hand, star formation starts later. One can see that even at the time the feedback takes over and the inner region of the cluster is already gas-free, the star cluster shows lots of spatial structures on different scales. As we may see from the time evolution of the star formation efficiencies in Figure 6.8 (right), the higher global density threshold postpones the star formation. At that time, the high density regions of the underlying molecular cloud are already in a late stage of collapse. Stars form very rapid and spatially concentrated.

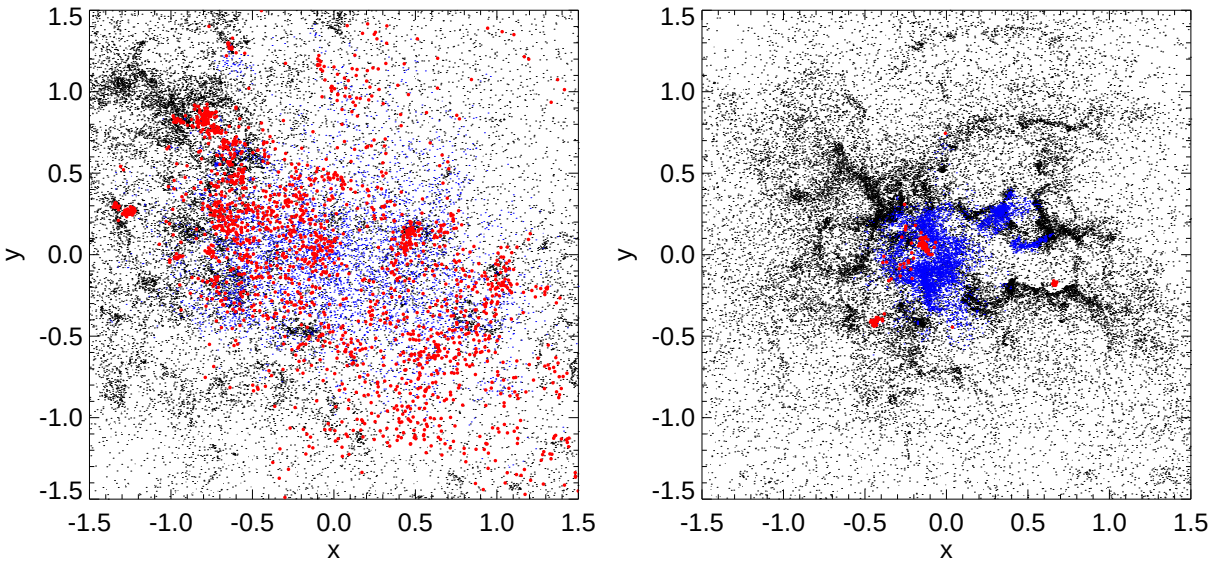

Figure 6.10: *Projection on the x–y plane of the final state of the runs with same time delays* $t_{\mathrm{delay}} = 0.1$*, but different global density criteria; Black dots: SPH particles; blue dots: bound N–body particles; red dots: unbound N–body particles;* ***Left:*** *Run L14,* $\rho_{\mathrm{global}} = 10.0$*;* ***Right:*** *Run L10,* $\rho_{\mathrm{global}} = 100.0$*; Shown are the timesteps where the star formation efficiency* $\epsilon = 0.14$ *in both cases.*

Elmegreen (2000) points out that rapid star formation should lead to hierarchical structures, connected to the structures of the underlying molecular cloud. E.g. Lada & Lada (1995) have shown that the density distributions of the cluster OC 348 shows significant substructures. Elmegreen (2000) also stresses that star formation does not take place everywhere in the cloud, but only in distinct cores. Even if this cores only comprise a small fraction of the initial gas mass, the local star formation efficiency can be much higher and could lead to bound clusters, as shown afterwards.

In detail, Figure 6.10 shows the strong influence of the global density threshold on the spatial distribution of stars: In the case of a low density threshold $\rho_{\mathrm{global}} = 10.0$, the newly-formed cluster shows a large spatial extension and a large fraction of stars (red dots) is unbound and will leave the system of stars and gas. Using the high density threshold $\rho_{\mathrm{global}} = 100.0$, the simulations result in a compact cluster where the majority of stars is bound. So even if the star formation efficiency in both runs is approximately the same, the dynamics of the resulting system is completely different.

Chappell & Scalo (2001), who examine the effects of stellar winds on the gas and star formation in galaxies in two dimensional simulations, showed that wind-driven gas networks build up. Varying the time delay between $2.5 \cdot 10^6$ yr and $10 \cdot 10^6$ yr, they find that the star formation rate and the clustering of the forming stars is enhanced in the case of large delays, giving the same qualitative results as our simulations.

To validate the boundness or unboundness of the stellar cluster, we examine the binding energy of the stellar parts of the simulations. Figure 6.13 compares the energies of all N–body particles and Figure 6.14 the virial ratios of the bound particles from run L5 and L10. In both

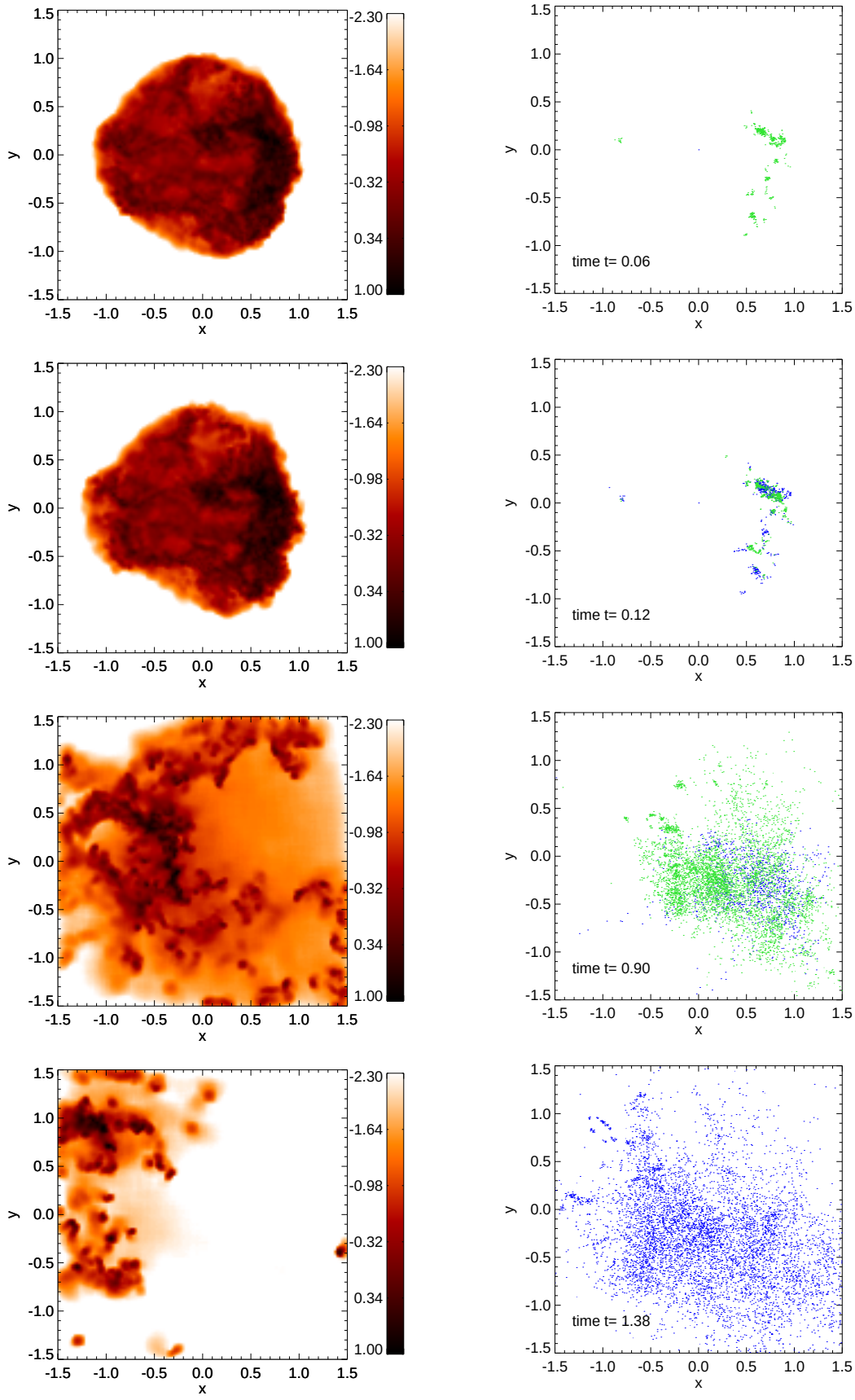

Figure 6.11: *Run L5. Logarithmic column densities (left) and stars (right) for various time steps. New stars with respect to the last shown timestep are marked green.*

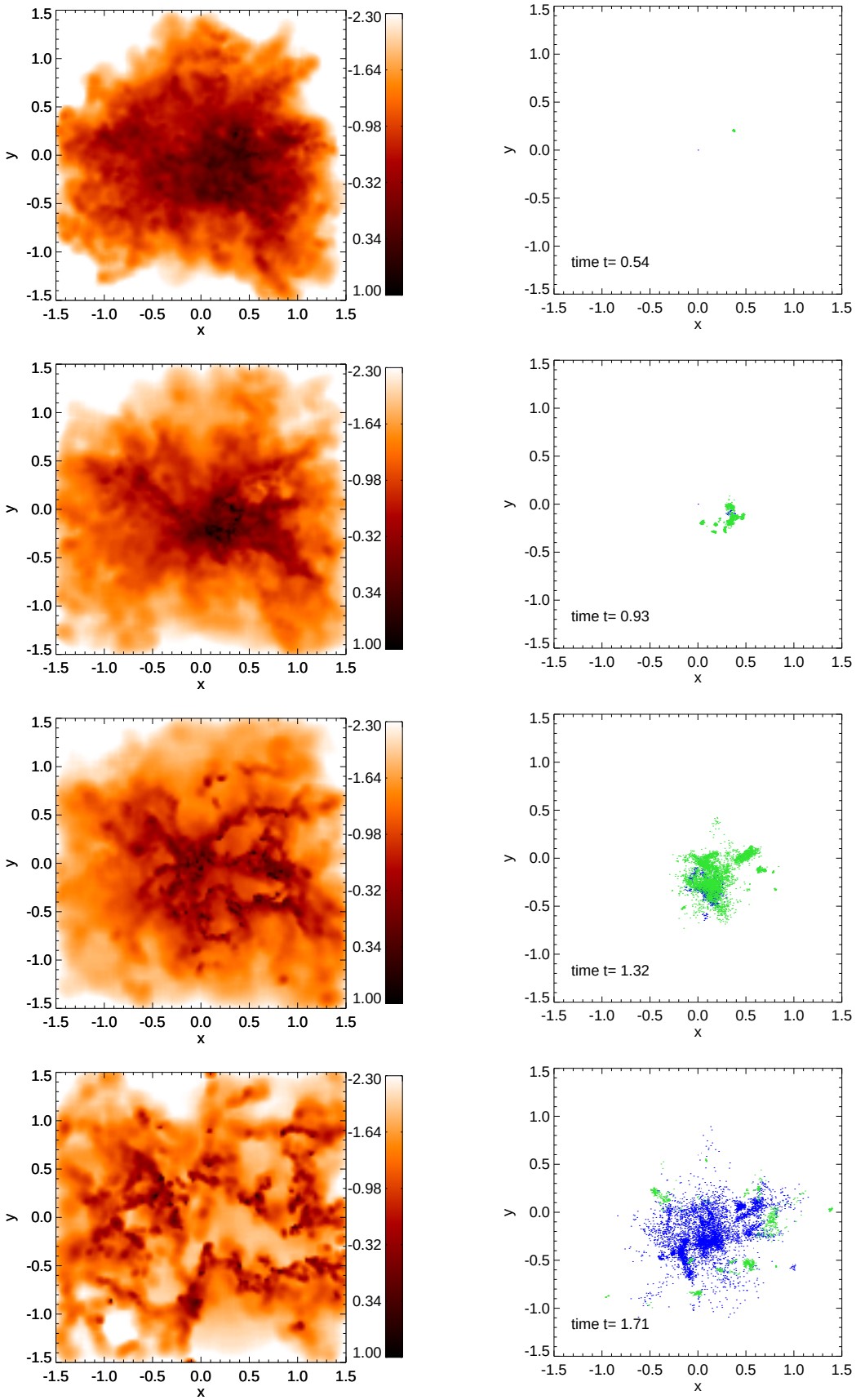

Figure 6.12: *Run L10. Logarithmic column densities (left) and stars (right) for various time steps. New stars with respect to the last shown timestep are marked green.*

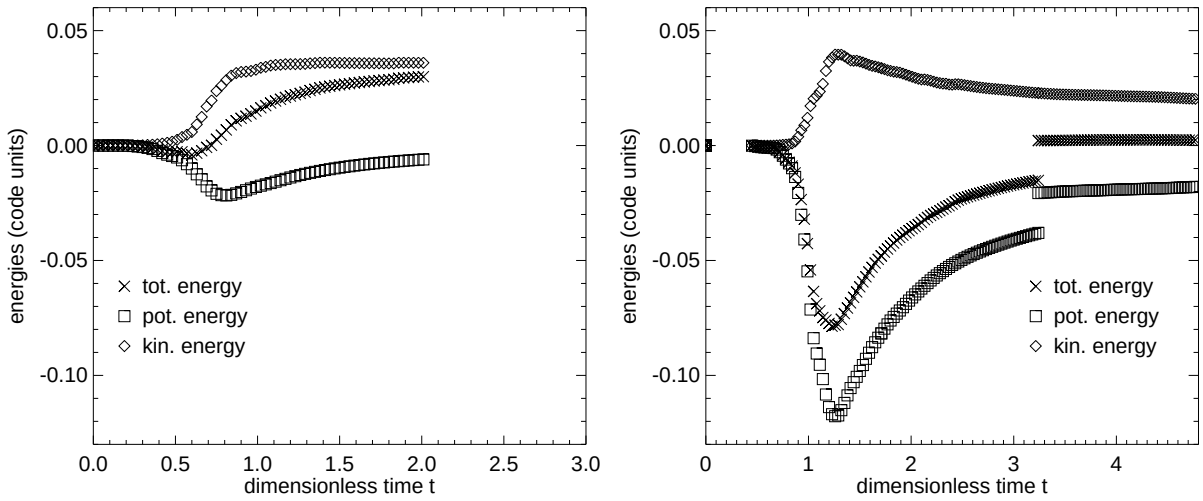

Figure 6.13: *Kinetic, potential and total energy of all N–body particles included in the simulation at the given times.* ***Left:*** *Run L5;* ***Right:*** *Run L10; the unsteadiness comes from the sudden removal of the gas by hand.*

cases, the total kinetic energy of the particles shows a steep rise caused by the increasing total number of N–body particles. In Run L5, the total energy of the stars gets greater than zero long before the end of the simulations, reflecting that most of the stars are unbound. Contrary, in Run L10, the minimum of the potential energy is much lower, such that the total energy remains less than zero nearly all the time. To be able to follow the simulations and confirm the boundness of the cluster, at $t = 3.24$ all the gas still left in the system was suddenly removed by hand. As shown in Chapter 5.1.3, this is the most destructive case of gas expulsion. Even this most severe interference with the system unbinds only a small fraction of the stars (Figure 6.15). This confirms that the majority of stars in this simulations are bound to the system.

Figure 6.16 shows the configuration of the system at time $t = 1.71$. At that time, already most of the gas has been driven out of the central region of the cluster. Clearly two distinct clusters of stars can be seen. Observations of double clusters exist: E.g. Gilmozzi et al. (1994) give actual Hubble Space Telescope (HST) observations of the young double cluster NGC 1850 in the Large Magellanic Cloud (see Figure 2.4).

In the simulation, the distinct clusters are bound together and are likely to merge in the future. However, in the tidal field of a galaxy, the system of subclusters might be disrupted. A first approximation of the tidal cut-off radius r_t, regarding the host galaxy as a point mass, is given by Spitzer (1987):

$$r_t = (\frac{m_c}{2\,M_g})^{1/3}\,R_g\,. \tag{6.3.11}$$

We use exemplarily the mass of our Galaxy, $M_g = 2 \cdot 10^{11}\,M_\odot$, and the typical distance of globulars from the galactic center, $R_g = 12\,\mathrm{kpc}$. The mass of the central cluster in the simulations is about $m_c' = 0.07$ in code units. Using the mass and spatial scale factors $\hat{M} = 10^5\,M_\odot$ and $\hat{L} = 50\,\mathrm{pc}$, the dimensionless tidal radius is $r_t' = 0.6$, which is of the same order as the spatial extension of the stellar cluster. In the regarded case, the subcondensations might float away instead of merging. However, in the less strong tidal field of e.g. the Large Magellanic Cloud,

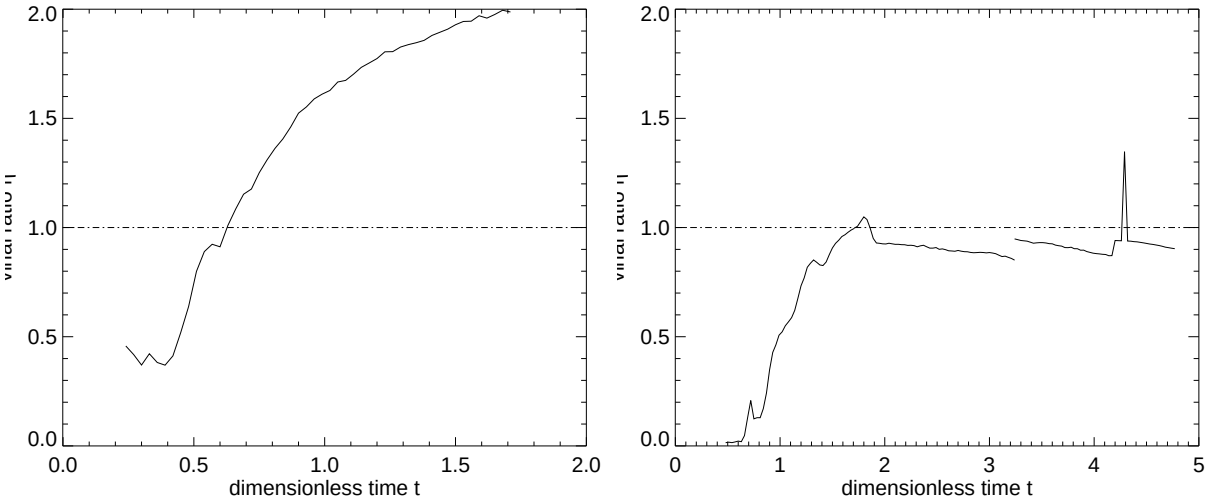

Figure 6.14: *Virial ratio* $\eta = -2\,E_{\rm kin}/E_{\rm pot}$ *of all* bound *N–body particles included in the simulation at the given times.* ***Left:*** *Run L5;* ***Right:*** *Run L10; the unsteadiness comes from the sudden removal of the gas by hand; the single spike is caused by the cluster center finding method (see Section 5.1.1), which failed to converge at that timestep.*

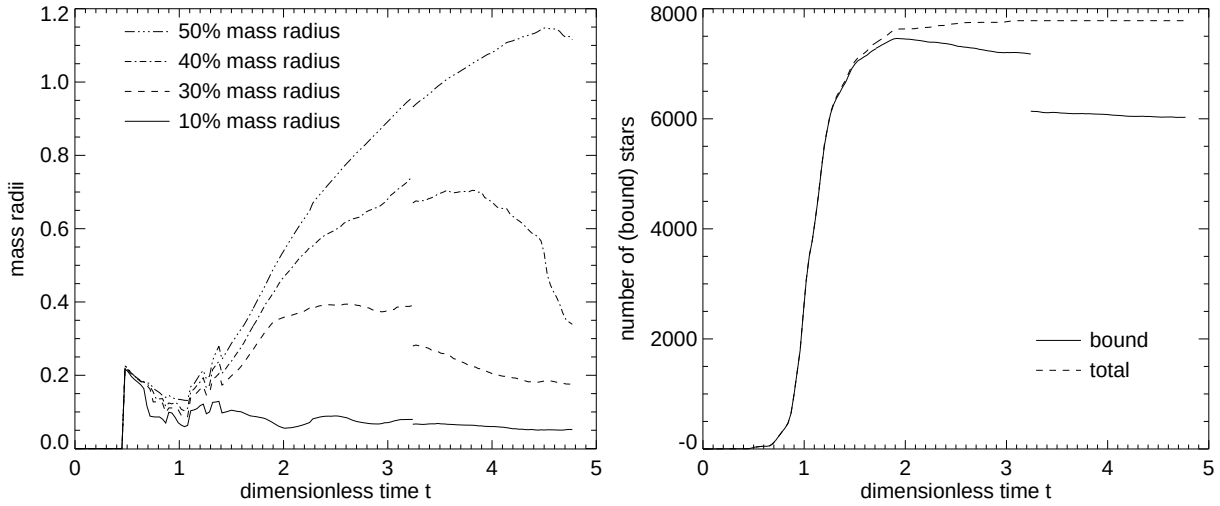

Figure 6.15: *Run L10;* ***Left:*** *Mass radii, considering only bound particles.* ***Right:*** *Total number of stars and number of bound stars. The jump in the curves results from the sudden gas removal by hand at time* $t = 3.24$.

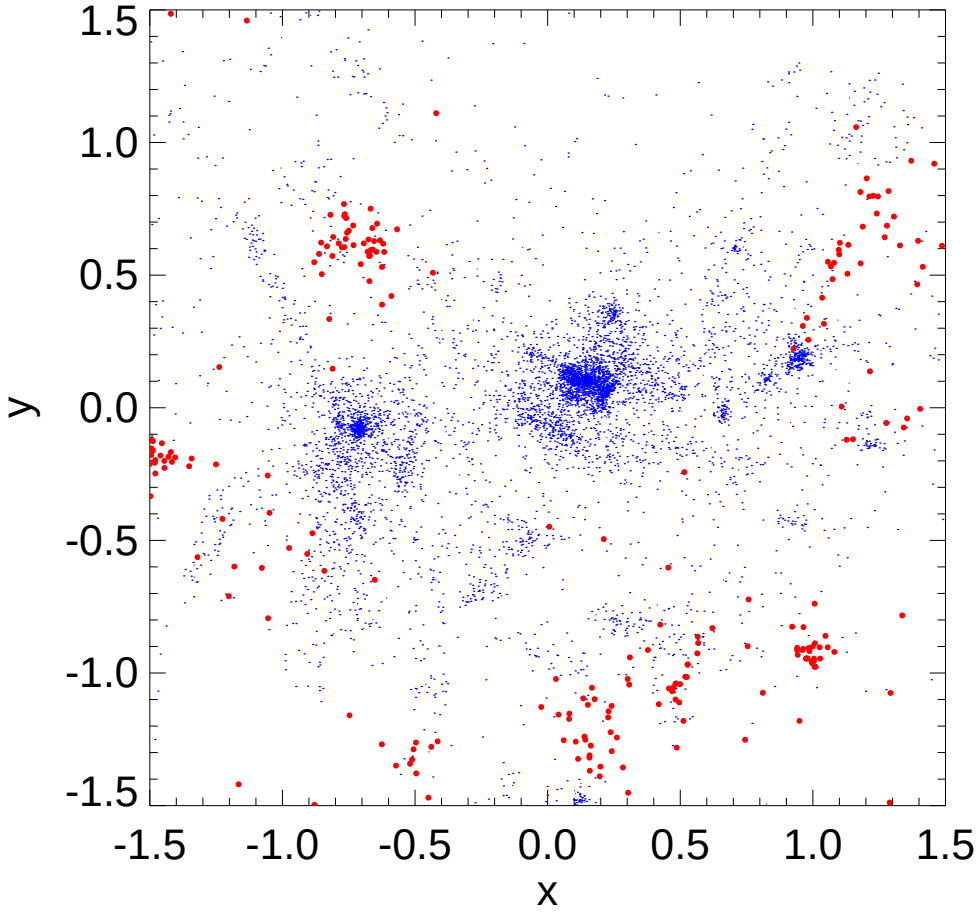

Figure 6.16: *Snapshot of run L10 at time $t = 1.71$. The substructure is clearly visible; stars unbound to the system are marked red.*

the system could survive.

The evolution of only the stellar part in the x–y plane as well as the evolution of the stellar density distribution is shown in Figure 6.17. Also shown is a fitted King profile, using the logarithmic method described in Section 5.3. Even though a lot of substructure can be seen in the first stages of the evolution, King profiles fit well already at time $t = 1.44$. Later, as the cluster splits up into two main parts, the fit gets worse. After the separation, the central cluster in the figures can again be fitted with King profiles. At intermediate timesteps, the young star cluster shows slight enhancements and depressions compared with the King profile, similar to the ones mentioned in Section 5.3, which are probably caused by the substructure of the system. In simulation L10, the gas was removed by hand at time $t = 3.24$ and only the evolution of the stellar part was integrated.

We now look at the evolution of the mass radii of the bound stars and the total number of the stars as well as the number of stars bound in the system (Figure 6.17). The jump in the curves results from the sudden gas removal by hand at time $t = 3.24$. Although most of the gas is already expelled from the center, a certain amount of stars, preferentially at large radii, get

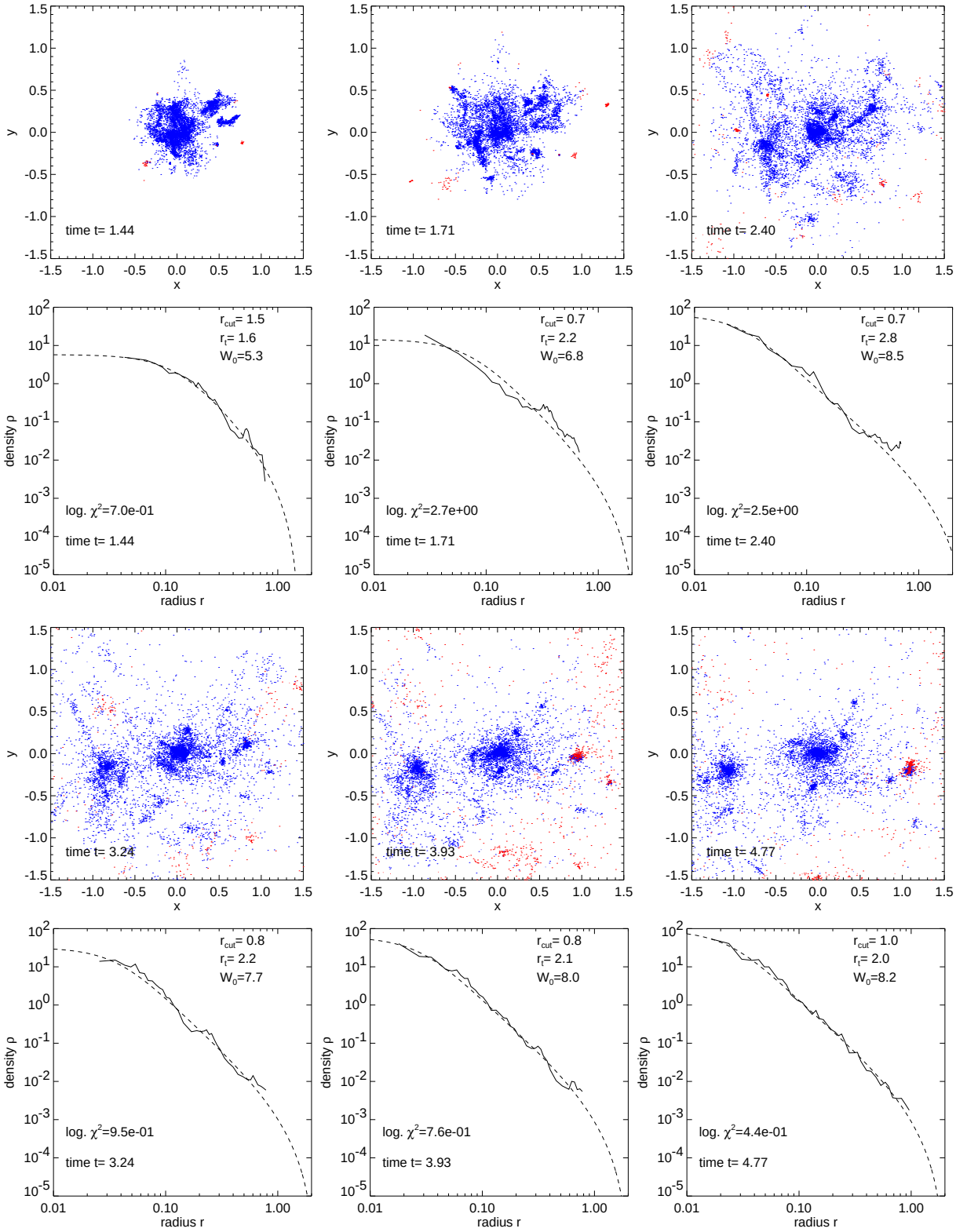

Figure 6.17: *Run L10, the top figures show a time sequence of the projection on the x–y plane, centered on the larger star cluster; the bottom figures show the density distribution at various timesteps with fitted King profiles; density distributions are cut off at an arbitrary radius* $r_{\rm cut}$*; unbound particles are marked red.*

unbound and cause the unsteadiness in the number of bound stars and in the evolution of the mass radii. As star formation sets in, the mass radii decrease, reflecting the overall collapse of the system. At about $t = 1$, the stellar part expands again, due to the high velocities gained during the formation process. The mass radii increase until a maximum is reached and start shrinking again. Looking at the virial ratio of the bound stars for run L10 (Figure 6.14, right), we can see that the system has nearly reached virial equilibrium. The jump in the virial ratio again has its cause in the removal of the gas. On the other hand, the virial ratio of run L5 continues to increase. As we consider only *bound* particles with total energies $E_{\mathrm{tot}} = E_{\mathrm{kin}} + E_{\mathrm{pot}} < 0$, the virial ratio $\eta = -2\,E_{\mathrm{kin}}/E_{\mathrm{pot}}$ or $\eta = -2\,(E_{\mathrm{tot}}/E_{\mathrm{pot}} - 1)$ has a maximum value: In the worst case, $E_{\mathrm{tot}} = 0$ and therefore $\eta \leq +2$. Thus, the asymptotic limit of the virial ratios in Figure 6.14 (left) near the end of the simulation does not mean that the system reaches some sort of equilibrium state – the ratio just stops increasing because more and more particles get unbound (compare Figure 6.6, run L4) and are omitted from the virial ratio determination.

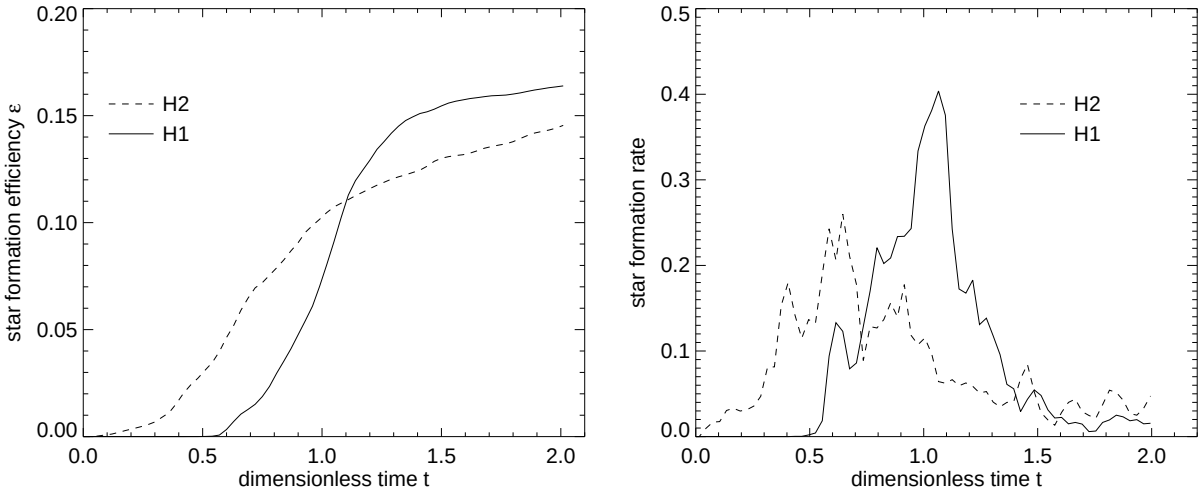

Figure 6.18: *Runs H1 and H2;* ***Left:*** *Star formation efficiencies vs. time;* ***Right:*** *Dimensionless star formation rates; units as in Figure 6.7.*

6.4 Dynamical Evolution of Young Bound Clusters

Now we look at the runs H1 ($P(k) \sim k^{-2}$) and H2 ($P(k) \sim k^{-4}$), which both use 100000 particles instead of the 40000 particles of simulations L1... L14. Both H1 and H2 use the initial conditions and parameters that successfully lead to bound clusters as presented in the last section. After most of the gas has been expelled from the center of the newly-formed star cluster and star formation has stopped, at time $t = 2.0$ the residual gas was completely removed from the simulation by hand and only the stellar part was followed by pure N–body simulations.

Table 6.2 shows that in both runs the final star formation efficiencies are consistent with the ones derived with lesser particles. Due to the different initial power spectra, runs H1 and H2 show different behaviours regarding the time evolution of the efficiencies and rates (Figure 6.18). In the case of H2, the steeper power spectrum leads to earlier star formation compared to H1, ending with a shallower decline. As can be seen, star formation in run H2 was not yet terminated at the time when the residual gas was removed by hand. However, one can expect that the majority of stars has already formed. This behaviour is also reflected in the star formation rate. Additionally, we see that, probably caused by the turbulent nature of the initial gas cloud, star formation is not a smooth process: several smaller bursts manifest themselves with peaks in the star formation rate. As already visible in Figure 6.11 or 6.12, star formation may take place in various parts of the cloud starting at different times.

The time evolution of the energies of the stellar cluster (Figure 6.19) shows, that even after the sudden gas removal by hand, the majority of the stars stays bound (compare also Figure 6.13, run L10). We conclude that in both cases, H1 and H2, bound clusters have formed. The total number stars and the number of bound stars in Figure 6.20 indeed confirm that after the unsteadiness the number of bound stars is approximately constant; only few particles get lost. The virial ratios in Figure 6.21 show that the stellar parts of the simulations tend towards virial equilibrium. Even if the gas outside the cluster does not influence its dynamics, it contributes to the potential energy. Thus, the sudden gas removal by hand decreases the potential well, reflected in a jump in the virial ratios. As we are interested in the boundness, which depends

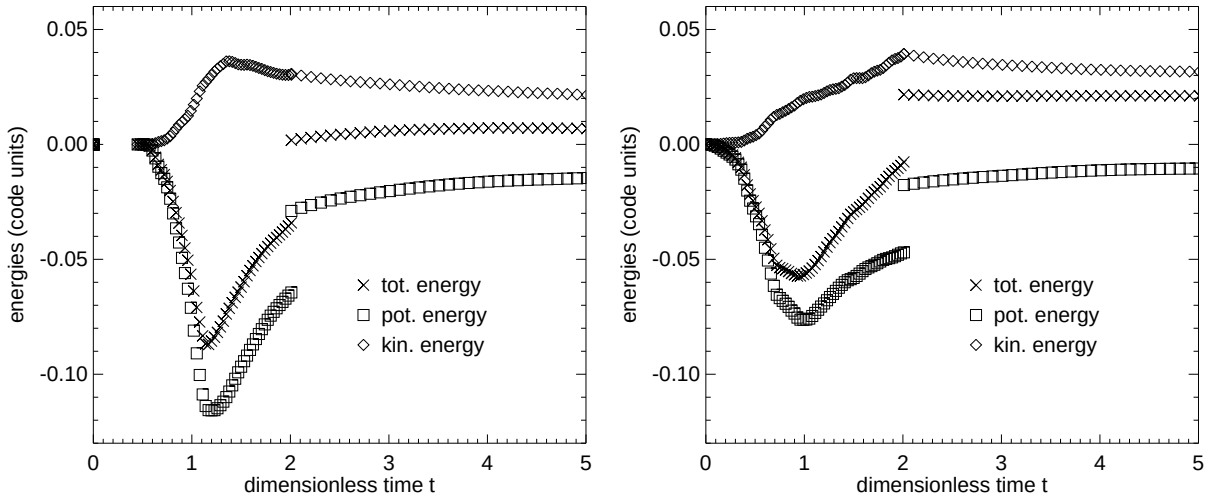

Figure 6.19: *Kinetic, potential and total energy of all N–body particles included in the simulation at the given times.* ***Left:*** *Run H1;* ***Right:*** *Run H2; the unsteadiness comes from the sudden removal of the gas by hand.*

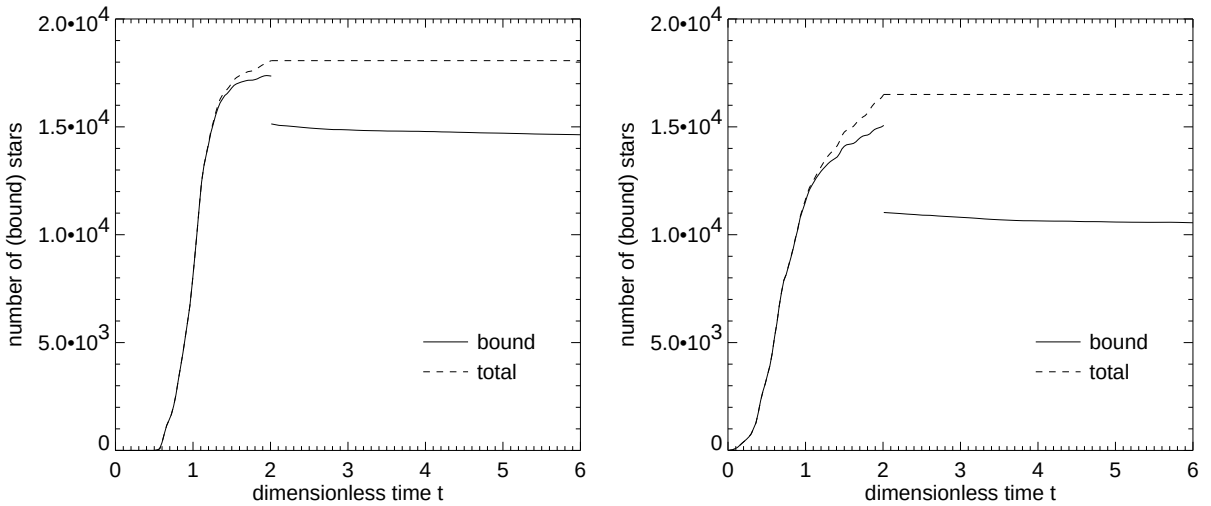

Figure 6.20: *Total number of stars and number of bound stars;* ***Left:*** *Run H1;* ***Right:*** *Run H2; the unsteadiness comes from the sudden removal of the gas by hand.*

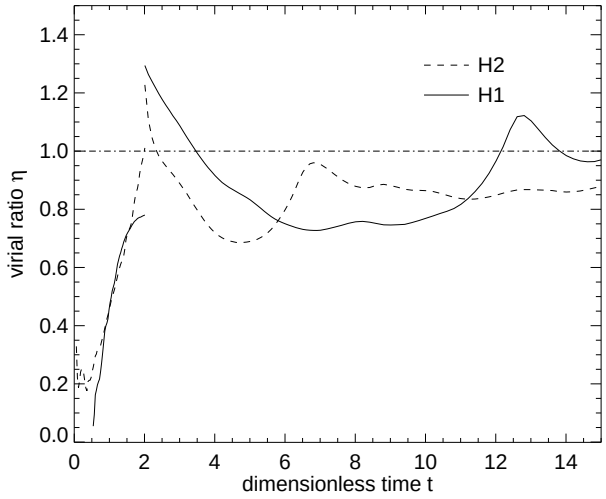

Figure 6.21: *Virial ratios vs. time for runs H1 and H2 only considering bound particles.*

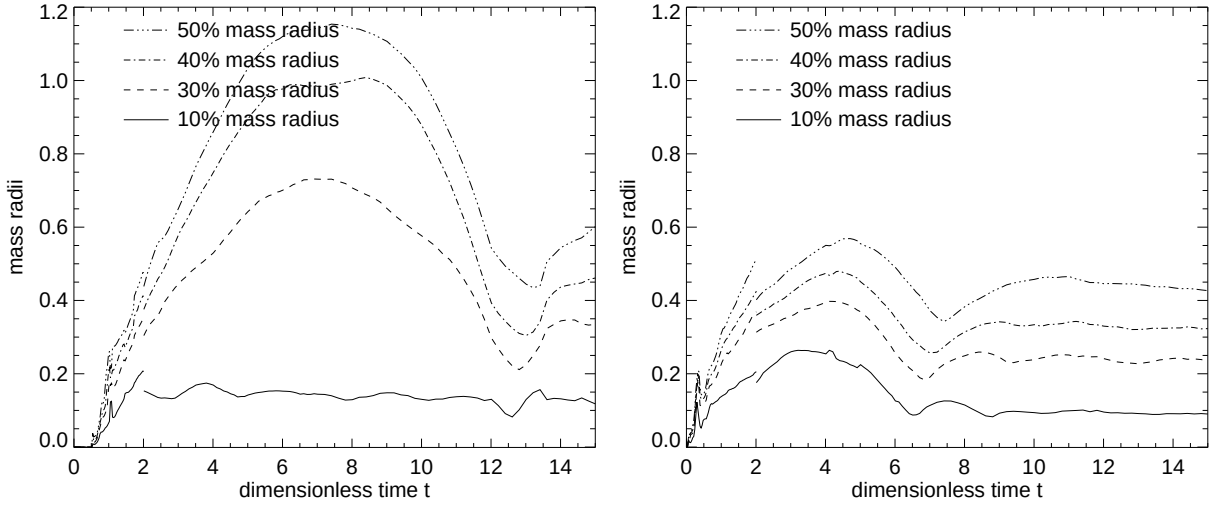

Figure 6.22: *Mass radii, considering only bound particles;* ***Left:*** *Run H1;* ***Right:*** *Run H2.*

on the internal binding energy of the cluster only, removing the gas completely is necessary. A slower expulsion of the gas would be less severe and more stars might stay bound; also the final spatial extensions of the cluster could be decreased, as shown in Figure 5.3 for various timescales.

The mass radii in Figure 6.22 show that the systems undergo heavy relaxation processes during the evolution. The dynamical timescales at time $t = 7$ in code units are about $t_d = 9.2$ and $t_d = 2.3$ for the runs H1 and H2, respectively. Thus, compared to H1, system H2 needs less time to relax until the mass radii are approximately constant.

In the case of run H1, one can also detect stellar groups that, although unbound to the system, form loose associations travelling outwards together, e.g. the "red association" in Figure 6.24, top left panel, at coordinates $x = -1.8$ and $y = +1.1$. An enlarged image is given in Figure 6.23 (left panel). At the end of the simulation, this subcluster is well beyond the tidal radius of the large central cluster and has a mass of about 10% of the large one. To compute the evolution

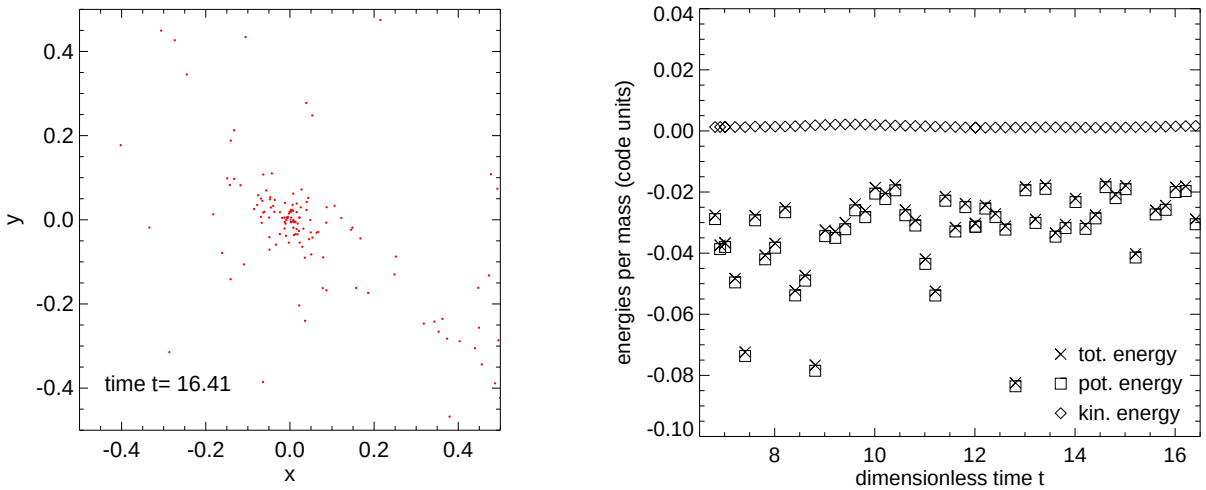

Figure 6.23: *Properties of the small "red subcluster" found in Figure 6.24, top left panel, at coordinates $x = -1.8$ and $y = +1.1$.* ***Left:*** *Spatial distribution, centered on the subcluster, projected onto the x–y plane.* ***Right:*** *Evolution of specific energies.*

of the energies (Figure 6.23, right panel) all particles inside a radius $r = 0.5$ with regard to the subcluster center were included. The negative total energy shows that the small system is bound. However, computing the virial ratio from these energies shows that the system is not in equilibrium. Additionally, the subclusters consist of only about 100 particles, which gives a poor numerical resolution. In reality, it might evaporate fast due to two-body encounters.

Goodwin (1998) was concerned about how much substructure a newly-formed young globular cluster may have at maximum. He argued that after several 10 Mio years the new clusters must have relaxed – all the substructure must have gone to resemble actual observed young globulars. Looking at our simulations, we see that early in its evolution, the cluster is unspherical and has lots of substructures or clumps. These deformations obviously come from the initial properties of the turbulent gas cloud: The shallower power spectrum results in more individual clumps (Figure 6.24). In the following evolution, the clumps will interact with each other and / or merge. Observations of molecular clouds give hints that the steeper power spectrum $P(k) \sim k^{-4}$ is preferred by nature – therefore simulation H2, which shows less substructure, might be more likely and also explains the properties of young clusters more easily. However, it must be noted that at the end of the simulation also run H2 still is not really relaxed and shows substructures.

Figure 6.25 shows the radial stellar density evolution of the cluster of run H2. The cut off radius was set such that a continuous decrease of the radial density was guaranteed. Beyond the cut off radius, the density distribution is governed by disturbances due to outwards travelling stellar associations unbound to the system and stars whose dynamical timescales are large and which have not yet relaxed. The used cut-off radius matches the region shown in Figure 6.24. The fitted King profile with the scaled central potential $W_0 = 7.2$ at time $t = 17$, which corresponds to a central concentration $c = 1.6$, is well in the range of the globulars observed today in our Milky Way (see Figure 2.2). Further simulations will be needed to determine what the central concentration of the new cluster depends on or where the spread in the observed concentrations comes from, respectively.

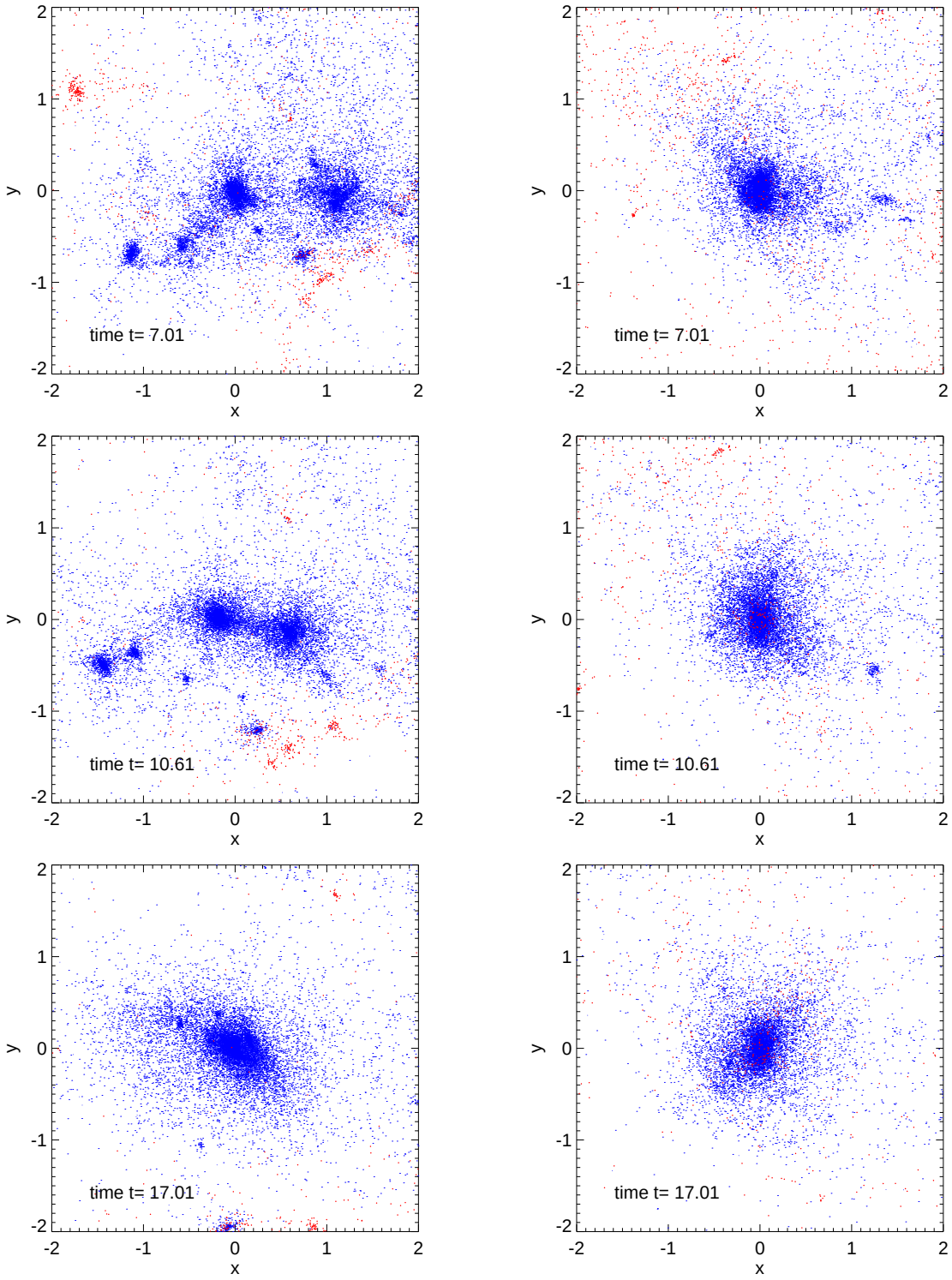

Figure 6.24: *Snapshots of Run H1 (left column) and H2 (right column) early in the evolution until the different clumps merge; stars unbound to the system are marked red. The steeper power spectrum of simulation H2, where most power is in long wavelength modes, leads to one major clump early in the evolution, whereas H1, using the shallow power spectrum, leads to several clumps at first.*

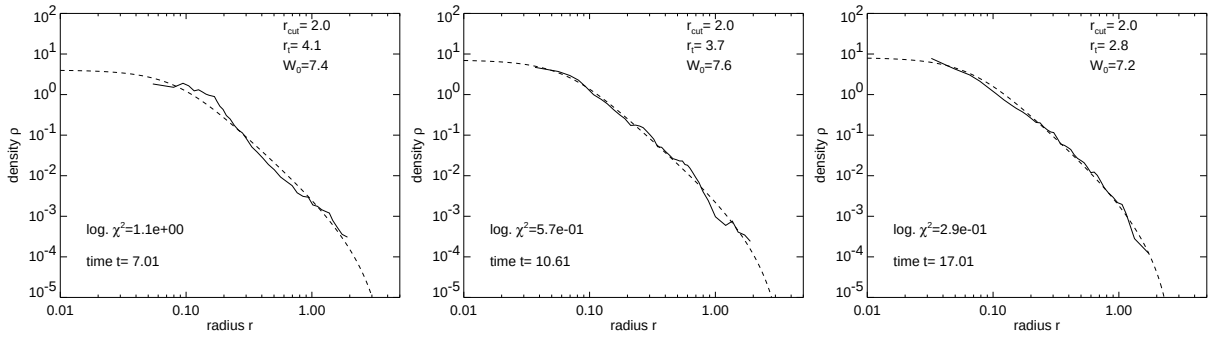

Figure 6.25: *Density distribution and fitted King profile for the timesteps shown in Figure 6.24, run H2.*

Observations of young clusters in the Large Magellanic Cloud by Elson (1991) show that preferentially the youngest clusters have typical "humps" and "dips" in the radial densities compared with fitted King profiles. The radial density given in Figure 6.25 (run H2) gives about the same density range as the observations shown by Elson (1991). In the first shown timestep, deviations from the King profile can be clearly seen. However, these are only transient features and have already disappeared in the following snapshots. One explanation for these departures from the relaxed profile may be merging subclusters (Elson 1991) like in our run H1. This theory is corroborated by the complex dynamics of young cluster systems: A large amount of close pairs of young clusters have been observed in the Large Magellanic Cloud. Dieball, Grebel & Theis (2000) and Dieball & Grebel (2000) give evidence for coeval double clusters in the Large Magellanic Cloud which might have formed from one single giant molecular cloud. Bhatia & MacGillivray (1988) even observed a possible merger of young clusters (Figure 6.26). But also our less sophisticated gas expulsion simulations in Section 5.3 show similar deviations from King profiles and might explain the deviations as relics of the gas expulsion process (see also Goodwin, Pearce & Thomas 2001). Shortly after the loss of stars due to the decreasing potential the cluster relaxes again.

The compatibility with observations of course does not proof that the model used here is valid. The scenario in which merging subcondensations form the young globular cluster after relaxation is very attractive, but would favor the probably unlikely shallower power spectrum. One must also mention that the fit of the King profile to the final cluster of the simulations is strongly influenced by the assumed cut-off radius. Fits with lower cut-off radii lead to lower scaled potentials W_0. Thus, if outer parts of the new clusters are stripped off, maybe by tidal interactions with the host galaxies, more centrally concentrated clusters might remain. On the other hand, mass loss due to stellar evolution, which is not included in the presented models, could lead to an expansion of the cluster core.

Figure 6.27 shows the asymmetric structure of the column densities of the gas expelled from the central stellar cluster. Structures on various spatial scales show up. Clearly visible are shell-like structures which are travelling outwards. Comparing improved simulations with young star forming regions, e.g. Figure 2.4, might give hints to determine the age of the clusters, independent of other methods.

Summing up, we derive a picture where globular clusters form in the dense central regions of giant molecular clouds. Even if the global star formation efficiency is low, high local efficiencies

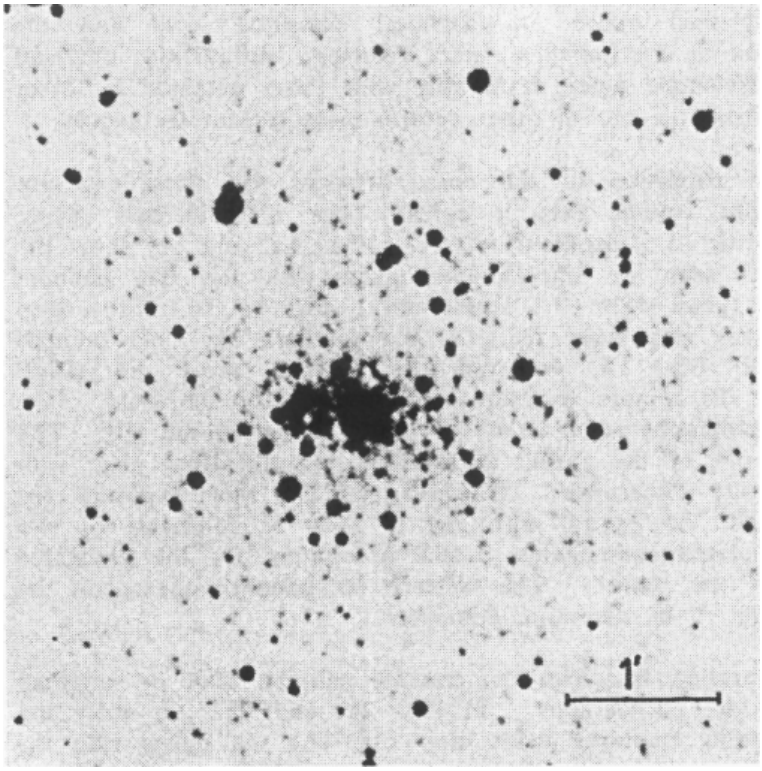

Figure 6.26: *NGC 2214, optical image from Bhatia & MacGillivray (1988); the core seems to be consisting of two components.*

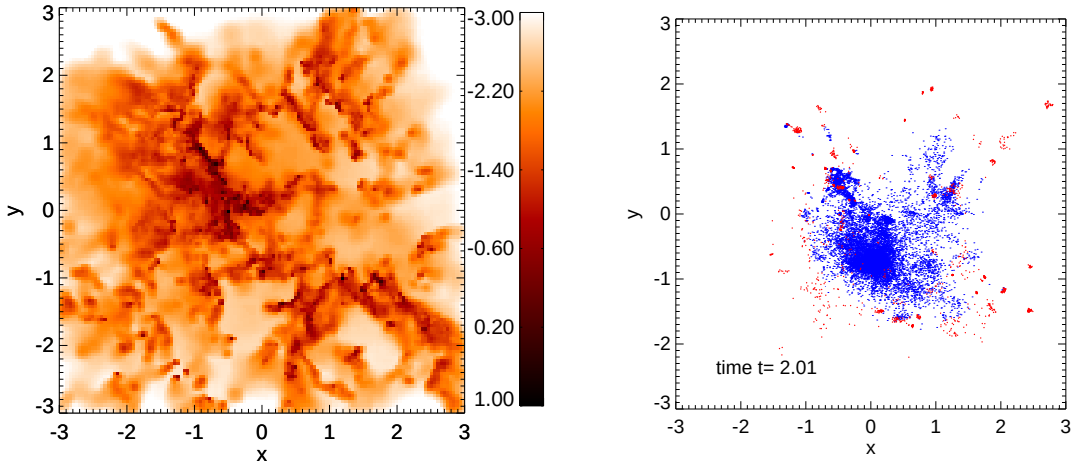

Figure 6.27: *Run H2. Logarithmic column densities (left) and stars (right) at time* $t = 2.01$. *Unbound stars are marked red.*

can lead to bound clusters. It has to be checked whether the stellar subcondensations which form first due to the turbulent motion merge and relax fast enough so that the resulting clusters match the smooth radial density distributions of observed young mass-rich clusters. This picture would lead to globular cluster systems where at least a fraction of the initial turbulent kinetic energy of the progenitor clouds is conserved in the individual clusters or associations. One would also have to check if the star clusters of this simulation are able to survive in the tidal field of the host galaxy for times comparable to the ages of old globular clusters.

6.5 Collisions of Molecular Clouds

It has long been speculated that globular cluster formation might be triggered by molecular cloud collisions in the halo of protogalaxies or in interacting or merging galaxies. Ashman & Zepf (1992) give an extensive review of evidences for young globular cluster formation in external galaxies which at the moment undergo such violent events. Ashman & Zepf (2001) also stress that molecular clouds in such high pressure environment show the right masses and spatial extensions compared to observed globulars.

In their picture, the constant specific frequency of globulars around spirals (Harris 1991) is caused by similar mass spectra of gas clumps that have been able to form globulars around protospirals. It is suggested that at least some ellipticals form by mergers of spiral galaxies (Naab & Burkert 2001). The observed excess in the specific frequency around ellipticals can then be explained by forming a new population of clusters during the merging process of two spirals. Different populations of globulars within one system have been detected by the bimodal metallicity distributions of the clusters in our and other galaxies (see Ashman & Zepf (1999) and references therein). The bimodality can be explained by globular cluster subsystems forming at different times: Younger systems form in a more metal-rich environment compared to that of the old population.

Collisions of molecular clouds have been studied by various people as a possible mechanism for triggering efficient star formation, needed for the formation of globular clusters. Fujimoto & Kumai (1997) investigate globular cluster formation by cloud collisions in the high-velocity random motion of galactic halos. They explain the large number of young double clusters by oblique cloud collisions which can split up the clumps into two objects. However, our simulations of the last section show that stellar subcondensations may form from turbulent molecular clouds without further assumptions.

Whereas most work was restricted to homogeneous or spherical symmetric clouds, Kimura & Tosa (1996) look at collisions of clumpy clouds. They show that small clouds are even able to pass through larger clouds without serious damage – such behaviour can not show up in the homogeneous case. However, if the clouds are comparable in size, shocks build up and clumps with masses greater than the Jeans mass are formed, probably leading to triggered star formation.

For our initial setup of the merger simulations, we use two identical single cloud configurations. At the start, the clouds nearly touch each other, the relative velocity is about $v' = 4.0 = 50\, a'_T$, where $a'_T = 0.08$ is the mean isothermal sound speed in code units. With our usual scales, the relative velocity is $v = 12\,\mathrm{km/s}$, which is still less than the relative cloud velocities of $100\,\mathrm{km/s}$ or more observed in the Large Magellanic Cloud and other galaxies (Kumai, Basu & Fujimoto 1993). The lack of these latter high velocities in our Galaxy might explain the absence of young globulars.

The time evolution of star formation efficiencies in our merger simulation M1 (Figure 6.28, left) shows that by collisions of clouds star formation can be considerably increased. Additionally, by triggering star formation this way, the overall time needed until all the gas is transformed into stars or has been expelled due to feedback, respectively, decreases. Comparing the star formation rates of the single cloud and the merger (Figure 6.28, right) shows that at late times star formation has already stopped in the merger while at the same time some stars still form in the single cloud case.

Figure 6.29 shows the time evolution of the column density and the stellar part. Stellar

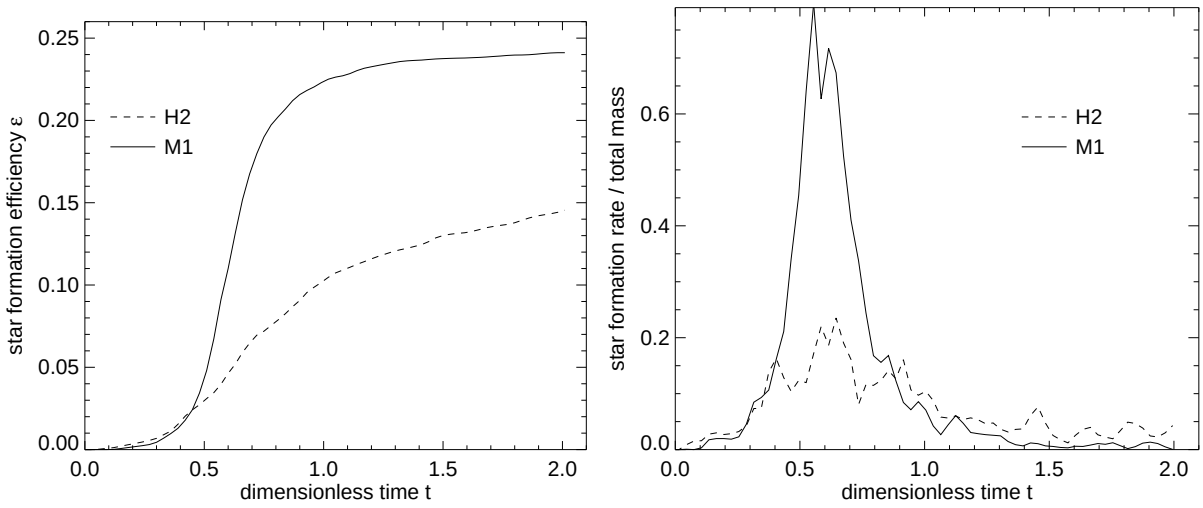

Figure 6.28: *Cloud collision M1 compared to the single cloud H2;* ***Left:*** *Star formation efficiencies vs. time;* ***Right:*** *Star formation rates normalized to the total initial gas mass of the system*

structures which form due to the collapse of the cloud, independent of the merging process, have high speeds and cross the central stellar clump which forms by the collision. They are unbound to the system, but may be observed as loose associations. This can be seen in the detailed diagrams of the stellar cluster evolution in Figure 6.30: A large, unbound (red) association of stars leaves the system to the left and expands. Of course the bound star clumps will undergo the same merging processes as the ones in the last section.

Summarizing, we can see that collisions of molecular clouds in our model can increase the star formation efficiency. The peak star formation rate is even four times higher compared to the single cloud configuration. As these are still low resolution runs, more extensive simulations, also with higher collision velocities, will be needed to test the model. Particularly, heating and cooling processes may play an important role in the shocked regions (Kimura & Tosa 1996).

Additionally, oblique collisions will be much more likely. They yield shear and rotation to the merger and may disrupt the clouds (Fujimoto & Kumai 1997). Especially in the case of clumpy clouds, non head-on collisions might give considerable decreased star formation rates, as not enough clumps are able to hit each other during the collision.

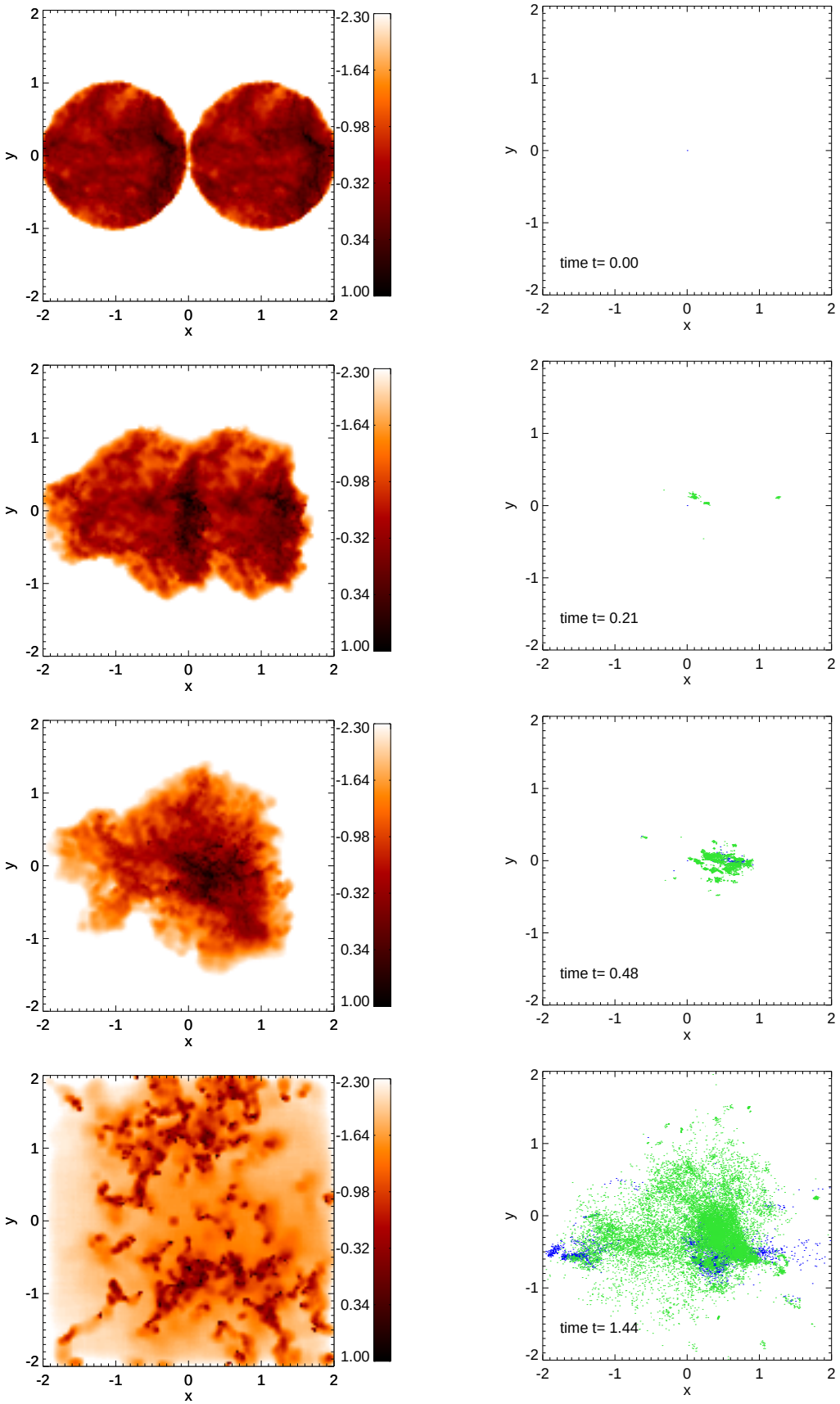

Figure 6.29: *Collision run M1. Logarithmic column densities (left) and stars (right) for various time steps. New stars with respect to the last shown timestep are marked green.*

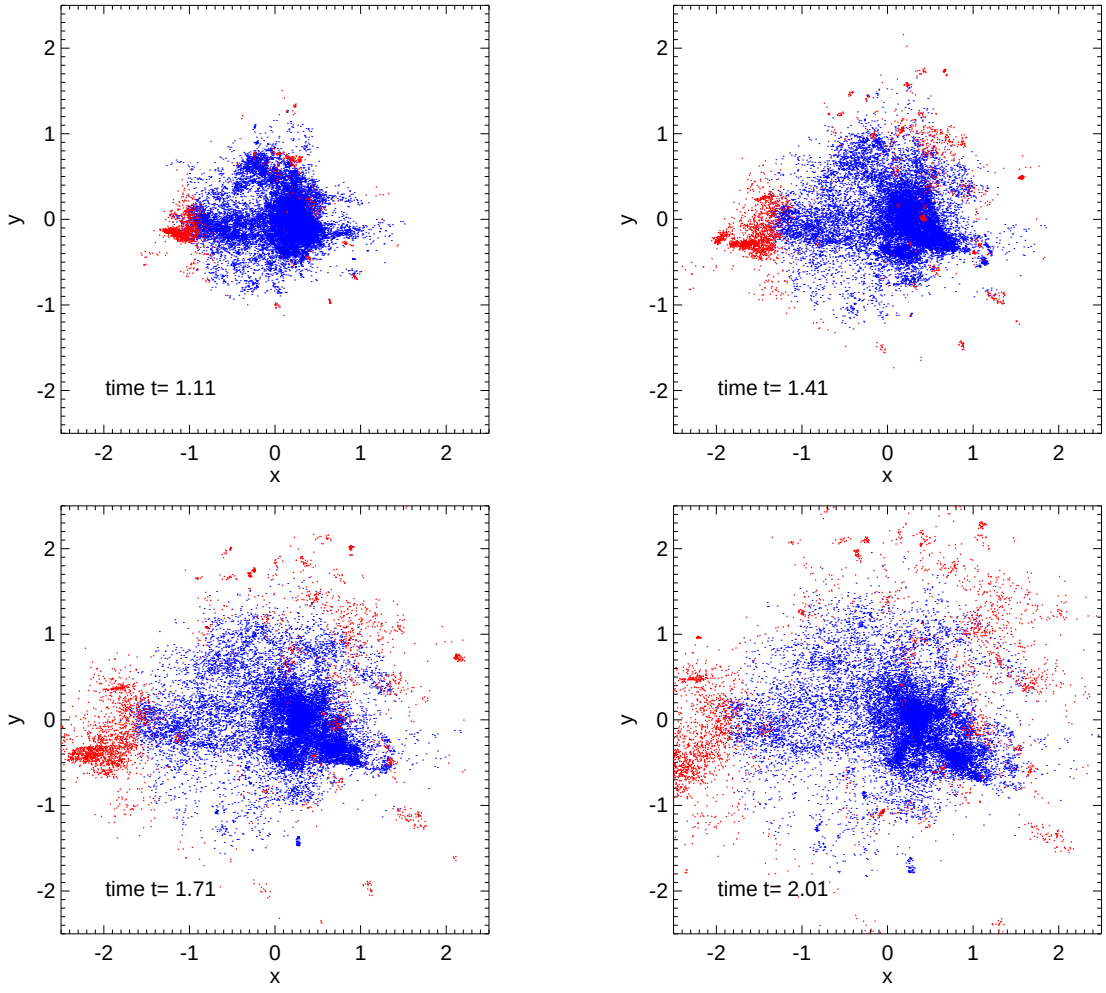

Figure 6.30: *Snapshots of run M1; stars unbound to the system are marked red.*

6.6 Star Formation and Feedback – Caveats of the Implementation

After the presentation of the obtained results in the last section, we now will have a cautious look at the implementation of star formation and feedback in the code.

First, each simulation using SPH and the idealized star formation description used in this thesis at some time will violate the strict resolution limit of Bate & Burkert (1997), which mainly is based on the Jeans limit (see also Section 3.5.2). This is even worsened by applying global density thresholds. In our simulations we are mainly interested in the dynamics and structure of the forming stellar system and not in the detailed gas dynamics on small scales at late epochs. Our approach therefore is justifiable.

But turbulence on small scales could have an important influence on star formation and in the worst case might destroy the dense cores, which in our picture would form stars right away. Our treatment thus may overestimate the star formation efficiency. In addition, regarding the actual resolution, we of course cannot make any statements about properties of individual stars, like the initial mass function, binary fraction or competitive accretion processes.

Another important point is the interplay between the numerical timestep and the implementation of star formation and feedback. In the worst case, a high density SPH particle, which fulfills all the criteria, is transformed into a stellar particle and heats up immediately all its 50 neighbours. "Immediately" means at least faster than the timesteps of these neighbours. However, if we can assume that the density contrasts over one smoothing length are not too strong, neighbouring particles will be on the same or similar timestep levels. Nonetheless, if this heating is sufficient, none of these neighbours will be able to form stars itself – the star formation may be underestimated. Figures 6.31 and 6.32 show on the right panels the actual specific thermal energy distribution of the SPH particles at the last timestep. In the same panel the specific thermal energies of the progenitor SPH particles for each N–body particle are plotted. A large fraction of the gas particles has been heated up to the temperature limit $T = 10.0$ (code units). Only gas particles with specific temperatures less than about $T = 0.5$ were able to form N–bodies. However, this means that star formation is not shut off immediately and at least some neighbours of a star may form stars subsequently, even if they have been heated a little. Also the time delay, which was used in this simulations, circumvents the problem of artificially stopping star formation among neighbours by giving them some additional time for transforming into stars.

From Figures 6.31 and 6.32 we can take the total amount of thermal energy put into the gas, if we neglect the thermal energy of the gas that formed stars. In the case of run H2, the thermal energy increases (code units) from $E'_{\mathrm{thermal}} = 0.01$ to $E'_{\mathrm{thermal}} = 2.0$. Using the units from Section 4.4 and the scale factors from Table 3.1, this corresponds to an energy change of $\Delta E_{\mathrm{thermal}} = 3.4 \cdot 10^{42}\mathrm{J}$ or a rate $\Delta \dot{E}_{\mathrm{thermal}} = 3.3 \cdot 10^{27}\mathrm{J/s}$ over the simulation time. This roughly matches the values that were estimated in Section 4.4.

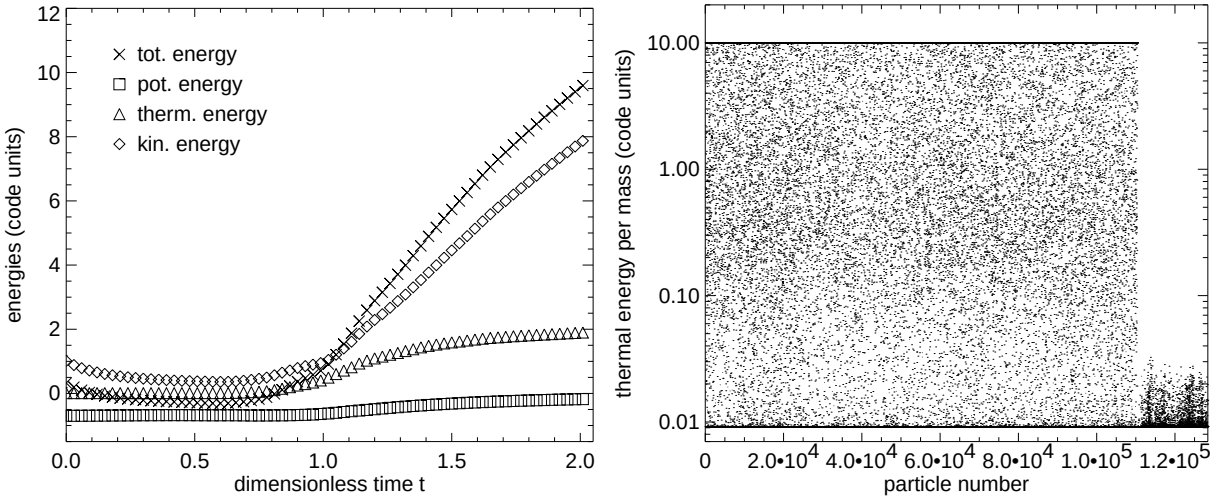

Figure 6.31: *Run H1, last timestep;* ***Left:*** *Time evolution of kinetic, potential, thermal and total energies of the gas;* ***Right:*** *Distribution of thermal energies among SPH particles at the last timestep (broad distributed dots on the left side) and of the progenitors of the N–bodies at the time of their formation (dots on right side).*

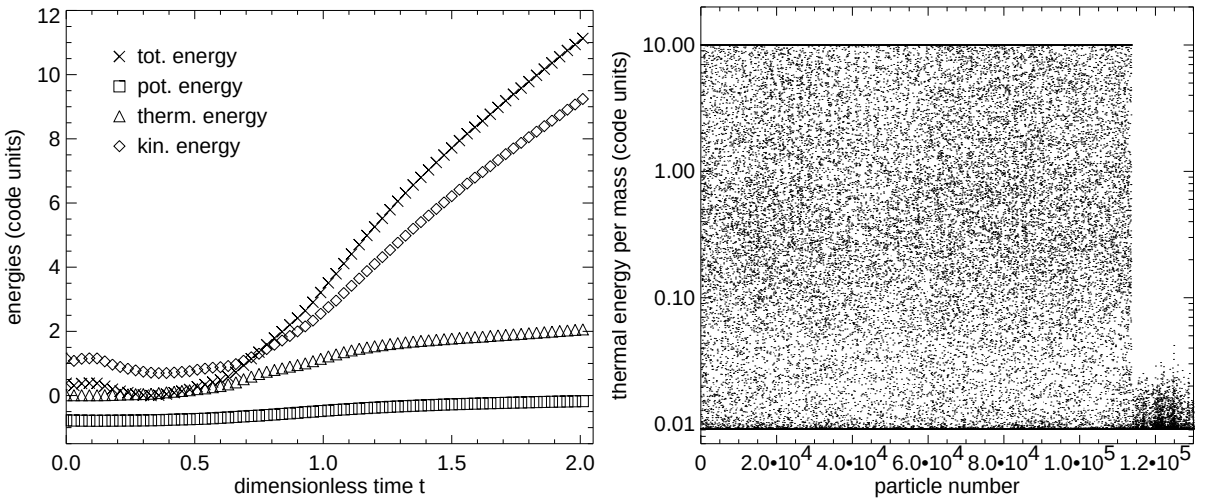

Figure 6.32: *Run H2, last timestep;* ***Left:*** *Time evolution of kinetic, potential, thermal and total energies of the gas;* ***Right:*** *Distribution of thermal energies among SPH particles at the last timestep (broad distributed dots on the left side) and of the progenitors of the N–bodies at the time of their formation (dots on right side).*

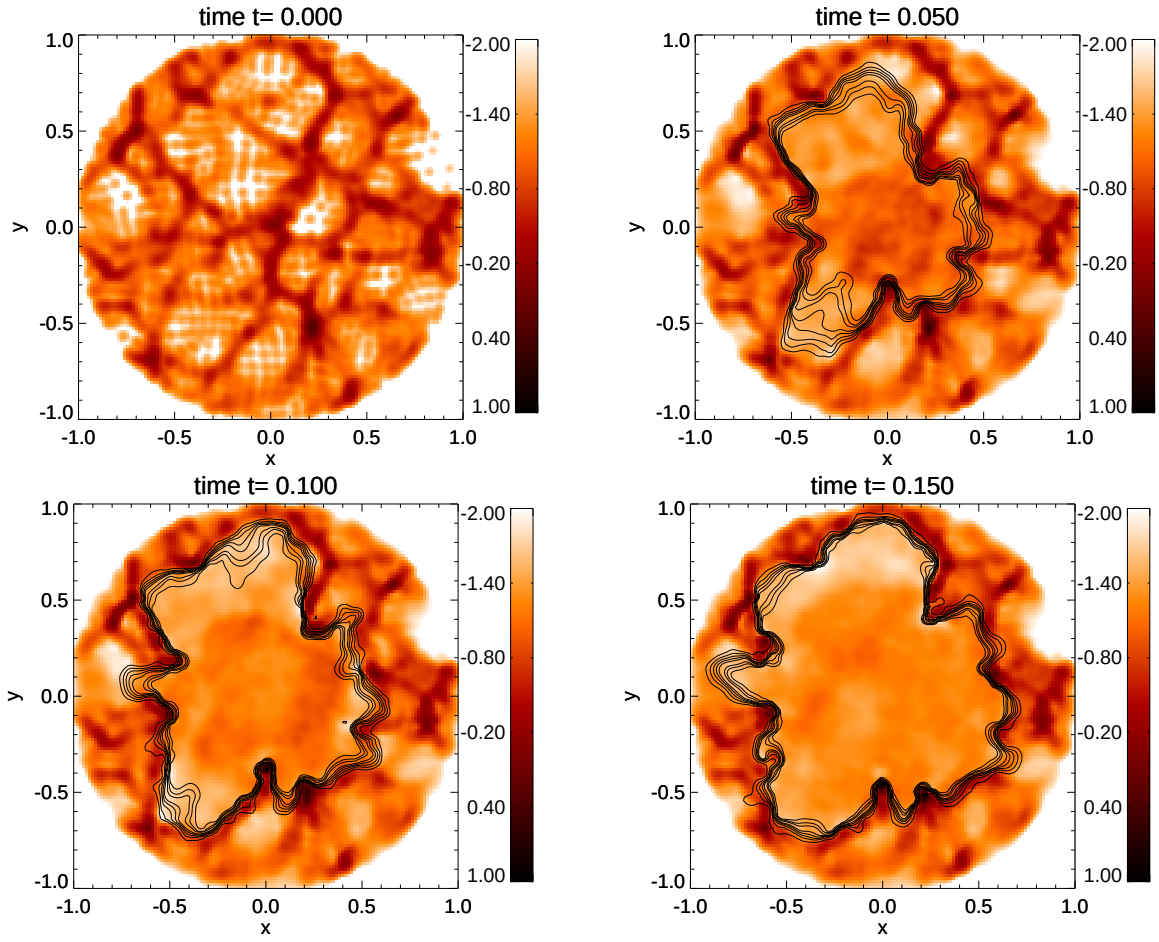

Figure 6.33: *Example run showing ionization due to a point source in the center of a turbulent molecular cloud with radius* 50 pc *and mass* $10^5\,M_\odot$*; flux of ionizing photons* $5 \cdot 10^{48}\,\mathrm{s}^{-1}$*; shown is the density in the x–z plane and contours giving the ionization fraction from 0.1 to 1.0 in steps of 0.1.*

6.7 Towards an Improved Implementation of Stellar Feedback

A first improvement regarding the description of energy feedback is not to heat the neighbours of all the gas particles, but only to heat the neighbours of *selected* OB stars. However, we then have to decide for a radius inside which we heat up the particles. This could be e.g. the Strömgren radius of the star, determined by the density at the position of the newly-formed star. But this radius may be severely underestimated if the density drops of on small scales beyond the spatial region around the star.

A vast improvement can be achieved by directly following the ionization. Kessel-Deynet & Burkert (2000) implemented ionization into SPH using a ray tracing method. Figure 6.33 shows the evolution of a turbulent molecular cloud with an embedded point like ionizing source located at the center using this code. The developing shell is not at all symmetric – the ionization front travels faster in low density regions. Instabilities might occur which may induce star formation in the non-ionized parts of the cloud. A combination of this code with star formation and energy feedback will give valuable new insights into the evolution of star forming regions.

Chapter 7

Summary

This thesis concentrated on the basic conditions that must be fulfilled to form massive bound star clusters like the globular clusters we see today in the halo of our and other galaxies or like the young mass-rich clusters observed in star forming regions of external galaxies. In this last section, the main statements are summarized and a brief outlook regarding improvements and possible applications of the presented investigations is given.

7.1 Conclusions

In a first step we investigated the influence of residual gas expulsion on the dynamical evolution of star forming regions: Shortly after the formation of stars from turbulent molecular clouds, the cluster consists of a bound system of stars and gas. The gas will leave the system after a few dynamical timescales due to the feedback of young massive stars, like ionizing radiation, stellar winds or supernova explosions. This terminates the star formation epoch and reduces the binding energy of the cluster and can unbind the stellar system.

To simulate the gas expulsion and early evolution of young star forming regions we performed numerical N–body calculations, where the stars are represented by collisionless, equal mass N–body particles. To model the ejection of the residual gas we used a time variable external potential that linearly decreases with time. Initially the stars are in virial equilibrium within the potential of the stars and the gas. Also combined N–body & SPH (smoothed particle hydrodynamic) simulations were performed for a more self-consistent description of the gas expulsion process.

Bound clusters can only sustain the expulsion of the residual gas if the star formation efficiency is high enough: The results showed that in the case of instantaneous gas expulsion, clusters with star formation efficiencies greater than $\epsilon = 0.45$ can keep more than 50% of the initial stars. Clusters with star formation efficiencies less than $\epsilon = 0.40$ are dissolved. Gas expulsion timescales which are several times longer than the dynamical timescale of the star cluster can decrease the needed efficiency to sustain bound clusters considerably. But even these efficiencies are greater than the typical observed star formation efficiencies in our Galaxy of less than 10% . Thus, the formation of gravitationally bound open clusters and globular clusters is yet unsolved.

However, it is not clear from the outset if the assumption of virial equilibrium after the stars have formed is correct. Models with stars having an initial zero velocity dispersion lead to a compaction of the cluster and can explain bound systems even in low star formation efficiency

regions: For efficiencies as low as $\epsilon = 0.15$ more than 80% of the stars stay bound. For follow-up investigations it is essential to know the velocity dispersion of newly-born stars in clusters, determined by observations and / or numerical simulations.

This problem directly leads to the second part of this thesis: The formation of a bound stellar system is a race between efficient star formation and feedback processes leading to an expulsion of the residual gas. The results regarding the idealized description of the gas expulsion process show that strict conditions are necessary to form massive bound stellar clusters. How can these circumstances be achieved during the formation process of the cluster ?

SPH simulations including idealized star formation and feedback descriptions due to high mass stars were performed. Stars are allowed to form where the density exceeds the local Jeans mass and a certain global density criterion. The feedback is done by heating the interstellar medium surrounding the stars by an amount corresponding to the energy input of ionization or stellar winds.

We chose our initial conditions to match the properties of giant turbulent molecular clouds, which are generally believed to be the progenitors of massive star clusters like globular clusters. The initial power spectra for the velocities were $P(k) \sim k^{-2}$ and $\sim k^{-4}$. Evolution of the systems without self-gravitation and star formation gives the initial models with self-consistent density and velocity distributions.

The simulations of the collapsing and fragmenting molecular cloud show that the star formation efficiency depends strongly on the time delay between the formation of stars, and the time when feedback from the stars begins. The later the feedback sets in, the more stars may form. This delay might be caused by the finite formation time of the stars and could be enhanced by massive stars forming late in the evolution of the cluster. Next, the occurrence of bound systems heavily depends on the chosen global density criterion, which essentially determines when stars form during the collapse of the host molecular cloud. The later star formation starts, the more compact is the resulting star cluster and thus greater the probability of staying bound after gas expulsion. The goal was to present one possibility of forming bound star clusters. Comparison with observations and more detailed numerical models must tell whether the made assumptions for the initial conditions and simulation parameters are reasonable.

In the presented simulations, the main properties of a cluster-forming molecular cloud, such as star formation efficiencies and rates, interaction with the residual gas, compactness and boundness of the newly-born cluster and their dependencies on the initial conditions could be investigated. However, the resolution is not high enough to make statements about individual stars. In addition, the star formation efficiency could be vastly influenced by turbulent perturbations in the molecular clouds on scales that are not resolved.

Elmegreen (2000) argues that due to the short formation time of the cluster, protostar interactions do not play a role in determining the average initial stellar mass function. Contrary, the initial mass function would be caused primarily by the initial cloud structure. On the other hand, Bonnell et al. (2001) and Bonnell et al. (2001) have shown that competitive accretion among the protostars can influence the initial mass function. They find that the accretion rate primarily depends on the local gas density. Observations of the young double cluster NGC 1850 in the Large Magellanic Cloud by Gilmozzi et al. (1994) (Figure 2.4) suggest that the two clusters formed at distinct times with different initial mass functions. In Chapter 6.3 we showed that if bound star clusters are formed, they show strong spatial structures, connected to the initial molecular cloud density distribution.

7.2 Outlook

Simulations of the fragmentation of turbulent molecular clouds with SPH down to the scale of the protostars were done by Klessen & Burkert (2000) and Klessen & Burkert (2001). Only with this resolution or higher can one begin to draw conclusions about the stellar initial mass function, accretion processes or the binary fraction. Using up to 500000 SPH particles, these computations were limited to the simulation of about 60 stellar cores – resembling open clusters or associations. However, without feedback processes, nearly all the mass of the initial gas cloud is accreted onto the stellar objects at the end of the simulation. Bate, Bonnell & Bromm (2001) also have performed simulations of the fragmentation of a molecular cloud. In these calculations, the resolution is high enough to resolve individual binary systems and circumstellar discs. They use a polytropic equation of state to model the heating of collapsing gas at high densities but do not include any other feedback. In the presented simulations, a higher resolution would be needed for resolving the properties of individual stars. Combining the high-resolution simulations mentioned above with feedback processes will lead to new valuable insights.

In addition, as energy feedback tremendously influences star formation, a more physical description of the feedback processes must be achieved. Star formation in ionized regions will be stopped abruptly. One approach is to include ionizing radiation like proposed by Kessel-Deynet & Burkert (2000) into the code. Also the dynamics of stellar winds can dominate the vicinity of massive OB associations (Abbott 1982). Goodwin et al. (2000) examine the effects of expanding supernovae on the surrounding medium. These complex dynamic interactions need high resolutions to resolve shock fronts travelling into the unperturbed surrounding medium. Interactions of these shock fronts could lead to propagating star formation (Kimura & Tosa 1993, Chappell & Scalo 2001). Further improvements can be achieved by the inclusion of radiative transfer into SPH using the flux-limited diffusion approximation which is developed by Lang, Kessel-Deynet & Burkert (2001).

In recent simulations of galaxy formation (Katz 1992, Gerritsen & Icke 1997, Thacker & Couchman 2000, Springel 2000) and globular cluster formation (Nakasato, Mori & Ken'ichi 2000), star formation and energy feedback can only be done empirically with the idealized descriptions similar to the one used in this thesis. An improved knowledge of the feedback processes and star formation on small scales of turbulent clouds may lead to a better understanding of how feedback behaves on the scale of larger regions and influence these galaxy formation scenarios and cosmological simulations. Explanations for the differences in star formation efficiencies observed for various galaxies (Young 1999) and in galaxy mergers could be derived.

Provided that the physical processes are well described in the simulations, a comparison of the results with observations of young star clusters that recently expelled their residual gas may lead to independent age estimations.

Bibliography

Abbott, D. C. (1982). *The Return of Mass and Energy to the Interstellar Medium by Winds from Early-Type Stars*. ApJ **263**, 723–735.

Adams, D. (1996). *The Ultimate Hitchhikers Guide*. Wings Books, New York.

Adams, F. (2000). *Theoretical Models of Young Open Star Clusters: Effects of a Gaseous Component and Gas Removal*. ApJ **542**, 964–973.

Ashman, K. M. & S. E. Zepf (1992). *The Formation of Globular Clusters in Merging and Interacting Galaxies*. ApJ **384**, 50–61.

Ashman, K. M. & S. E. Zepf (1999). *Globular Cluster Systems*. Cambridge University Press, Cambridge.

Ashman, K. M. & S. E. Zepf (2001). *Some Constraints on the Formation of Globular Clusters*. AJ **122**, 1888–1895.

Barnes, J. & P. Hut (1986). *A Hierarchical O(N logN) Force-Calculation Algorithm*. Nature **324**, 446–449.

Bate, M. (1995). *The Role of Accretion in Binary Star Formation*. Dissertation, University of Cambridge.

Bate, M. R., I. A. Bonnell & V. Bromm (2001). *The Formation of a Cluster of Stars and Brown Dwarfs in a Turbulent Molecular Cloud*. In *Proceedings of 'The Origins of Stars and Planets: The VLT View', ESO Astrophysics Symposia, in press*.

Bate, M. R., I. A. Bonnell & N. M. Price (1995). *Modelling Accretion in Protobinary Systems*. MNRAS **277**, 362–376.

Bate, M. R. & A. Burkert (1997). *Resolution Requirements for Smoothed Particle Hydrodynamics Calculations with Self-Gravity*. MNRAS **288**, 1060–1072.

Baumgardt, H. (2001). *Dynamical Evolution of Star Clusters*. Reviews of Modern Astronomy **14**, 283–296.

Benz, W. (1990). *Smooth Particle Hydrodynamics: A Review*. In J. Buchler (Ed.), *The Numerical Modelling of Nonlinear Stellar Pulsations*, pp. 269–288. Kluwer Academic Publishers, Dordrecht, Boston, London.

Benz, W., R. Bowers, A. Cameron & W. Press (1990). *Dynamic Mass Exchange in Doubly Degenerate Binaries*. ApJ **348**, 647–667.

Bhatia, R. K. & H. T. MacGillivray (1988). *NGC 2214 - A Merging Binary Star Cluster in the Large Magellanic Cloud ?*. A&AL **203**, L5–L8.

Binney, J. & S. Tremaine (1987). *Galactic Dynamics*. Princeton University Press, Princeton.

Blitz, L. (1993). *Giant Molecular Clouds*. In E. H. Levy & J. I. Lunine (Ed.), *Protostars and Planets III*, pp. 125–161. The University of Arizona Press, Tucson, London.

Blitz, L. & F. H. Shu (1980). *The Origin and Lifetime of Giant Molecular Cloud Complexes*. ApJ **238**, 148–157.

Bonnell, I. A., M. R. Bate, C. J. Clarke & J. E. Pringle (2001). *Competitive Accretion in Embedded Stellar Clusters*. MNRAS **323**, 785–794.

Bonnell, I. A., C. J. Clarke, M. R. Bate & J. E. Pringle (2001). *Accretion in Stellar Clusters and the Initial Mass Function*. MNRAS **324**, 573–579.

Bonnor, W. B. (1956). *Boyle's Law and Gravitational Instability*. MNRAS **116**, 351–359.

Brown, J. H., A. Burkert & J. W. Truran (1995). *On the Formation of Globular Clusters: I. Early Dynamical Evolution*. ApJ **440**, 666–673.

Burkert, A. & P. Bodenheimer (2000). *Turbulent Molecular Cloud Cores: Rotational Properties*. ApJ **543**, 822–830.

Carretta, E., R. G. Gratton, G. Clementini & F. Fusi Pecci (2000). *Distances, Ages, and Epoch of Formation of Globular Clusters*. ApJ **533**, 215–235.

Cen, R. (2001). *Synchronized Formation of Subgalactic Systems at Cosmological Reionization: Origin of Halo Globular Clusters*. ApJ **560**, 592–598.

Chappell, D. & J. Scalo (2001). *Wind-Driven Gas Networks and Star Formation in Galaxies: Reaction-Advection Hydrodynamic Simulations*. MNRAS **325**, 1–33.

Chernoff, D. F. & S. Djorgovski (1989). *An Analysis of the Distribution of Globular Clusters with Postcollapse Cores in the Galaxy*. ApJ **339**, 904–918.

Datta, S. (2001). *Fractal Structure of Molecular Clouds*. astro-ph/0105036, to be published.

Dieball, A. & E. K. Grebel (2000). *Studies of Binary Star Cluster Candidates in the Bar of the LMC. II*. A&A **358**, 897–909.

Dieball, A., E. K. Grebel & C. Theis (2000). *Studies of Binary Star Cluster Candidates in the Bar of the LMC. I. SL 353 and SL 349*. A&A **358**, 144–153.

Djorgovski, S. & G. Meylan (1994). *The Galactic Globular Cluster System*. AJ **108**, 1292–1311.

Drissen, L., J. Roy, C. Robert, D. Devost & R. Doyon (2000). *The Star Formation History of the Starburst Region NGC 2363 and its Surroundings*. AJ **119**, 688–704.

Dubinski, J., R. Narayan & T. G. Phillips (1995). *Turbulence in Molecular Clouds*. ApJ **448**, 226–231.

Ebert, R. (1955). *Über die Verdichtung von H I-Gebieten*. Z. Astrophys. **37**, 217.

Elmegreen, B. G. (2000). *Star Formation in a Crossing Time*. ApJ **530**, 277–281.

Elmegreen, B. G. & Y. N. Efremov (1997). *A Universal Formation Mechanism for Open and Globular Clusters in Turbulent Gas*. ApJ **480**, 235–245.

Elmegreen, B. G. & Y. N. Efremov (1999). *Theory and Observations of Star Cluster Formation*. In V. G. Mannings, A. P. Boss & S. Russell (Ed.), *Protostars and Planets IV*. to be published.

Elmegreen, B. G. & E. Falgarone (1996). *A Fractal Origin for the Mass Spectrum of Interstellar Clouds*. ApJ **471**, 816–821.

Elson, R. A. W. (1991). *The Structure and Evolution of Rich Star Clusters in the Large Magellanic Cloud*. ApJS **76**, 185–214.

Fall, S. M. & Rees (1985). *A Theory for the Origin of Globular Clusters*. ApJ **298**, 18–26.

Fehlberg, E. (1969). *Low-Order Classical Runge-Kutta Formulas with Stepsize Control and their Application to Some Heat Transfer Problems*. NASA Technical Report, R–315.

Franco, J., S. N. Shore & G. Tenorio-Tagle (1994). *On the Massive Star–Forming Capacity of Molecular Clouds*. ApJ **436**, 795–799.

Fritze-v. Alvensleben, U. (1998). *Young Star Clusters in the Antennae: a Clue to Their Nature from Evolutionary Synthesis*. A&A **336**, 83–97.

Fujimoto, M. & Y. Kumai (1997). *Star Clusters Driven to Form by Strong Collisions between Gas Clouds in High–Velocity Random Motion*. AJ **113**, 249–263.

Gerritsen, J. P. E. & V. Icke (1997). *Star Formation in N–body Simulations. I. The Impact of the Stellar Ultraviolet Radiation on Star Formation*. A&A **325**, 972–986.

Geyer, M. P. & A. Burkert (2001). *The Effect of Gas Loss on the Formation of Bound Stellar Clusters*. MNRAS **323**, 988–994.

Gilmozzi, R., E. K. Kinney, S. P. Ewald, N. Panagia & M. Romaniello (1994). *WFPC2 Observations of the Double Cluster NGC 1850 in the Large Magellanic Cloud*. ApJL **435**, L43–L46.

Goldsmith, P. F. & W. D. Langer (1978). *Molecular Cooling and Thermal Balance of Dense Interstellar Clouds*. ApJ **222**, 881–895.

Goodman, A. A., J. A. Barranco, D. J. Wilner & M. H. Heyer (1998). *Coherence in Dense Cores. II. The Transition to Coherence*. ApJ **504**, 223+.

Goodman, A. A., P. J. Benson, G. A. Fuller & P. C. Myers (1993). *Dense Cores in Dark Clouds. VIII - Velocity Gradients*. ApJ **406**, 528–547.

Goodwin, S., F. Pearce & P. Thomas (2001). *The Effects of Gas Expulsion on Star Clusters*. In *ASP Conf. Ser. 228: Dynamics of Star Clusters and The Milky Way*, pp. 440–442.

Goodwin, S. P. (1997). *Residual Gas Expulsion from Young Globular Clusters*. MNRAS **284**, 785–802.

Goodwin, S. P. (1998). *Constraints on the Initial Conditions of Globular Clusters*. MNRAS **294**, 47–60.

Goodwin, S. P., F. R. Pearce & P. A. Thomas (2000). *Simulating Supernovae Remnants in Gas Clouds*. astro-ph/0001180, submitted to ApJ.

Harris, W. E. (1991). *Globular Cluster Systems in Galaxies Beyond the Local Group*. ARAA **29**, 543–579.

Harris, W. E. (1996). *A Catalog of Parameters for Globular Clusters in the Milky Way*. AJ **112**, 1487–1488, http://physun.physics.mcmaster.ca/Globular.html, revision June 22, 1999.

Hernquist, L. (1987). *Performance Characteristics of Tree Codes*. ApJS **64**, 715–734.

Hills, J. G. (1980). *The Effect of Mass Loss on the Dynamical Evolution of a Stellar System: Analytic Approximations*. ApJ **225**, 986–991.

Katz, N. (1992). *Dissipational Galaxy Formation. II. Effects of Star Formation*. ApJ **391**, 502–517.

Kessel-Deynet, O. & A. Burkert (2000). *Ionizing Radiation in Smoothed Particle Hydrodynamics*. MNRAS **315**, 713–721.

Kimura, T. & M. Tosa (1993). *Shock Propagation in a Turbulent Cloud*. ApJ **406**, 512–519.

Kimura, T. & M. Tosa (1996). *Collision of Clumpy Molecular Clouds*. A&A **308**, 979–987.

King, I. R. (1966). *The Structure of Star Clusters. III. Some Simple Dynamical Models*. AJ **71**, 64–75.

Klessen, R. (1997). *GRAPESPH With Fully Periodic Boundary Conditions: Fragmentation of Molecular Clouds*. MNRAS **292**, 11–18.

Klessen, R. S. (1998). *Fragmentation of a Molecular Cloud: The Initial Phases of a Stellar Cluster*. Dissertation, Ruprecht-Karls-Universität Heidelberg.

Klessen, R. S. & A. Burkert (2000). *The Formation of Stellar Clusters: Gaussian Cloud Conditions. I.*. ApJS **128**, 287–319.

Klessen, R. S. & A. Burkert (2001). *The Formation of Stellar Clusters: Gaussian Cloud Conditions. II.*. ApJ **549**, 386–401.

Knödlseder, J. (2000). *Cygnus OB2 - A Young Globular Cluster in the Milky Way*. A&A **360**, 539–548.

Koo, B.-C. (1999). *CO Observations of the W51B HII Region Complex*. ApJ **518**, 760–768.

Kroupa, P., S. Aarseth & J. Hurley (2001). *The Formation of a Bound Star Cluster: from the Orion Nebula Cluster to the Pleiades*. MNRAS **321**, 699–712.

Kumai, Y., B. Basu & M. Fujimoto (1993). *Formation of Globular Clusters from Gas in Large-Scale Unorganized Motion in Galaxies*. ApJ **404**, 144–161.

Kutta, W. (1901). *Beitrag zur näherungsweisen Integration totaler Differentialgleichungen*. Zeitschrift für Mathematik und Physik **46**, 435–453.

Lada, C. J., M. Margulis & D. Dearborn (1984). *The Formation and Early Dynamical Evolution of Bound Stellar Systems*. ApJ **285**, 141–152.

Lada, E. A. & C. J. Lada (1995). *Near-Infrared Images of IC 348 and the Luminosity Functions of Young Embedded Star Clusters*. AJ **109**, 1682–1696.

Lang, B., O. Kessel-Deynet & A. Burkert (2001). *Radiative Transport for a Smoothed Particle Hydrodynamic Code*. In *Astronomische Gesellschaft Meeting Abstracts*, Band 18, pp. 81+.

Lüst, R. (1978). *Hydrodynamik*. Wissenschaftsverlag, Mannheim, Wien, Zürich.

Mac Low, M. (1999). *The Energy Dissipation Rate of Supersonic, Magnetohydrodynamic Turbulence in Molecular Clouds*. ApJ **524**, 169–178.

Mac Low, M., M. D. Smith, R. S. Klessen & A. Burkert (1998). *The Decay of Supersonic and Super-Alfvénic Turbulence in Star-Forming Clouds*. Astrophysics and Space Science **261**, 195–196.

Makino, J., M. Taiji, T. Ebisuzaki & D. Sugimoto (1997). *GRAPE-4: A Massively Parallel Special-Purpose Computer for Collisional N–Body Simulations*. ApJ **480**, 432+.

Mathieu, R. D. (1983). *Dynamical Constraints on Star Formation Efficiency*. ApJL **267**, L97–L101.

Mermilliod, J.-C. (2000). *Massive Clusters in the Milky Way and Magellanic Clouds*. In *ASP Conf. Ser. 211: Massive Stellar Clusters*, pp. 43–48.

Meylan, G. & D. C. Heggie (1997). *Internal Dynamics of Globular Clusters.*. ARAA **8**, 1–143.

Monaghan, J. (1992). *Smoothed Particle Hydrodynamics*. ARAA **30**, 543–574.

Monaghan, J. & J. Lattanzio (1985). *A Refined Particle Method for Astrophysical Problems*. A&A **149**, 135–143.

Morgan, S. & G. Lake (1989). *The Self-Enrichment of Globular Clusters*. ApJ **339**, 171–177.

Murray, S. D. & D. N. C. Lin (1992). *Globular Cluster Formation: The Fossil Record*. ApJ **400**, 265–272.

Myers, P. C., T. M. Dame, P. Thaddeus & R. S. Cohen (1986). *Molecular Clouds and Star Formation in the Inner Galaxy: A Comparison of CO, HII, and Far-Infrared Surveys*. ApJ **301**, 398–422.

Myers, P. C. & C. Gammie (1999). *On the Turbulent Velocity Dispersion in Molecular Clouds*. ApJL **522**, L141–L144.

Naab, T. & A. Burkert (2001). *The Formation of Disks in Elliptical Galaxies*. ApJL **555**, L91–L94.

Nakasato, N., M. Mori & N. Ken'ichi (2000). *Numerical Simulations of Globular Cluster Formation*. ApJ **535**, 776–787.

Okumura, S. K., J. Makino, T. Ebisuzaki, T. Fukushige, T. Ito, D. Sugimoto, E. Hashimoto, K. Tomida & N. Miyakawa (1993). *Highly Parallelized Special-Purpose Computer, GRAPE-3*. PASJ **45**, 329–338.

Parmentier, G., E. Jehin, P. Magain, C. Neuforge, A. Noels & A. Thoul (1999). *The Self-Enrichment of Galactic Halo Globular Clusters: A Clue to their Formation ?*. A&A **352**, 138–148.

Peebles, P. & R. Dicke (1968). *Origin of the Globular Star Clusters*. ApJ **154**, 891–908.

Press, W. (1986). In P. Hut & S. McMillan (Ed.), *The Use of Supercomputers in Stellar Dynamics, Springer Lecture Notes in Physics*, pp. 184. Springer, Berlin, Heidelberg, New York.

Press, W. H., S. A. Teukolsky, W. T. Vetterling & B. P. Flannery (1999). *Numerical Recipes in C* (2 edition). Cambridge University Press, Cambridge.

Reif, F. (1987). *Statistische Physik und Theorie der Wärme* (3 edition). de Gruyter, Berlin, New York.

Saiyadpour, A., B. M. Deiss & W. H. Kegel (1997). *The Effect of Dynamical Friction on a Young Stellar Cluster Prior to the Gas Removal*. A&A **322**, 756–763.

Salpeter, E. E. (1955). *The Luminosity Function and Stellar Evolution*. ApJ **121**, 161–167.

Scheffler, H. & H. Elsässer (1992). *Bau und Physik der Galaxis* (2. edition). BI-Wissenschaftsverlag, Mannheim, Leipzig.

Schweizer, F. (1999). *Young Globular Clusters*. In *ASP Conf. Ser. 192: Spectrophotometric Dating of Stars and Galaxies*, pp. 135+.

Spitzer, L. J. (1968). *Diffuse Matter in Space*. Interscience Publishers, New York.

Spitzer, L. J. (1978). *Physical Processes in the Interstellar Medium*. John Wiley & Sons, New York, Chichester, Brisbane, Toronto.

Spitzer, L. J. (1987). *Dynamical Evolution of Globular Clusters*. Princeton University Press, New Jersey.

Springel, V. (2000). *Modelling Star Formation and Feedback in Simulations of Interacting Galaxies*. MNRAS **312**, 859–879.

Steinmetz, M. (1996). *GRAPESPH: Cosmological Smoothed Particle Hydrodynamics Simulations with the Special-Purpose Hardware GRAPE*. MNRAS **278**, 1005–1017.

Stoer, J. & R. Bulirsch (1990). *Numerische Mathematik 2* (3 edition). Springer Verlag, Berlin, Heidelberg, New York.

Stutzki, J., F. Bensch, A. Heithausen, V. Ossenkopf & M. Zielinsky (1998). *On the Fractal Structure of Molecular Clouds*. ARAA **336**, 697–720.

Thacker, R. J. & H. M. P. Couchman (2000). *Implementing Feedback in Simulations of Galaxy Formation: A Survey of Methods*. ApJ **545**, 728–752.

Umemura, M., T. Fukushige, J. Makino, T. Ebisuzaki, D. Sugimoto, E. L. Turner & A. Loeb (1993). *Smoothed Particle Hydrodynamics with GRAPE-1A*. PASJ **45**, 311–320.

van den Bergh, S. (2000). *Some Musings on Globular Cluster Systems*. PASP **112**, 932–941.

van den Bergh, S. (2001). *How did Globular Clusters Form ?*. ApJ **559**, L113–L114.

Verschueren, W. (1990). *Collapse of Young Stellar Clusters Before Gas Removal*. A&A **234**, 156–163.

Wetzstein, M., T. Naab, A. Nelson, O. Kessel-Deynet & A. Burkert (2001). *A New Tree Code for SPH and N–Body Simulations*. In *Astronomische Gesellschaft Meeting Abstracts*, Band 18, pp. 156+.

Whitmore, B. C. & F. Schweizer (1995). *Hubble Space Telescope Observations of Young Star Clusters in NGC 4038/4039, "The Antennae" Galaxies*. AJ **109**, 960–980.

Whitmore, B. C., Q. Zhang, C. Leitherer, S. M. Fall, F. . Schweizer & B. W. Miller (1999). *The Luminosity Function of Young Star Clusters in "the Antennae" Galaxies (NGC 4038-4039)*. AJ **118**, 1551–1576.

Whitworth, A. (1998). *The Jeans Instability in Smoothed Particle Hydrodynamics*. MNRAS **296**, 442–444.

Williams, J. P. & C. F. McKee (1997). *The Galactic Distribution of OB Associations in Molecular Clouds*. ApJ **476**, 166–183.

Young, J. S. (1999). *The Efficiency of Star Formation in Galaxies as a Function of Galaxy Size and Environment*. ApJL **514**, L87–L90.

Zepf, S. E., K. M. Ashman, J. English, K. C. Freeman & R. M. Sharples (1999). *The Formation and Evolution of Candidate Young Globular Clusters in NGC 3256*. AJ **118**, 752–764.

Zinn, R. (1985). *The Globular Cluster System of the Galaxy. IV. The Halo and Disk Subsystems*. ApJ **293**, 424–444.

Herzlichen Dank an...

all die Leute die mich bei der Anfertigung dieser Arbeit unterstützt haben – astronomisch, physikalisch und mental !

Besonders bedanken möchte ich mich bei Priv.-Doz. Dr. Andreas Burkert für die Betreuung meiner Arbeit am MPIA, die ungezwungene Arbeitsatmosphäre, inspirierende Gespräche und tatkräftige Hilfe dort, wo immer es nötig war.

Danke auch an Dr. Ralf Klessen sowie Dr. Matthew Bate, ohne deren SPH–Code diese Arbeit so nicht möglich gewesen wäre.

Vielen Dank auch an Dipl.-Phys. Bernd Lang und Dipl.-Phys. Regina Kalchgruber für die sorgfältige und kritische Korrektur des Manuskripts.

Bei meinem Zimmerkollegen Dr. Markus Feldt bedanke ich mich für die stets gute Stimmung in unserem Büro und seine richtungsweisende Nebelleuchte.

Danke natürlich auch an die gesamten MPIA-Theoristen und alle anderen MPIAler für das immer lockere und offene Arbeitsumfeld.

Unter keinen Umständen vergessen möchte ich Prof. Dr. Friedrich Schmitz, der mich mit seiner gewissenhaften wissenschaftlichen Arbeitsweise an die theoretische Astrophysik herangeführt hat.

Nicht zuletzt danke ich Ginni, ohne die ich nicht die nötige Kraft hätte aufbringen können.

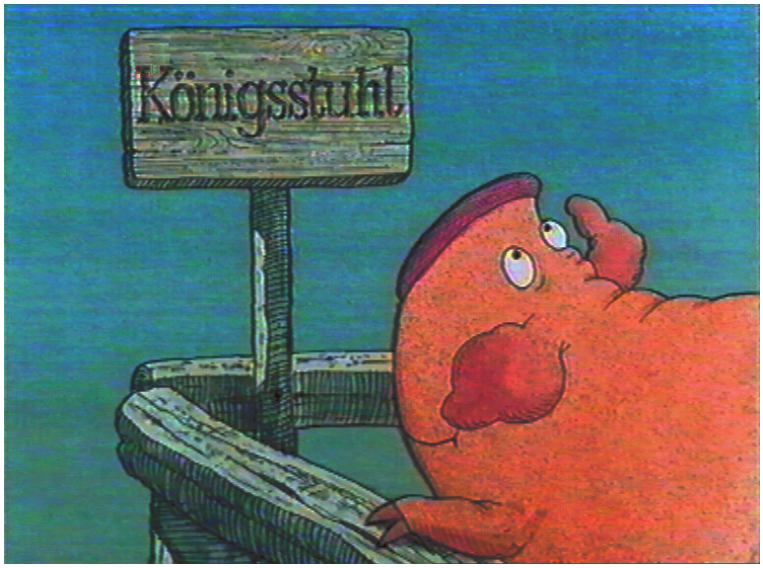

„Frederick," fragte Piggeldy seinen großen Bruder,
„Frederick, was ist ein Königsstuhl ?"

Ein Hauch von Gelb.